REAL-TIME VEHICLE PARAMETER ESTIMATION
AND ADAPTIVE STABILITY CONTROL

A Dissertation
Presented to
the Graduate School of
Clemson University

In Partial Fulfillment
of the Requirements for the Degree
Doctor of Philosophy
Automotive Engineering

by
John Limroth
December 2009

Accepted by:
Dr. Thomas R. Kurfess, Committee Chair
Dr. E. Harry Law
Dr. Beshahwired Ayalew
Dr. Timothy B. Rhyne

UMI Number: 3389256

UMI

Dissertation Publishing

ProQuest®

ABSTRACT

This dissertation presents a novel Electronic Stability Control (ESC) strategy that is capable of adapting to changing vehicle mass, tire condition and road surface conditions. The benefits of ESC are well understood with regard to assisting drivers to maintain vehicle control during extreme handling maneuvers or when extreme road conditions such as ice are encountered. However state of the art ESC strategies rely on known and invariable vehicle parameters such as vehicle mass, yaw moment of inertia and tire cornering stiffness coefficients. Such vehicle parameters may change over time, especially in the case of heavy trucks which encounter widely varying load conditions. The objective of this research is to develop an ESC control strategy capable of identifying changes in these critical parameters and adapting the control strategy accordingly.

An ESC strategy that is capable of identifying and adapting to changes in vehicle parameters is presented. The ESC system utilizes the same sensors and actuators used on commercially-available ESC systems. A nonlinear reduced-order observer is used to estimate vehicle sideslip and tire slip angles. In addition, lateral forces are estimated providing a real-time estimate of lateral force capability of the tires with respect to slip angle. A recursive least squares estimation algorithm is used to automatically identify tire cornering stiffness coefficients, which in turn provides a real-time indication of axle lateral force saturation and estimation of road/tire coefficient of friction. In addition, the recursive least squares estimation is shown to identify changes in yaw moment of inertia that may occur due to changes in vehicle loading conditions. An algorithm calculates the reduction in yaw moment due to axle saturation and determines an equivalent moment to

be generated by differential braking on the opposite axle. A second algorithm uses the slip angle estimates and vehicle states to predict a Time to Saturation (TTS) value of the rear axle and takes appropriate action to prevent vehicle loss of control. Simulation results using a high fidelity vehicle modeled in CarSim show that the ESC strategy provides improved vehicle performance with regard to handling stability and is capable of adapting to the identified changes in vehicle parameters.

DEDICATION

This dissertation is dedicated to my wife, Elena Kathleen Limroth, and our sons Antone Francisco Treviño Limroth and Ian Charles Limroth. This research could not have been possible without their love, support and patience. The many sacrifices they made to allow me to pursue this degree will be forever appreciated.

ACKNOWLEDGMENTS

TABLE OF CONTENTS

Table of Contents (Continued)

Table of Contents (Continued)

LIST OF TABLES

LIST OF FIGURES

List of Figures (Continued)

List of Figures (Continued)

NOTATION

Subscripts

Subscripts are used to indicate a quantity that is "per axle" or "per wheel."

A single number in the subscript indicates a per axle variable:
- 1: Front axle
- 2: Rear axle

A subscript number immediately followed by a letter "L" or "R" indicates a per wheel variable:
- 1L: Front left wheel
- 1R: Front right wheel
- 2L: Rear left wheel
- 2R: Rear right wheel

Variables in **bold** indicate either a matrix (upper case letter) or vector (lower case letter).

The hat symbol ^ above a variable indicates an estimated state or parameter.

List of Symbols

α	Wheel slip angle
α_L	Lagged wheel slip angle
α_{sat}	Slip angle corresponding to lateral force saturation
$\alpha_{sat,ideal}$	Slip angle corresponding to linear cornering stiffness at maximum traction force
δ	Road wheel steer angle
δ_{HW}	Hand wheel steer angle
κ	Wheel longitudinal slip ratio
κ_{LL}	Wheel longitudinal slip ratio lower limit for ABS control
κ_{UL}	Wheel longitudinal slip ratio upper limit for ABS control
λ	Recursive least squares exponential forgetting factor
μ	Road/tire surface coefficient of friction
$\mathbf{\Phi}_n$	Regression matrix of linear estimation equations at step n

ϕ_{a_y}	Lateral acceleration phase delay
$\boldsymbol{\theta}$	Parameter vector of linear estimation equations
σ_{total}	Tire total slip
σ_x	Tire longitudinal slip
σ_y	Tire lateral slip
τ	Tire lateral force lag time constant
ω	Wheel spin angular velocity
$\omega_{n,r}$	Yaw rate natural frequency
ζ_r	Yaw rate damping ratio
$\mathbf{A}$	State-space model $\mathbf{A}$ matrix
A	Coefficient of quadratic term in quadratic equation
a	Longitudinal distance from vehicle center of gravity to front axle
a_y	Vehicle lateral acceleration relative to inertial reference frame
a'_y	Vehicle lateral acceleration for bicycle model with yaw rate input
a_{ij}	Entry in state-space model $\mathbf{A}$ matrix
$\mathbf{B}$	State-space model $\mathbf{B}$ matrix
B	Coefficient of linear term in quadratic equation
b	Longitudinal distance from rear axle to vehicle center of gravity
b_{ij}	Entry in state-space model $\mathbf{B}$ matrix
$\mathbf{C}$	State-space model $\mathbf{C}$ matrix
C	Coefficient of constant term in quadratic equation
C_i	Cornering stiffness of axle i
c_{ij}	Entry in state-space model $\mathbf{C}$ matrix
$\mathbf{D}$	State-space model $\mathbf{D}$ matrix
d_{ij}	Entry in state-space model $\mathbf{D}$ matrix
$E\{\ \}$	Expected value operator
E_{diff}	Differential efficiency ratio

F_x	Longitudinal braking force in –x direction of wheel reference frame
F_x^*	Longitudinal brake force potential at zero slip angle
$F_{x,c}$	Longitudinal brake force commanded by ESC differential braking
$F_{x,u}$	Hypothetical longitudinal brake force without ESC differential braking
F_y	Lateral force in +y direction of wheel reference frame
F_y^*	Lateral brake force potential at zero longitudinal slip ratio
$F_{y,c}$	Reduced lateral force due to longitudinal brake force commanded by ESC differential braking
$F_{y,u}$	Hypothetical lateral force without ESC differential braking
$F_{y,deadzone}$	Lateral force dead zone from theoretical linear lateral force to saturation limit lower bound
$F_{y,sat}$	Lateral force saturation limit lower bound
ΔF_y	Difference between lateral force predicted by linear cornering stiffness and actual lateral force
F_z	Normal force in +z direction of wheel reference frame
$\mathbf{I}$	Identity matrix
I_{eff}	Effective combined spin inertia of wheel and drivetrain components
I_{trans}	Transmission spin inertia
I_w	Wheel spin inertia
J	Total vehicle yaw moment of inertia including driver
J_M	Driver mental workload metric
J_P	Driver physical workload metric
J_T	Task performance metric
$\mathbf{K}$	Observer feedback gain matrix
$\mathbf{K}_n$	Update matrix $\mathbf{K}$ of regressive least squares algorithm at step n
K	Vehicle stability factor
K_{us}	Vehicle understeer gradient

k	Observer feedback gain
k_b	Wheel brake torque constant
k_n	Update variable k of regressive least squares algorithm at step n
L_y	Tire lateral force relaxation length *or* simulation vehicle lateral position
$L_{y,target}$	Target vehicle lateral position for simulated driver model
M_z	Yaw moment about vehicle center of gravity
$M_{z,c}$	Yaw moment about vehicle center of gravity due to longitudinal brake forces of wheels
$M_{z,p}$	Predicted yaw moment about vehicle center of gravity from lateral forces generated by linear cornering stiffnesses
ΔM_z	Difference between predicted yaw moment from linear cornering stiffnesses and actual yaw moment from lateral forces
ΔM_z	Net change in yaw moment due to ESC differential braking
m	Total vehicle mass including driver
N_{diff}	Differential gear ratio
P_b	Wheel-end brake pressure
P_n	Update variable P of regressive least squares algorithm at step n
$\mathbf{P}_n$	Update matrix $\mathbf{P}$ of regressive least squares algorithm at step n
$\mathbf{Q}$	Process noise auto-covariance matrix
Q	Process noise auto-covariance scalar value
$\mathbf{R}$	Measurement noise auto-covariance matrix
R	Measurement noise auto-covariance scalar value
R_z	Radius of gyration of vehicle yaw moment of inertia
r	Vehicle yaw angular rate
$\dot{r}$	Vehicle yaw angular acceleration
r_{rec}	Desired yaw rate to recover rear axle lateral force stability
T_b	Wheel brake torque
T_d	Wheel drive torque

T_{trans}	Transmission output torque
t	Vehicle track width (between tire contact patch centers)
t_{rec}	Predicted time to recover rear axle lateral force stability by ESC differential braking
t_{sat}	Predicted time to rear axle lateral force saturation
$\mathbf{v}(t)$	Stochastic model measurement random noise vector
v_x	Vehicle forward velocity in vehicle reference frame
v_{xi}	Axle i forward velocity in reference frame of axle i wheels
v_y	Vehicle lateral velocity in vehicle reference frame
$\dot{v}_y$	Vehicle lateral acceleration relative to vehicle reference frame
v_{yi}	Axle i lateral velocity in reference frame of axle i wheels
v_y'	Vehicle lateral velocity for bicycle model with yaw rate input
$\mathbf{w}(t)$	Stochastic model process random noise vector
$\mathbf{x}$	State-space model state vector
$\mathbf{y}$	State-space model output vector
$\mathbf{y}_n$	Output vector of linear estimation equations at step n

CHAPTER ONE

INTRODUCTION

1.1 Motivation

A study by the Insurance Institute for Highway Safety on all types of road vehicles has found that Electronic Stability Control (ESC) systems "could prevent nearly one-third of all fatal crashes and reduce the risk of rolling over by as much as 80 percent [1]." In light of these benefits, NHTSA has issued Federal Motor Vehicle Safety Standard 126 which mandates that all new light vehicles include ESC systems as standard equipment by September 2011 [2]. While the inclusion of ESC on heavy trucks is not yet mandated, increasingly the cost benefits of such systems are being emphasized by suppliers and it is believed that legislation mandating ESC systems on heavy trucks is on the horizon.

A study by Wang and Council [3] determined that there are approximately 4,500 to 5,000 truck rollovers on ramps per year in the U.S. In addition to potential injury and loss of life, rollover accidents can also be very expensive to vehicle operators. According to Sampson and Cebon [4], the average cost of heavy truck rollover incidents in the United Kingdom is estimated to be between $120,000 and $160,000. Heavy truck ESC systems can be an effective measure at reducing the number of rollover and other incidents. Bendix, a commercial truck ESC system supplier, reports that the addition of ESC to commercial vehicles results in a 10-60% reduction in incidents such as rollover, jackknifing or loss of control [5].

1.2 Problem Statement

Current state of the art ESC systems utilize the well-known bicycle handling model as the basis for determining expected vehicle response with regard to driver steering input. Commonly state variable feedback designs are used where measured vehicle states are compared to the theoretical vehicle states predicted by the bicycle model simulated as part of the control system. Unfortunately the applicability of the bicycle handling model, and hence the control system, is restricted by the accuracy of vehicle parameters such as mass, yaw moment of inertia, center of gravity (CG) longitudinal location and tire cornering stiffness coefficients.

Commercial trucks have loading conditions that vary in both magnitude and load distribution from trip to trip. In addition, even passenger cars which have less variation in loading conditions may have worn tires or replacement tires which have different handling properties. These changes that may occur in fundamental vehicle parameters motivate the need for a stability control system that can identify the parameter changes and adapt the control strategy accordingly.

1.3 Objectives

The fundamental objective of this thesis is the development of an ESC system that is capable of identifying changes in relevant vehicle and environment parameters and adapting the control strategy to these changes. The system should identify changes in tire lateral cornering stiffness that may occur over time due to tire wear or replacement. The system should also compensate for changes in vehicle mass and/or yaw moment of inertia that may occur due to passenger or freight loading. In addition, the system should

automatically identify the current road/tire coefficient of friction. The control strategy itself should be robust with respect to changes in these parameters and be capable of adapting the strategy as needed to compensate for the changes. The system should be capable of accomplishing these objectives using current state of the art ESC sensors and actuators and possible additional sensors that add only marginal cost and complexity. In addition the parameter identification and adaptive stability control algorithms should be of a reasonable complexity for implementation on modern vehicle electronic control units.

1.4 Contributions

The fundamental contributions of this research are as follows:

1. A novel nonlinear reduced-order vehicle lateral velocity observer that accurately tracks lateral velocity during non-linear handling events, but is robust with respect to measurement noise and/or bias.

2. A method of estimating lateral forces and lateral force potential of each wheel.

3. Real-time identification of axle linear cornering stiffness coefficients and vehicle yaw moment of inertia, which enables adaptation of the control strategy to changes in tire cornering stiffness or vehicle loading condition.

4. Estimation of axle lateral force saturation when the estimated lateral force magnitude falls below that predicted by the current linear cornering stiffness coefficient and slip angle estimates.

5. Estimation of road/tire coefficient of friction from saturated axle lateral force and normal force.

6. An "equivalent moment" stability control strategy that uses differential braking to generate a yaw moment equal to the reduction in moment of the saturated axle, while considering the interaction of lateral and longitudinal forces on the actuated wheel.

7. A "Time to Saturation" predictive control strategy capable of applying front axle differential braking prior to saturation of the rear axle lateral force to maintain vehicle stability.

8. An advanced Anti-lock Braking System (ABS) strategy that adapts longitudinal slip targets to account for road/tire coefficient of friction and interaction of longitudinal and lateral slip of the wheels.

1.5 Dissertation Overview

In Chapter 2 a review of relevant literature on state of the art ESC strategies, vehicle state estimation methods and vehicle parameter identification methods is presented. Subsequent Chapters 3-6 outline the various components of the parameter identification and ESC strategies developed. The general structure of the developed strategy and organization of these chapters is shown in Figure 1.1.

Chapter 3 presents a survey of approaches to estimating vehicle lateral velocity, including the nonlinear reduced-order kinematic observer developed for this work. The use of the estimated lateral velocity to generate estimates of axle slip angles is also discussed.
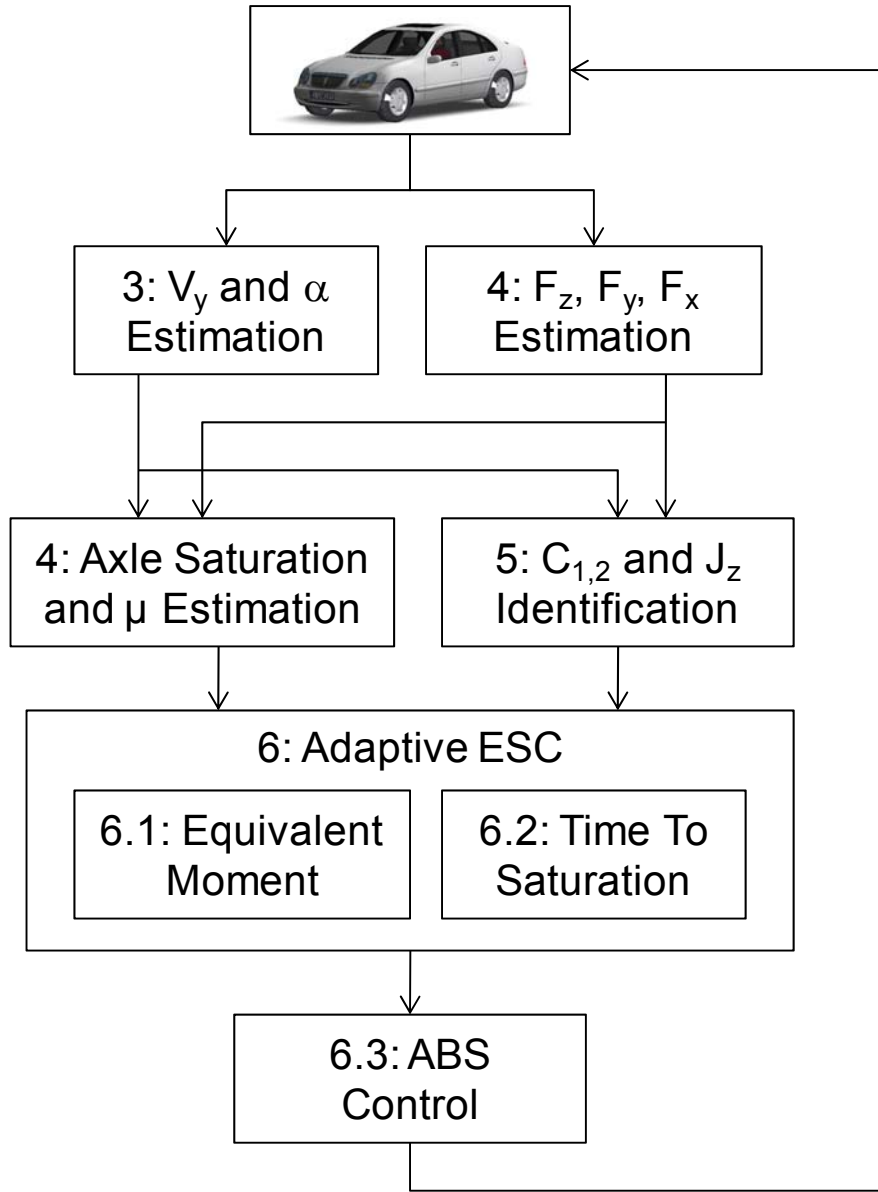
Figure 1.1: Organization of Dissertation Chapters 3-6 on ESC Strategy

In Chapter 4 estimates of axle lateral forces are determined from the ESC sensor values by inversion of the linear force and angular momentum equations. This chapter also explains the determination of axle lateral force saturation and estimation of road/tire coefficient of friction. Chapter 5 shows how the estimated axle slip angles and lateral

5

forces may be used with a recursive least squares algorithm to estimate cornering stiffnesses and yaw moment of inertia. The ESC algorithm is presented in Chapter 6, including an equivalent moment differential braking strategy employed when axle saturation is detected and a predictive Time To Saturation (TTS) algorithm that takes corrective action when impending rear axle saturation is detected. This chapter also describes the Anti-Lock Braking (ABS) algorithm used to control braking of individual wheels.

The remaining chapters summarize the results of simulations of the designed ESC strategy. Chapter 7 presents results of co-simulation of the adaptive ESC strategy and a high-fidelity vehicle model in CarSim. Finally conclusions and ideas for future work are provided in Chapter 8.

CHAPTER TWO

BACKGROUND

This section provides an overview of the current literature relevant to this project. First an overview of ESC systems for passenger vehicles is provided. Then methods of vehicle state and parameter estimation in the literature are presented.

2.1 Electronic Stability Control Algorithms

Electronic stability control is currently implemented in many production passenger vehicles to prevent spin-out and to match the vehicle yaw rate response to the intent of the driver [6, 7]. The fundamental concept of current ESC systems is the use of differential braking to apply a yaw moment to the vehicle in order to ensure the vehicle follows the path indicated by the driver steering input. Actuation is accomplished by the use of hydraulic or pneumatic valves in the braking system which are also used for Anti-lock Braking System (ABS) functionality [8-12]. Sensors used by theses systems typically include a steering wheel angle sensor, individual wheel speed sensors, lateral accelerometer and yaw rate sensor [12].

It should be noted that ESC affects both vehicle handling stability and responsiveness, and often the design of the system involves a trade-off between the two [13]. One objective of this research is to match the model used for determining driver intent to the actual physical system in order to reduce the compromise in vehicle responsiveness due to the ESC system.
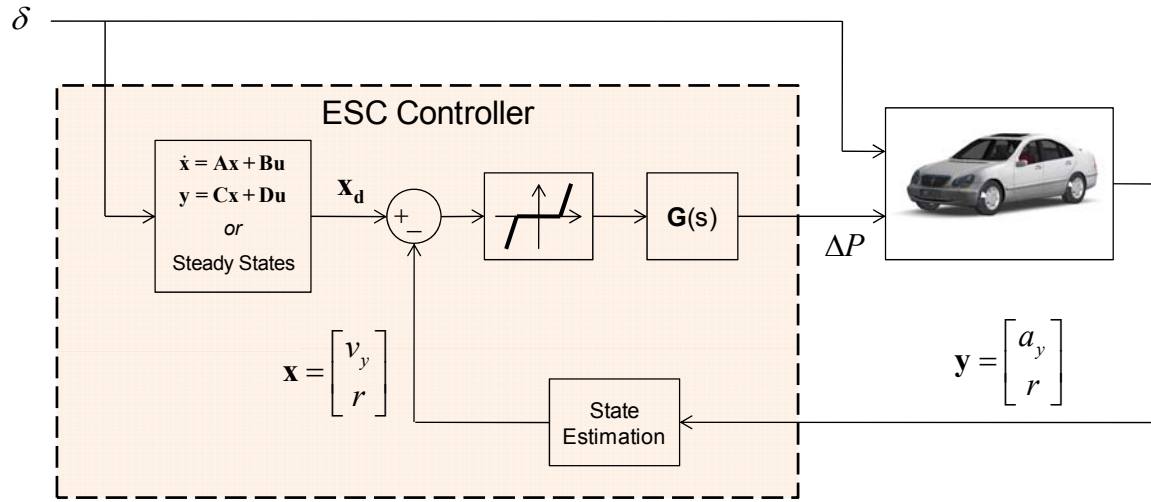
Figure 2.1: Typical ESC State Feedback Control Strategy

The general form of a typical ESC control scheme is shown in Figure 2.1. The current state vector **x** of the vehicle is determined from the measurements of the set of sensors described above. Some states such as vehicle lateral velocity cannot be measured directly, and instead must be estimated from the various sensor values. Approaches to addressing this and other problems are described below in section 2.3.2 Estimation From Lateral Dynamics.

The desired states are typically determined from the measured steering wheel angle and vehicle forward velocity using either a linear state space dynamic model or a steady state model of the vehicle [6, 10]. The dynamic model typically used is the classic bicycle handling model [14]. This model is called the bicycle model since differences in force generation between left and right wheels on an axle are ignored and may thus be approximated by a single wheel at the center of the axle. The bicycle model is depicted graphically in Figure 2.2 with a top view of the vehicle.

8
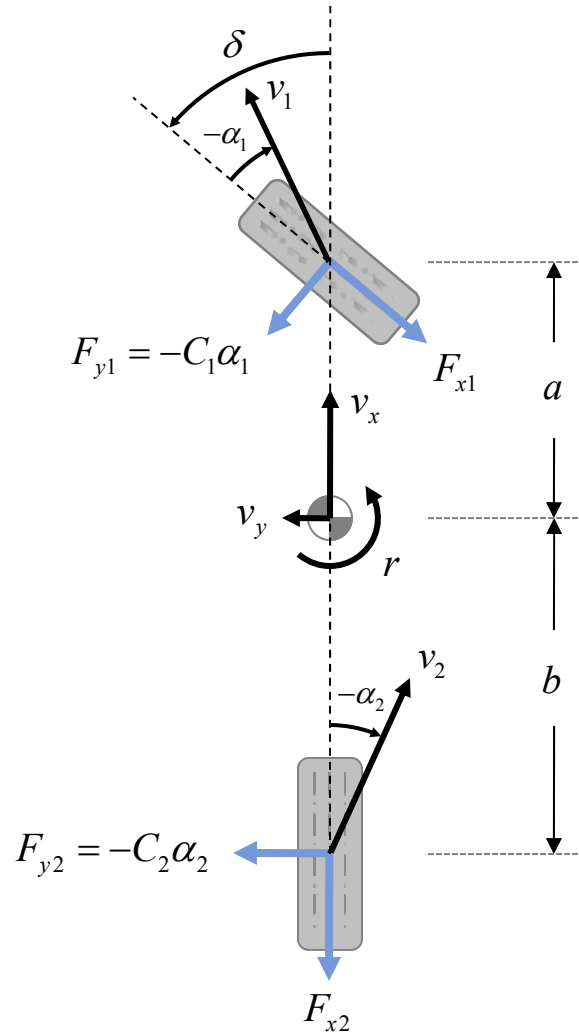
Figure 2.2: Bicycle Dynamic Handling Model

The total vehicle center of gravity is located a distance *a* behind the front axle and a distance *b* in front of the rear axle. The vehicle velocity at the center of gravity is separated into longitudinal v_x and lateral v_y components. The vehicle yaw rate *r* is also indicated at the vehicle center of gravity. The bicycle model assumes a constant forward velocity v_x, therefore the two states of the model are lateral velocity v_x and yaw rate *r*. The velocity vector of each axle v_i is indicated at the virtual wheel located at the center of

each axle. The model depicted assumes steering of the front wheels only through a road

wheel steer angle δ. The angle between the axle longitudinal axis and the axle velocity

vector is defined as the slip angle α_i, which is negative in the direction shown for both

axles in Figure 2.2. The bicycle modal assumes a linear lateral force response with

respect to slip angle. The linear lateral force gain is defined as the axle cornering

stiffness C_i. A longitudinal braking force in the axle –x direction may also be present at

each axle as shown in the figure.

The resulting linear bicycle model is second order with vehicle states of lateral

velocity (or alternatively sideslip angle) and yaw rate.

$$
\begin{bmatrix} \dot{v}_y \\ \dot{r} \end{bmatrix} = \begin{bmatrix} -\dfrac{C_1+C_2}{mv_x} & \dfrac{-aC_1+bC_2}{mv_x}-v_x \\ \dfrac{-aC_1+bC_2}{Jv_x} & -\dfrac{a^2C_1+b^2C_2}{Jv_x} \end{bmatrix} \begin{bmatrix} v_y \\ r \end{bmatrix} + \begin{bmatrix} \dfrac{C_1}{m} \\ \dfrac{aC_1}{J} \end{bmatrix} \delta
\qquad (2.1)
$$

Here the longitudinal brake forces of the steered axle are not included in the model, and

m is the total vehicle mass and J the yaw moment of inertia. Lookup tables are typically

used to vary the matrix entries with vehicle speed v_x.

The desired states determined from the bicycle model are compared to the

measured and estimated states. Typically a deadband function is employed to ensure that

activation of the system only occurs when there is significant deviation between the

desired and the measured state values [10]. Some form of transfer function may then be

applied to the error signal to determine the demanded moment to the lower-level system

that implements differential braking. For example in the case of full-state feedback

control, this transfer function is simply a set of gains applied to the error signal [15, 16].

The output is generally either a differential braking pressure [6] or desired slip value for a brake controller to be applied at a specific wheel [16].

One common form of feedback control for ESC is the full-state feedback Linear Quadratic Regulator (LQR) [15, 16]. Such a design automatically places the poles of the closed loop system such that a cost function with weighted Q and R matrices to be applied to the state errors and control outputs respectively is minimized. Alternatively if only a single variable is used for feedback such as yaw rate, a simple PD controller may be used to place the closed loop poles at a desired location [6].

One approach applied by Anwar [17] is a model-predictive controller for yaw control. Another optimization-based approach is described by Eslamian [18]. This approach uses an optimization to design a non-linear controller for sideslip regulation. Sliding mode control is yet another approach that has been used to address the stability control problem [19-21].

It should be noted that differential braking has been employed on passenger vehicles for functions other than yaw rate and sideslip tracking. Wielenga [22] has proposed an "anti-rollover braking" scheme which uses differential braking to avoid rollover in vehicles with a relatively high center of gravity. In high sideslip conditions, such a vehicle is prone to rollover instead of spinning out as would a normal passenger car. Braking applied to the front outside wheel in such a condition will slow the vehicle and provide moment to reduce the vehicle sideslip. It should be noted however that while such a system might mitigate the risk of rollover, the vehicle will not necessarily track the direction intended by the driver and may still leave the roadway and result in an accident.

A common feature of the ESC strategies found in current literature is the use of errors in the measured or estimated states of the model to determine the control law. For example understeer or oversteer conditions are detected by errors in yaw rate. However, the saturation of lateral force generated by each axle, which causes the understeer or oversteer condition, is not identified. The goal of this work is to develop a strategy that will identify the lateral force saturation of each axle and take control action accordingly. As a result the controller may take appropriate actions when both axles are saturated in lateral force as opposed to only one axle in saturation. The ESC control strategies presented in this section are not able to make such a distinction since the physical cause of the vehicle instability is not identified.

2.2 Vehicle Lateral Velocity Estimation Methods

Estimators are often employed in automotive applications to determine vehicle states that cannot be measured directly. Specifically the vehicle lateral velocity (or equivalently vehicle sideslip angle) is of critical importance to the ESC control strategies described in the previous section, as well as to the adaptive ESC strategy presented in this dissertation. In general there are three approaches that have been applied to determining vehicle lateral velocity: direct measurement using cameras or Global Positioning Satellite (GPS) units, estimation using physical model based observers and estimation using kinematic model based observers. Some of the approaches presented below combine elements of several of these approaches in an attempt to overcome limitations of each. In fact the lateral velocity estimator described in this dissertation is an observer that dynamically combines elements of the physical and kinematic models.

While direct sensing of lateral velocity using cameras or GPS units has been demonstrated, these approaches generally suffer from low data throughput and are prohibitively expensive to implement in passenger vehicles [23]. One approach is the use of GPS and inertial navigation system (INS) rate sensors combined with a planar vehicle model [24]. However, such an approach does not address out-of-plane motion or rate gyrometer sensor bias [25]. More recently the use of two-antenna GPS for direct vehicle roll and heading measurement for improved sideslip estimation has been proposed [26]. Other approaches combine the use of GPS sensors with lateral velocity observer techniques described below. For example GPS velocity measurements have been combined with a model-based Kalman filter observer to improve estimates of vehicle sideslip [27, 28]. In addition GPS measurements have also been combined with a kinematic observer for the same purpose [25]. Note however while these techniques may prove to enhance the estimation capability of the observers alone, the cost of the GPS units themselves still prevents their use in commercial applications.

A variety of observer structures have been proposed to estimate lateral velocity from the sensor signals commonly available in ESC systems: usually lateral acceleration and yaw rate. These are typically Luenberger observers based on either a physical vehicle model such as equation (2.1) above or a kinematic equation. The general form of a full state observer based on the bicycle model is:

$$\begin{bmatrix} \dot{\hat{v}}_y \\ \dot{\hat{r}} \end{bmatrix} = \begin{bmatrix} -\dfrac{C_1+C_2}{mv_x} & \dfrac{-aC_1+bC_2}{mv_x}-v_x \\ \dfrac{-aC_1+bC_2}{Jv_x} & \dfrac{a^2C_1+b^2C_2}{Jv_x} \end{bmatrix} \begin{bmatrix} \hat{v}_y \\ \hat{r} \end{bmatrix} + \begin{bmatrix} \dfrac{C_1}{m} \\ \dfrac{aC_1}{J} \end{bmatrix} \delta + \mathbf{K}\left\{ \begin{bmatrix} a_y \\ r \end{bmatrix} - \begin{bmatrix} \hat{a}_y \\ \hat{r} \end{bmatrix} \right\}$$

$$\begin{bmatrix} \hat{a}_y \\ \hat{r} \end{bmatrix} = \begin{bmatrix} -\dfrac{C_1+C_2}{mv_x} & \dfrac{-aC_1+bC_2}{mv_x} \\ 0 & 1 \end{bmatrix} \begin{bmatrix} \hat{v}_y \\ \hat{r} \end{bmatrix} + \begin{bmatrix} \dfrac{C_1}{m} \\ 0 \end{bmatrix} \delta$$

(2.2)

The matrix **K** is the observer feedback gain matrix, and may be designed by several different methods. As shown in section 3.1.2 Full-Order Observer, the observer dynamic matrix is **A-KC**, and the gains may be selected to produce desired eigenvalues of this matrix using pole placement methods. Alternatively, the system of equation (2.2) may be treated as a stochastic system and a Kalman filter may be designed to produce the observer feedback matrix. In general, lateral velocity observers designed using physical models produce estimates with low noise, but are sensitive to vehicle parameters and produce good results only in the linear handling range [27].

Hac and Simpson developed a model based full-order observer for both lateral velocity and yaw rate from steering and lateral acceleration measurements [29]. The physical model includes a nonlinear model of tire force characteristics as well as an estimation of road/tire coefficient of friction

Another example of a model based lateral velocity observer is presented by Liu and Peng [30]. This method simultaneously estimates lateral velocity and tire cornering stiffnesses as described in section 2.3.2 Estimation From Lateral Dynamics. This method was compared to others by Ungoren, et. al., and found to have slow convergence of the state and parameter estimations [31].

Farrelly and Wellstead showed how a steady state Kalman filter could be designed for the physical model based observer, and showed an alternative gain design that is insensitive to the rear axle cornering stiffness parameter [27]. However such an observer cannot be designed to be insensitive to all parameters of the physical model that may change over time and thus influence the accuracy of the observer. Deng and Haicen implemented a model based Luenberger observer with feedback gains designed to produce desired observer eigenvalues [23]. As discussed in section 2.3.2 Estimation From Lateral Dynamics, they also implemented cornering stiffness parameter estimation for both axles to reduce the sensitivity of the lateral velocity observer to changes in vehicle parameters.

Non-linear physical models may be incorporated into the estimation the by the use of the extended Kalman filter [32, 33]. In addition to the extended Kalman filter, [33] examines the use of a non-linear observer for vehicle velocity estimation based on advanced friction models and compares the result to that of the extended Kalman filter. Such extended Kalman filter approaches require linearization of the nonlinear equations at each time step, and therefore may not be practical for implementation in commercial applications.

As an alternative to physical model based observer, the kinematic relationships of the vehicle states may be exploited to design a lateral velocity observer. The most commonly used relationship is that of the lateral acceleration assuming constant forward velocity.

$$a_y = \dot{v}_y + v_x r \qquad (2.3)$$

15

Thus the lateral acceleration and yaw rate sensor values provide a means of computing the time derivative of lateral velocity directly, which may be integrated over time to develop an estimate of lateral velocity. Such kinematic model based observers are not sensitive to vehicle parameter changes and accurately estimate in the nonlinear handling range, but may produce noisy estimates and large estimation errors in the presence of any sensor bias [27]. A variety of approaches have been used to overcome these challenges with the kinematic model.

An observer based on longitudinal and lateral kinematics was also presented by Farrelly and Wellstead [27]. The observer has a nonlinear feedback gain that is a function of yaw rate. However, this observer develops large errors when the yaw rate goes to zero. This method was extended by Ungoren, et. al., to include a correction when yaw rate is small using a model based observer [31]. In this case a hard switch between models is made based on yaw rate, which will result in discontinuities in the rate of change of estimated lateral velocity. This approach is similar to that used in this work described in section 3.1.6 Nonlinear Reduced-Order Observer, however smooth switching functions for the observer gain are used to avoid such discontinuities.

Several successful approaches to lateral velocity estimation incorporate both the physical model and kinematic model in the observer structure. Fukada describes the Toyota ESC system in which sideslip is estimated from a combination of a model based observer and integration of the kinematic equation [34]. In addition to estimating lateral velocity, axle lateral forces are also estimated from lateral acceleration and yaw angular acceleration by inverting the lateral force and moment equations. This same approach is

used in this work, as described in section 4.1 Lateral Force Estimation. Fukada shows that the substitution of these direct lateral force estimates into the physical model based observer of equation (2.2) results in the kinematic model based observer. The physical model is incorporated by using a weighted average of the directly estimated forces and forces estimated from a nonlinear tire model. The relative weighting is determined by a nonlinear function of yaw rate deviation from a determined reference value. When yaw rate deviation is small, the lateral force estimate of the physical tire model is weighted more heavily in order to correct integration errors of the kinematic model integration.

Nishio, et. al., also proposed a combination of physical model based observer and kinematic based observer by executing both in parallel and switching between estimates based on a spinout detection algorithm [35]. The spinout detection is computed from tire models and measured lateral acceleration. Integration errors that arise due to sensor drift are corrected by artificially driving estimated sideslip to zero when the sideslip angular velocity (i.e. derivative of lateral velocity) is "extremely small" [35]. Note however that this may cause problems when sideslip peaks during highly nonlinear, transient maneuvers.

Another example of a combination of physical and kinematic models for lateral velocity estimation is the strategy used by the Ford vehicle stability system, presented by Tseng, et. al. [7]. This strategy uses an integration of the physical bicycle model with an observer feedback correction based on the kinematic model.

$$\hat{v}_y = \int_0^t \left[\hat{a}_y - v_x r + k \left(a_y - \hat{a}_y \right) \right] dt \qquad (2.4)$$

Here the observer gain k is in the range $0 < k \leq 1$ and $\hat{a}_y$ is the lateral acceleration computed using the output equation of the bicycle model described in equation (2.2). (Note that this equation has been corrected to the coordinate system used in this dissertation since Tseng, et. al., defines a left-handed coordinate system [7].) If k = 1, the result is a direct integration of the kinematic equation while if k = 0 then the physical bicycle model is simulated. Tseng, et al., explain that the observer gain may be adapted with the "behavior of vehicle dynamics" but provide no strategy for adaptation [7, 36]. The approach used in this research described in section 3.1.6 Nonlinear Reduced-Order Observer is equivalent to equation (2.4). The fundamental difference in the implementation is that this work uses an adaptive observer gain as a function of yaw rate and forward velocity to correct errors of integration of the kinematic equation when the vehicle dynamics are stable.

A similar approach also developed at Ford is also described in U.S. Patent 6,671,595 [37]. The integration of the kinematic equation is filtered with an "Anti-Integration-Drift" high-pass filter and the physical model based estimate is filtered using a "Steady-State-Recovery" low-pass filter. The two estimates are summed to realize the lateral velocity estimate. Thus, the steady state estimate is assumed to not contribute significantly much during non-linear events. However it is not clear that there will not be high-frequency content in the linear range, nor low-frequency content in the non-linear range. For example a vehicle sliding laterally on ice may be well into the nonlinear range of tire forces, yet the vehicle states may be changing slowly.

One challenge to estimating sideslip is that the road bank angle causes a bias in the lateral accelerometer measurement. One algorithm for estimating road bank angle and compensating the lateral acceleration measurement is proposed in Tseng [7]. Fukada corrects the lateral force estimation for bank angle by correcting the reference yaw rate by the measured lateral acceleration [34]. Other methods are included as part of identification schemes described in the next section. Note that in this research work, the vehicle is assumed to operate on a level planar surface. Bank angle estimation is not included since it is beyond the scope of this work and methods for addressing this issue have been described in the literature.

2.3 Real-time Vehicle Parameter Identification Methods

In addition to identifying unmeasureable vehicle states, estimation methods may be employed to identify unknown vehicle parameters. A number of system identification methods are available in the literature for automatic determination of system parameters. These methods are often extended to enable the real-time online parameter estimation that will identify changes in system parameters as they happen. Several of these methods have been applied to vehicle parameter estimation, including [38]:

- Least squares

- Extended Kalman filter

- Maximum likelihood

- Recursive prediction error

All of these methods rely on a model of the vehicle in order to yield a specific set of vehicle parameters. Often the vehicle model relates only to the vertical ride motion of

19

the vehicle or the longitudinal or lateral dynamics of the vehicle. For example, in [39] various vehicle and suspension parameters are identified using the vertical motions of the vehicle. An observer based identification method is used to identify the unsprung mass, pitch moment of inertia and suspension parameters using a "half-car" model of the pitch and heave motions. This method has been shown to be successful to identify nonlinear system parameters such as the nonlinear damping coefficients of the suspension model.

Examples of estimation of relevant vehicle parameters from the longitudinal and lateral vehicle dynamics are discussed in the following subsections.

2.3.1 Estimation From Longitudinal Dynamics

Estimation of vehicle parameters such as total mass have been successfully estimated directly from measured vehicle longitudinal dynamics [40-43]. In theory the vehicle mass can be readily identified from the measured longitudinal acceleration if the traction and braking forces are known. However, lateral accelerometer sensors on board the vehicle are biased due to gravity on a road with a non-zero bank angle. Therefore the primary problem is resolving the effect of the vehicle inertial mass from that of the road grade angle.

On approach to solving this problem is to use additional information from GPS sensors as demonstrated in [40]. Two different approaches are examined. In the first, two sensors are used to directly determine the road grade and correct the lateral acceleration measurement. In a second approach also discussed in [40], a single GPS sensor is used to determine the relative vertical and horizontal velocities and thus an estimate of road grade is obtained.

20

Other approaches using information available from standard vehicle sensors have been proposed by Vahidi [42]. In the first approach an observer is used, while in the second a recursive time-varying least square method with forgetting is used. Both methods rely on the engine speed and engine output torque to determine mass and road grade angle. Simulation results show both approaches to be successful.

In [41], two different applications of Kalman filtering to determine vehicle mass and road grade angle are presented. In the first approach an extended Kalman filter is applied in the case that vehicle speed is measured, but engine traction force at the wheels is not known. In the case where propulsion force may be determined from engine speed and amount of fuel injected in the engine, a simple filter is found to be sufficient to estimate vehicle mass and road grade angle.

Yet another approach to estimating vehicle mass is presented in [43]. In this case the mass is estimated from the longitudinal dynamics, the lateral dynamics and the vertical dynamics. The longitudinal dynamics are used to estimate mass via a recursive least square with the disturbance observer technique. A Kalman filter is used to estimate mass from the lateral dynamics. Finally a dual recursive least square algorithm is used on the vertical motions of the vehicle to estimate mass. Integration of all three techniques is shown to provide a means of mass estimation under arbitrary vehicle maneuvers.

2.3.2 Estimation From Lateral Dynamics

As described above, the vehicle mass may be estimated from the lateral dynamics [43]. Other parameters of interest including yaw moment of inertia and center of gravity height may also be estimated from the lateral dynamics. Time-varying parameters such

as road bank angle may be estimated to remove bias in the lateral accelerometer measurement used for vehicle sideslip estimation.

Deng and Haicen use a Recursive Least Squares with exponential forgetting factor approach to estimate tire cornering stiffness coefficients from vehicle lateral dynamics [23]. The estimates of cornering stiffness are used in turn to update the physical model that serves as a basis for a lateral velocity observer. Since the cornering stiffness estimation depends on the lateral velocity estimate, an interdependency between the observer and the parameter estimator exists and logic and data sanity checks are employed to ensure stability of the combined system. It should be noted that this work uses the same RLS algorithm for cornering stiffness estimation as described in section 5.1 Axle Cornering Stiffness Identification. However the problems due to interdependency of the lateral velocity observer and parameter estimator are avoided since the lateral velocity observer is based primarily on the kinematic model rather than the physical model.

Liu and Peng [30] present a scheme for estimating unknown system states and unknown parameters simultaneously. The scheme re-parameterizes signals into a regression form and a least squares error scheme is applied to estimate unknown parameters. An example application presented includes a handling example in which the bicycle model system matrix parameters are estimated from the vehicle lateral dynamics.

GPS sensors combined with standard vehicle sensors may be used to estimate vehicle states and parameters. Specifically GPS and inertial sensors are used by Ryu [44] to identify tire cornering stiffnesses, weight distribution and yaw moment of inertia.

Both the least squares method and total least squares method are used. In addition the same sensors are used to distinguish suspension roll and road bank angle. The road band bank angle has a bias effect on the lateral accelerometer measurement just as the road grade angle does on the longitudinal acceleration. Ryu [44] also provides a good discussion of the importance of excitation signals necessary for parameter convergence and the resulting errors produced when sufficient excitation is not available.

A means of automatically identifying the vehicle center of gravity location is described in [45]. Both the center of gravity longitudinal position and height are determined directly from the vehicle lateral dynamics. The Multiple Model Switching and Tuning (MMST) method is used to successfully identify these parameters. While simulation results show successful parameter estimation, the computational requirements for such a scheme may make the method prohibitive in commercial applications.

An additional important time varying parameter that may need to be identified is the road friction coefficient μ. A combination of lateral and longitudinal dynamics has been used to successfully estimate vehicle motion, tire forces and road friction coefficient in Ray [46, 47]. A five degree-of-freedom model and a basic tire model are used in an extended Kalman filter to perform the identification. Successful identification of these parameters has been demonstrated via simulation and via field testing on an actual vehicle [47].

Chapter Summary

This chapter provided a review of current literature on passenger car ESC systems, vehicle lateral velocity estimation techniques and approaches to real-time

vehicle parameter identification. The classical bicycle handling model was presented as a typical approach of traditional ESC control strategies for determining desired vehicle response to steering input. ESC strategies in the literature were shown to compare the determined desired states to measurements and estimates of actual vehicle states. These errors in vehicle states are typically used in feedback control strategies such as PID or state feedback control.

Approaches to estimating vehicle lateral velocity using observers based upon both kinematic models and physical models were presented. Some strategies in the literature combine both models in the observer with the goal of realizing the benefits of each simultaneously. Finally a variety of strategies to identifying vehicle parameters from both vehicle longitudinal and lateral dynamics were reviewed. Most strategies employ some form of recursive least squares estimation or extended Kalman filter.

CHAPTER THREE

SLIP ANGLE ESTIMATION

The ESC algorithm presented in this dissertation relies on an estimation of lateral slip angle for each axle. The vehicle lateral velocity is required to estimate slip angle of the axles, and this value must be estimated as described below since it cannot be measured directly. The estimation of lateral velocity and slip angles is therefore a critical part of the ESC strategy as shown in Figure 1.1. A detailed view of this portion of the control strategy is shown in Figure 3.1.
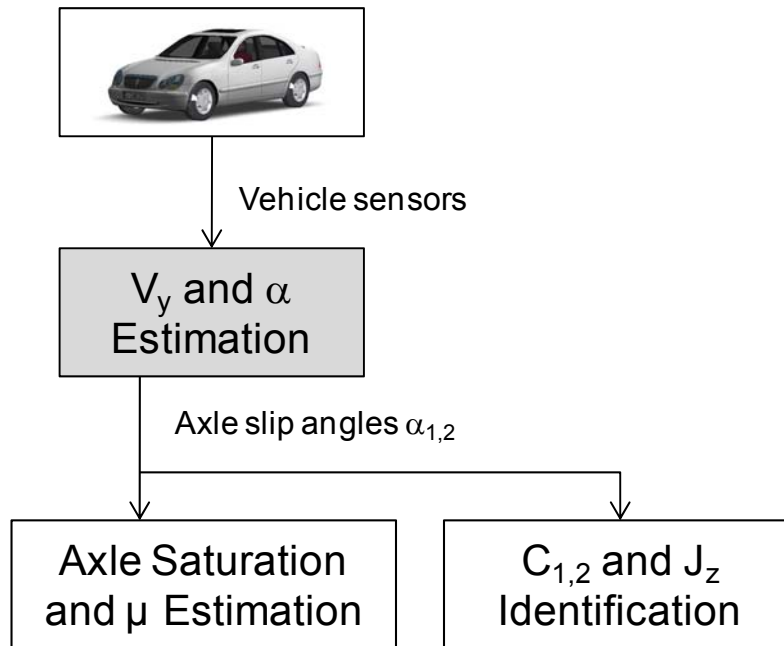
Figure 3.1: Role of Slip Angle Estimation in ESC Strategy

The vehicle sensor values are used in the estimation of lateral velocity and calculation of slip angles as described below in this chapter. The resulting estimated axle

slip angles are subsequently used by the ESC algorithm in both the determination of axle saturation and the online identification of vehicle parameters.

The axle slip angles may be calculated from the vehicle forward velocity, lateral velocity, yaw rate and front road wheel steer angle. The forward velocity is commonly estimated from wheel speeds and is an integral part of the ABS braking system. The front road wheel steer angle may be determined from the measured steering wheel angle and a model of the steering system dynamics. Alternatively a separate sensor may be used for road wheel steer angle, however this is typically prohibitively expensive. Since the estimation of the road wheel steer angle from steering system dynamics is common to all ESC systems, the road wheel angle value is used directly from the vehicle model for simulation. Yaw rate is measured directly, however lateral velocity must be estimated.

A survey of approaches to estimating lateral velocity is presented in this chapter, as well as a novel nonlinear reduced-order observer developed for this work. Additionally the estimation of slip angle along with a lag model for tire relaxation effect is presented.

3.1 Vehicle Lateral Velocity Estimation

3.1.1 Direct Observer

The measured lateral acceleration and yaw rate sensor values of the ESC system may be considered outputs of the bicycle model described in equation (2.1). In this case the complete state space bicycle model is:

$$\dot{\mathbf{x}} = \mathbf{A}\mathbf{x} + \mathbf{B}\delta$$
$$\mathbf{y} = \mathbf{C}\mathbf{x} + \mathbf{D}\delta$$

$$(3.1)$$

where

$$\mathbf{x} = \begin{bmatrix} v_y \\ r \end{bmatrix}$$

$$\mathbf{y} = \begin{bmatrix} a_y \\ r \end{bmatrix}$$

$$\mathbf{A} = \begin{bmatrix} -\dfrac{C_1 + C_2}{mv_x} & \dfrac{-aC_1 + bC_2}{mv_x} - v_x \\ \dfrac{-aC_1 + bC_2}{Jv_x} & -\dfrac{a^2 C_1 + b^2 C_2}{Jv_x} \end{bmatrix}$$

$$\mathbf{B} = \begin{bmatrix} \dfrac{C_1}{m} \\ \dfrac{aC_1}{J} \end{bmatrix}$$

$$\mathbf{C} = \begin{bmatrix} -\dfrac{C_1 + C_2}{mv_x} & \dfrac{-aC_1 + bC_2}{mv_x} \\ 0 & 1 \end{bmatrix}$$

$$\mathbf{D} = \begin{bmatrix} \dfrac{C_1}{m} \\ 0 \end{bmatrix} \tag{3.2}$$

In this case there are two state variables to be observed and two system outputs. Therefore the output equation may be inverted to directly observe the states of the bicycle model. Note that this is possible because the $\mathbf{C}$ matrix is nonsingular due to its structure.

$$\hat{\mathbf{x}} = \mathbf{C}^{-1}[\mathbf{y} - \mathbf{D}\delta] \tag{3.3}$$

As a result, this direct observer makes an estimation of lateral velocity based on measurements of steering angle, lateral acceleration and yaw rate. Figure 3.2 shows the observed lateral velocity for a double lane change maneuver simulated in CarSim at 60 kph. The plot shows that there is good agreement between the actual value from CarSim, the linear model response to the steering input and the value of the direct observer.

Although they are not plotted here, there is also very good agreement between CarSim and the linear model in the lateral acceleration and yaw rate outputs.
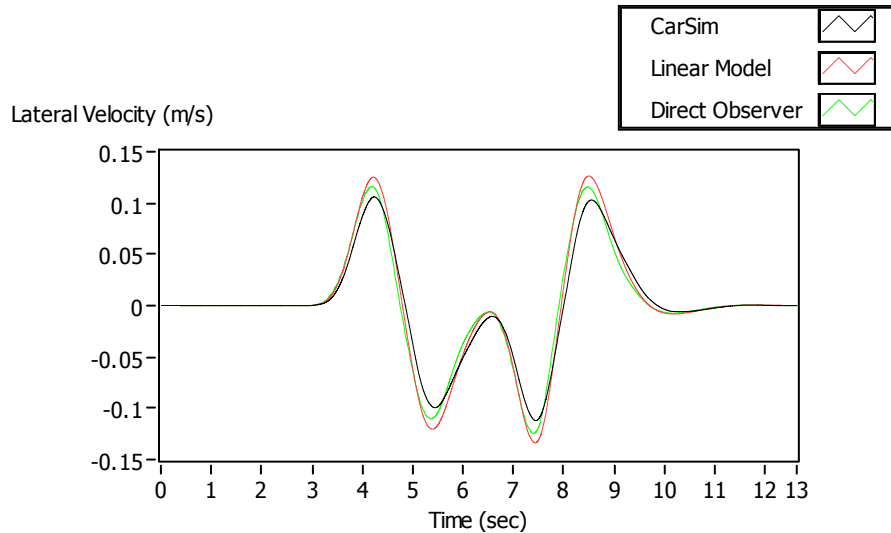
Figure 3.2: Double Lane Change 60 kph, Yaw Velocity Direct Observer

Figure 3.3 and Figure 3.4 show the results for a simulated double lane change maneuver at 120 kph. In this case the model inputs and outputs for both CarSim and the linear model are also plotted. The estimated lateral velocity of the direct observer can be seen to show good performance initially, but develops significant error at ~3 seconds. At this point the lateral acceleration and yaw rate of the linear model deviates significantly from the CarSim model. The reason is that at this speed there is significant lateral load transfer at both axles. The nonlinearity of the cornering stiffness as a function of vertical load in the tire model causes a net reduction in axle cornering stiffness for this lateral load transfer. Since the linear model states are in error at this point, the direct observer fails since the underlying output model has effectively changed. Therefore the direct

28

observer is not able to accurately track vehicle lateral velocity when the extreme vehicle handling behavior deviates from the linear response predicted by the bicycle model. In addition, the direct observer is prone to significant error if any vehicle parameters of the model itself are in error.
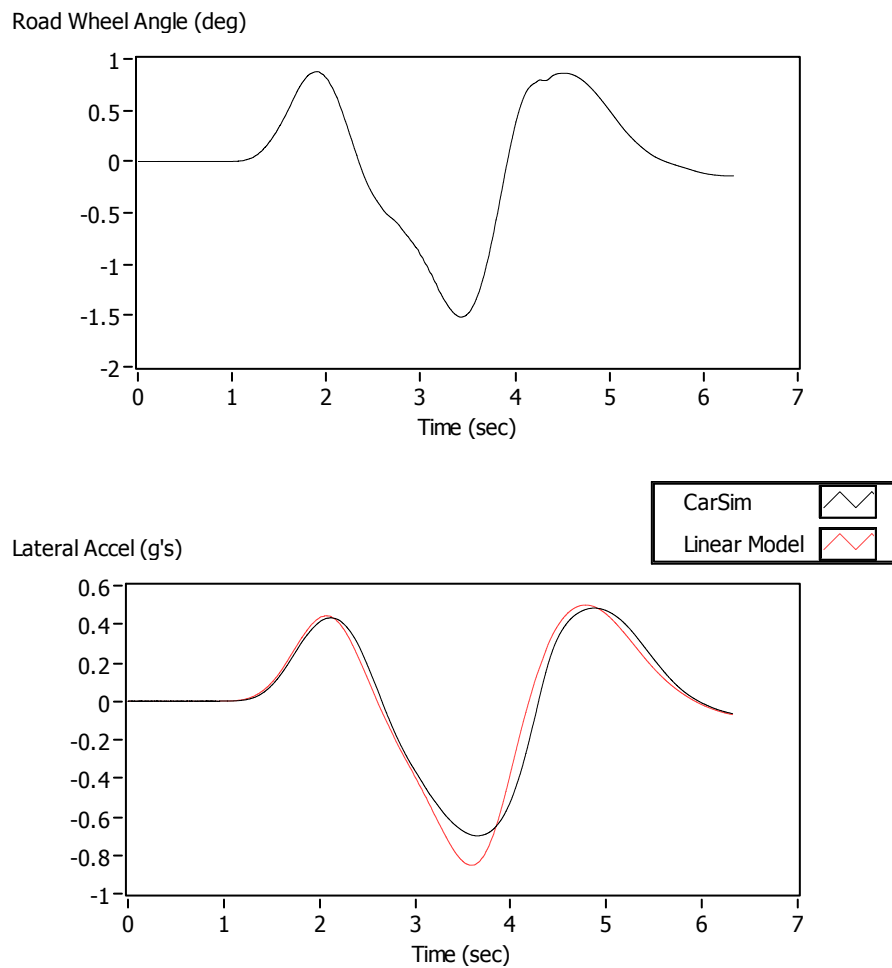
Figure 3.3: Double Lane Change 120 kph, Steering and Lateral Acceleration
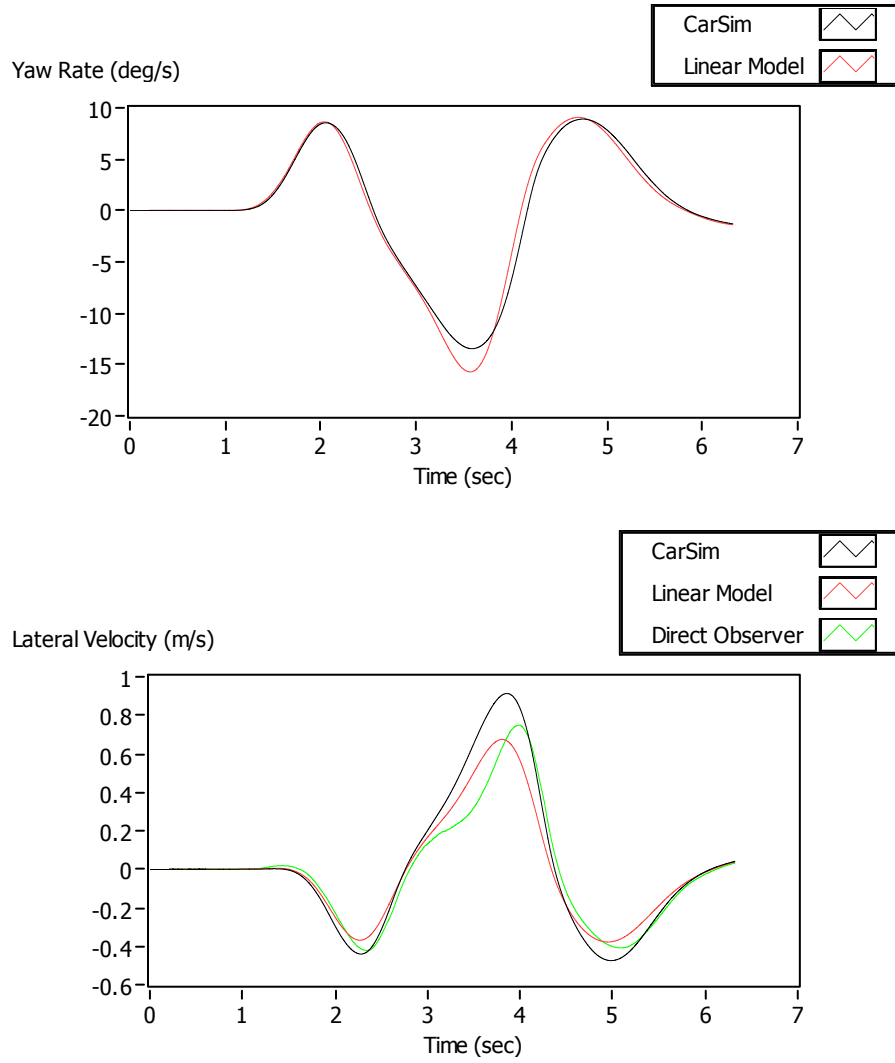
Figure 3.4: Double Lane Change 120 kph, Direct Observer

3.1.2 Full-Order Observer

A traditional full-order observer may be designed using the pole placement method.

$$\dot{\hat{\mathbf{x}}} = \mathbf{A}\hat{\mathbf{x}} + \mathbf{B}\delta + \mathbf{K}\left[\mathbf{y} - \hat{\mathbf{y}}\right]$$
$$= \left[\mathbf{A} - \mathbf{KC}\right]\hat{\mathbf{x}} + \left[\mathbf{B} - \mathbf{KD}\right]\delta + \mathbf{Ky} \qquad (3.4)$$
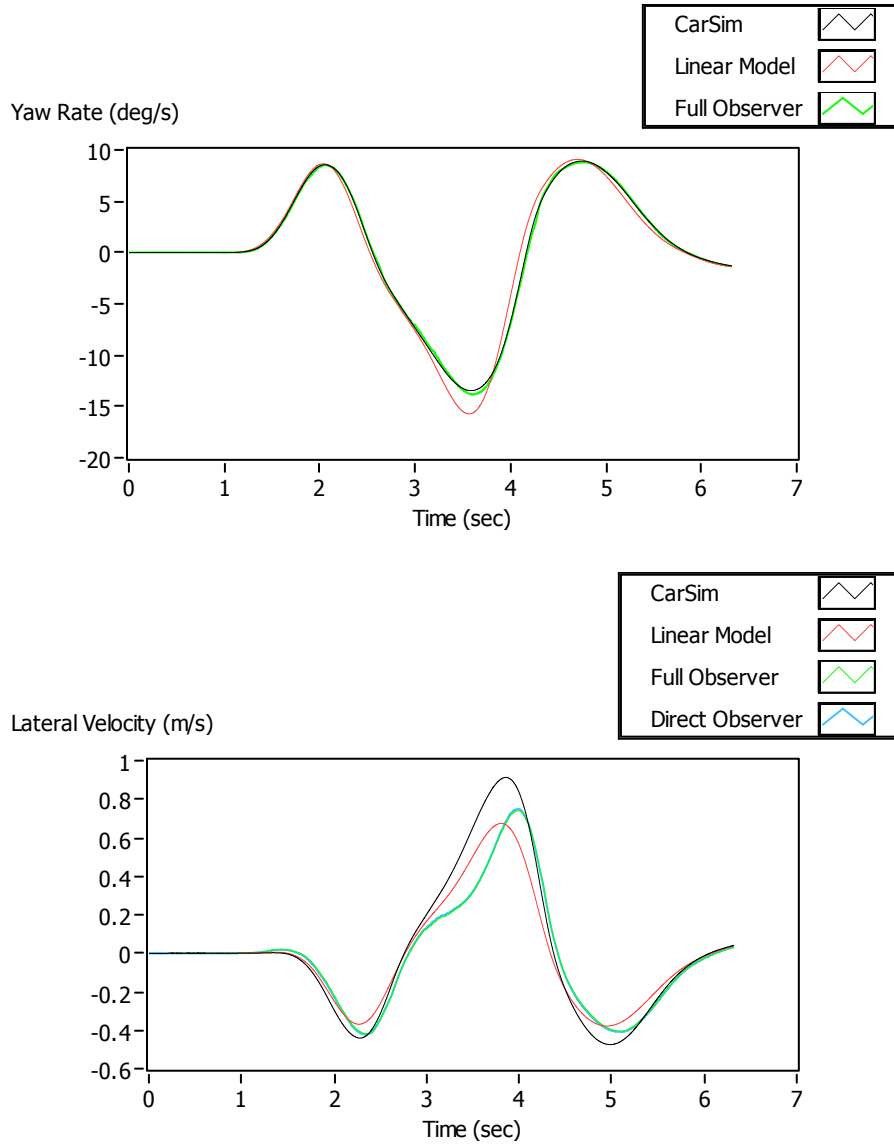
Figure 3.5: Double Lane Change 120 kph, Full-Order Observer, $\lambda_{d1,2}$ = -50

At 120 kph, the plant poles are located at -6.6 +/-0.64i. Therefore the observer gains were designed to place the full-state observer poles at $\lambda_{d1,2} = -50$.

For the double lane change maneuver at 60 kph, the observer states track the states of the simulated vehicle well. Note that this is fairly independent of the observer

pole locations since the linear model and CarSim model are in good agreement at this speed.

As seen in Figure 3.5, at 120 kph the full-state observer estimated lateral velocity tracks that of the direct observer. This is because the fast poles of the observer result in large observer gain and thus the observer minimizes error in model outputs very quickly. The result is effectively the same as that of the direct observer.

Figure 3.6 shows the full-state observer response with the observer poles placed at $\lambda_{d1,2} = -10$, much closer to the system poles. In this case the gain matrix is very small and essentially the observer is running an open-loop model in parallel with the actual system. As a result the estimated states track very closely to the linear model states as seen in the figure. Other gains designed with the observer poles at different real locations or as complex conjugate pairs exhibited similar behavior. Essentially the pole location results in a trade-off between tracking either the direct observer or the linear model states, both of which are in significant error during high lateral acceleration in the maneuver.
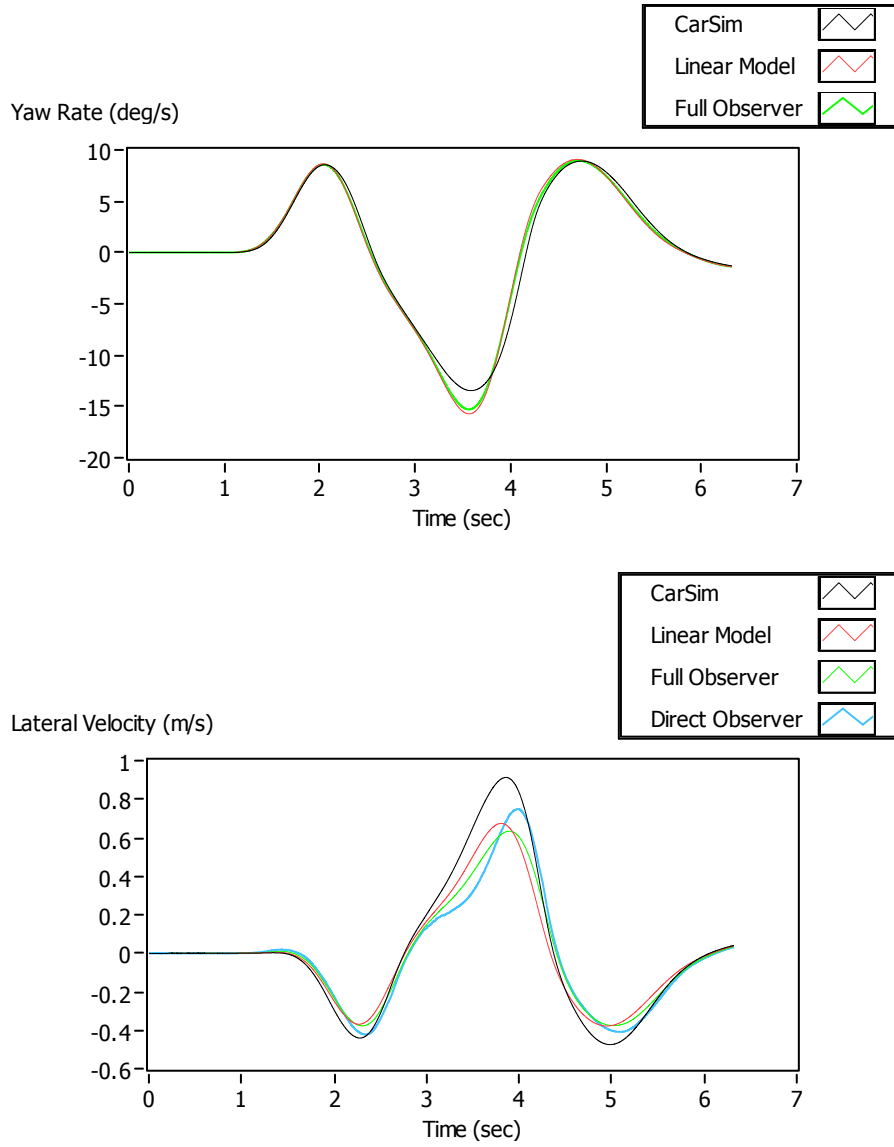
Figure 3.6: Double Lane Change 120 kph, Full-Order Observer, $\lambda_{d1,2} = -10$

3.1.3 Reduced-Order Observer

Typically a reduced-order observer for a system with n states and p outputs estimates n-p of the states, assuming that the other p states are determined directly from the system output equations [48]. In this case since the number of states and outputs are

both 2, $n = p$ and an alternative approach to designing a reduced order observer must be developed. In this case since the yaw rate is measured directly, the reduced-order observer may be designed using an alternative system model that treats the yaw rate as an input:

$$
\begin{aligned}
\dot{v}'_y &= [a_{11}]v'_y + [a_{12} \quad b_{11}]\begin{bmatrix} r \\ \delta \end{bmatrix} \\
a'_y &= [c_{11}]v'_y + [c_{12} \quad d_{11}]\begin{bmatrix} r \\ \delta \end{bmatrix}
\end{aligned}
\tag{3.5}
$$

The result is a first order observer for the estimated lateral velocity:

$$
\begin{aligned}
\dot{\hat{v}}_y &= [a_{11}]\hat{v}_y + [a_{12} \quad b_{11}]\begin{bmatrix} r \\ \delta \end{bmatrix} + k[a_y - \hat{a}_y] \\
&= [a_{11} - kc_{11}]\hat{v}_y + [a_{12} - kc_{12} \quad b_{11} - kd_{11}]\begin{bmatrix} r \\ \delta \end{bmatrix} + ka_y
\end{aligned}
\tag{3.6}
$$
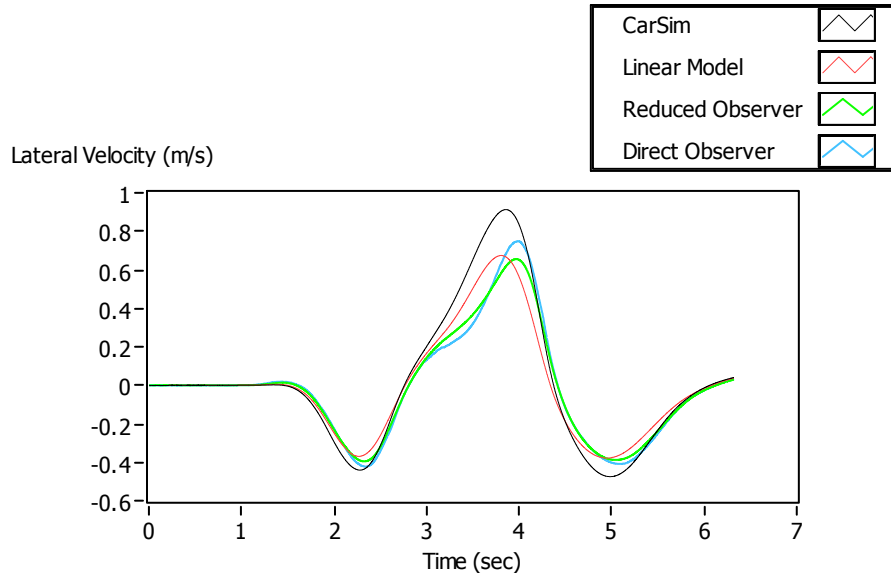
Figure 3.7: Double Lane Change 120 kph, Reduced-Order Observer, $\lambda_d = -10$

As with the full state observer, setting the observer pole at $\lambda_d = a_{11} - kc_{11} = -50$ results in an observer that directly tracks the state of the direct observer. Also similar to the full state observer, setting the observer pole at -10 results in an observer that tracks the linear model as seen in Figure 3.7. There is more deviation from the linear model than was observed with the full-state observer, however this can be attributed to the fact that the yaw rate is forced to be the same as that of the simulated vehicle.

An interesting phenomenon is observed when the observer pole is set to zero, resulting in an observer gain k = 1. In this case, the reduced-order observer yields a lateral velocity estimate that exactly matches the actual value of the simulated vehicle as seen in Figure 3.8.
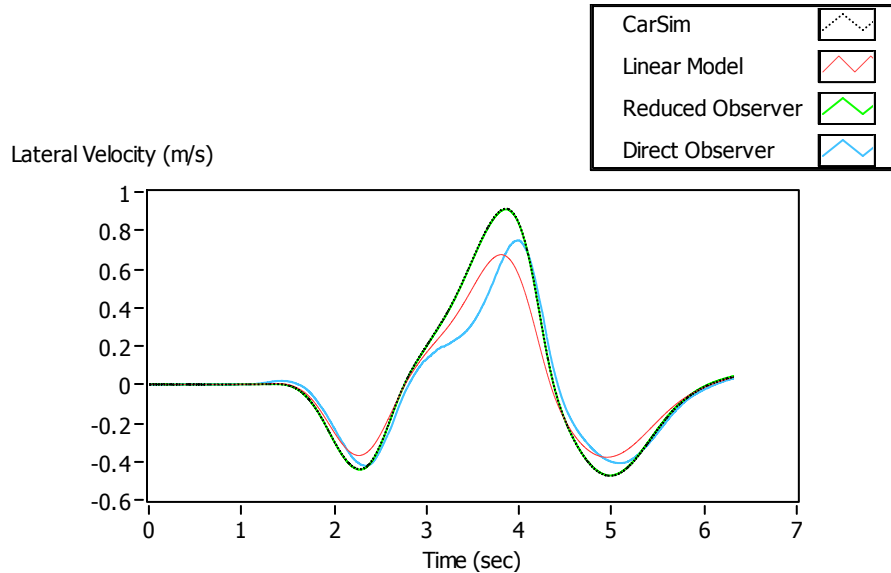
Figure 3.8: Lane Change 120 kph, Reduced-Order Observer, $\lambda_d = 0$

Note that for the vehicle model:

$$c_{11} = a_{11}$$
$$c_{12} = a_{12} + v_x \qquad (3.7)$$
$$d_{11} = b_{11}$$

Therefore when k = 1:

$$\dot{\hat{v}}_y = \left[a_{11} - kc_{11}\right]\hat{v}_y + \left[a_{12} - kc_{12} \quad b_{11} - kd_{11}\right]\begin{bmatrix} r \\ \delta \end{bmatrix} + ka_y$$
$$= -v_x r + a_y \qquad (3.8)$$

This is simply a restatement of the kinematic relationship $a_y = \dot{v}_y + v_x r$.

Unfortunately, however, the result is that the observer is simply an open-loop integrator and therefore any measurement error such as noise or especially bias will result in an incorrect estimate of lateral velocity.
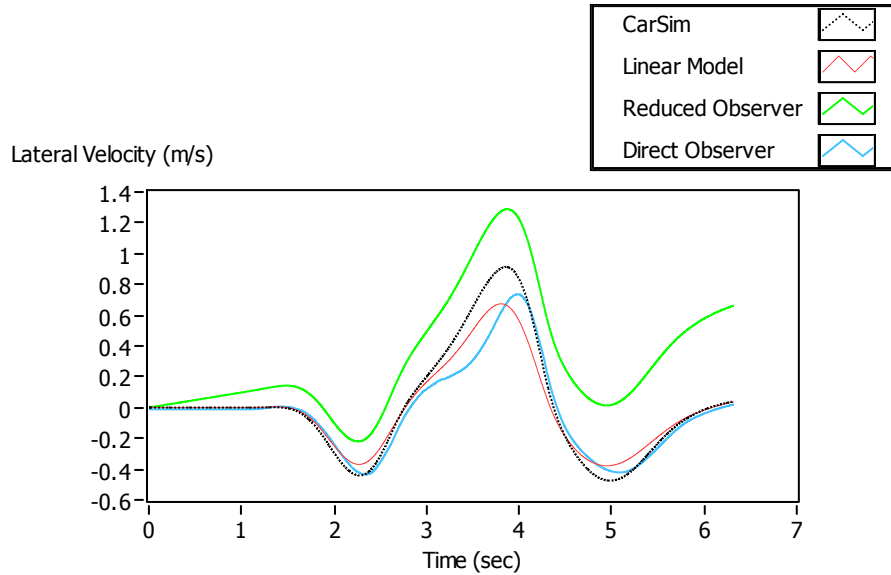
Figure 3.9: Lane Change 120 kph, Reduced-Order Observer, $\lambda_d = 0$, a_y Measurement Bias of 0.01 g

Simulation results with a bias of 0.01 g added to the lateral acceleration value are shown in Figure 3.9. However, this kinematic relationship is the motivation for an alternative reduced-order observer developed in the following section.

3.1.4 Kinematic Reduced-Order Observer

The idea behind the second approach to a reduced-order observer is to combine the kinematic relationship $a_y = \dot{v}_y + v_x r$ with the output feedback correction of an observer structure. As seen in the previous section integrating the lateral acceleration to get lateral velocity is prone to substantial error due to measurement noise and bias. However adding an output feedback correction can help limit the amount of error introduced during integration.

$$
\begin{aligned}
\dot{\hat{v}}_y &= a_y - v_x r + k\left[a_y - \hat{a}_y\right] \\
&= -kc_{11}\hat{v}_y + \begin{bmatrix} 1+k & -\left(v_x + kc_{12}\right) \end{bmatrix} \begin{bmatrix} a_y \\ r \end{bmatrix} - kd_{11}\delta
\end{aligned}
\tag{3.9}
$$

Therefore the observer gain may again be designed by placement of the observer pole at $\lambda_d = -kc_{11} = -10$. The estimation of this observer is identical to that of the physical model-based reduced-order observer shown in Figure 3.7. Note that if the first lateral acceleration a_y term in equation (3.9) is replaced with the physical model output a_y' of equation (3.5), the result is equivalent to the physical model-based observer presented in equation (3.6). As a result, the two reduced-order observers produce similar results for the same designed pole location, even though the actual value of observer gain is different for each observer. The two forms of reduced-order observers thus produce equivalent results with the same tradeoff in gain selection.

37

3.1.5 Steady State Gain Kalman Filter

The linear bicycle model may be reformulated as a stochastic model with zero-mean process random noise **w**(t) and measurement random noise **v**(t).

$$\dot{\mathbf{x}} = \mathbf{A}\mathbf{x} + \mathbf{B}\delta + \mathbf{w}(t)$$
$$\mathbf{y} = \mathbf{C}\mathbf{x} + \mathbf{D}\delta + \mathbf{v}(t)$$

(3.10)

In this case the Kalman filter can be used to implement an optimal observer with respect to the noise characteristics of **w**(t) and **v**(t). To implement the Kalman filter, the auto-covariance matrices of **w**(t) and **v**(t) must be specified:

$$\mathbf{Q} = E\left\{\mathbf{w} \cdot \mathbf{w}^T\right\}$$
$$\mathbf{R} = E\left\{\mathbf{v} \cdot \mathbf{v}^T\right\}$$

(3.11)

In theory the process noise and measurement noise would be measured and the auto-covariances computed directly. In practice this is very difficult to do, especially for the process noise **w**(t) as this often cannot be measured directly. As a result the **Q** and **R** matrices may be considered to be tuning parameters for the Kalman filter.

In order to evaluate the behavior of the Kalman filter for observing the vehicle state variables, a steady state Kalman gain was designed and implemented using the LabVIEW Control Design and Simulation module functions. The **Q** and **R** matrices were specified as diagonal matrices with equal values along the diagonal of each.

$$\mathbf{Q} = Q\mathbf{I}$$
$$\mathbf{R} = R\mathbf{I}$$

(3.12)

This simplistic approach was used to "tune" the Kalman filter by the relative weighting of the scalar values Q and R. The response to the double lane change maneuver with Q weighted more than R by two orders of magnitude may be seen in

Figure 3.10. Note that zero-mean white noise was added to the measured lateral acceleration and yaw rate signals obtained from the vehicle simulation. The more heavily weighted Q matrix indicates low confidence in the underlying model, but greater confidence in the output measurements. As a result the estimated lateral velocity is very close to that determined by the direct observer, seen in Figure 3.4.
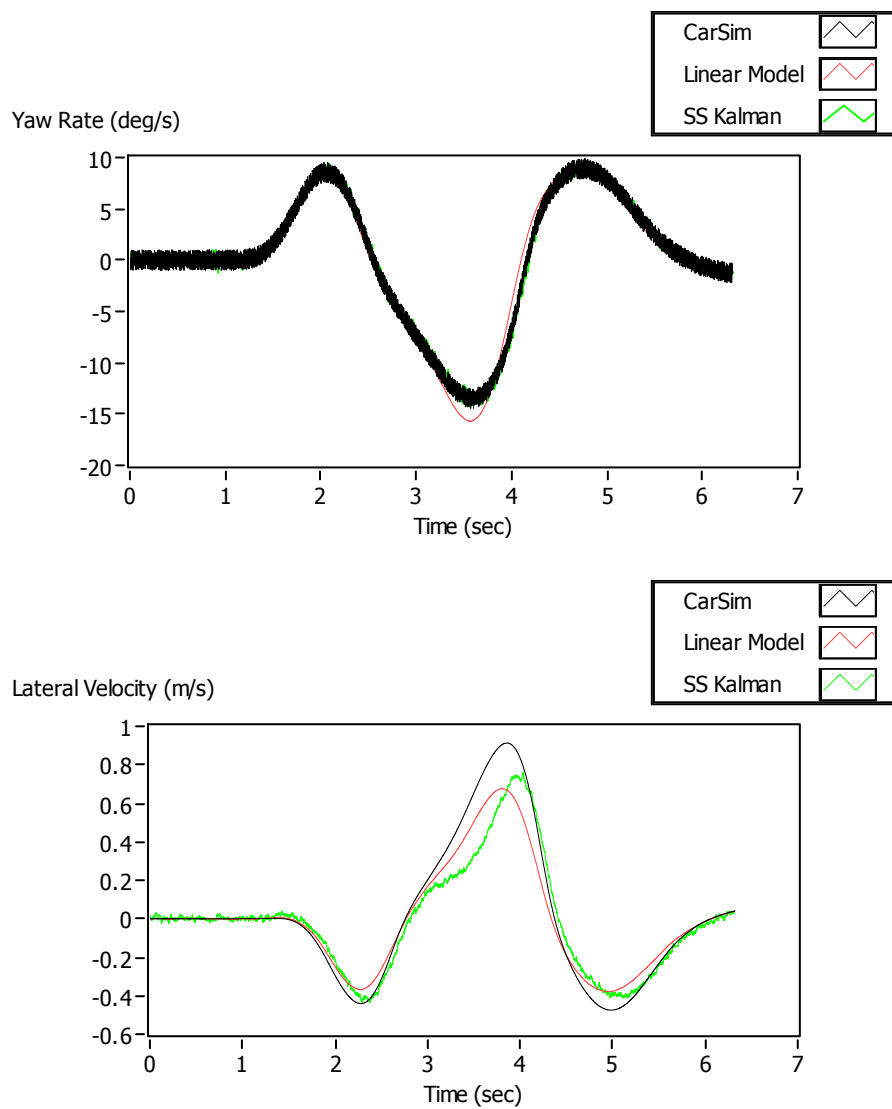
Figure 3.10: Lane Change 120 kph, Kalman Filter, Q = 100, R = 1

The results of a second simulation of the Kalman filter with R weighted two orders of magnitude higher than Q is shown in Figure 3.11. In this case the weighting indicates high confidence in the process model but low confidence in the measured outputs. As a result the model very closely tracks the linear model response.
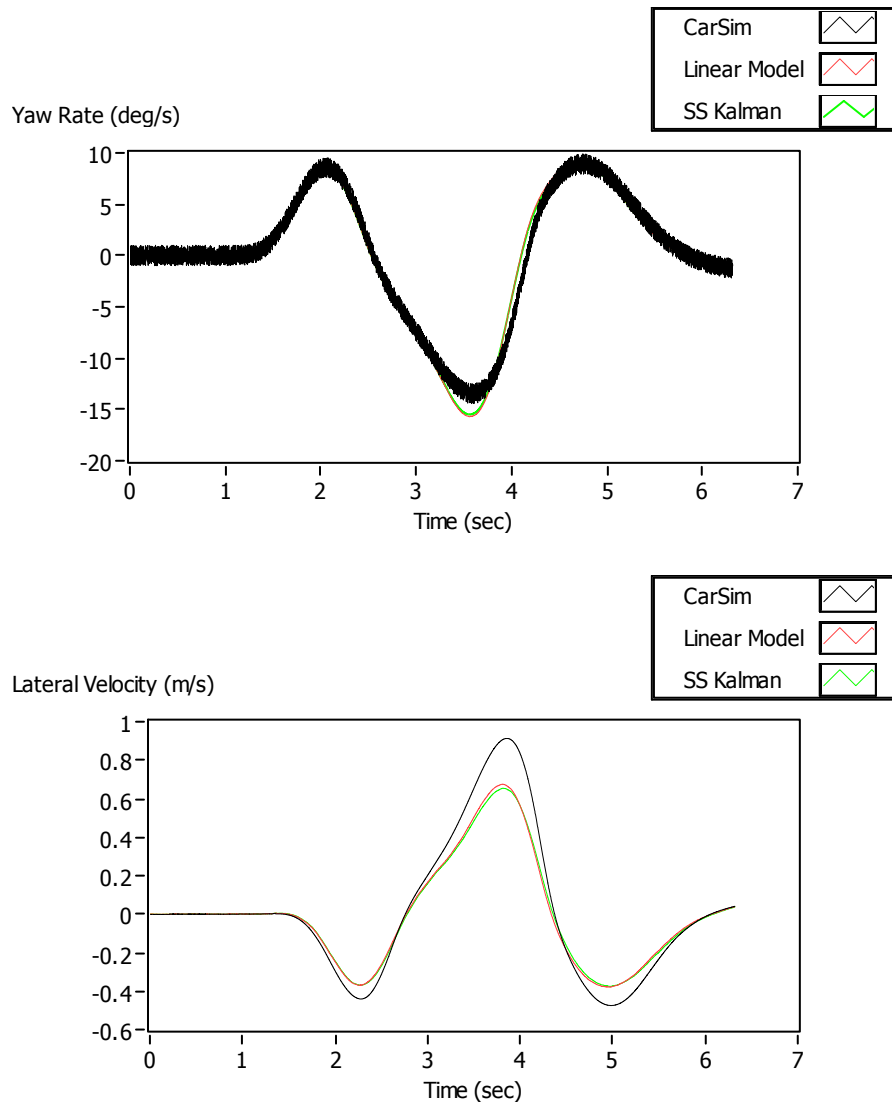
Figure 3.11: Lane Change 120 kph, Kalman Filter, Q = 1, R = 100

Although the Kalman filter provides the optimal observer gain with respect to the noise models, the actual implementation involves the same trade-offs with regard to model accuracy as with the other observer models.

3.1.6 Nonlinear Reduced-Order Observer

A number of approaches have been employed to estimate vehicle lateral velocity. One approach is to use the kinematic relationship between rate of change of lateral velocity, lateral acceleration and yaw rate assuming constant vehicle forward velocity [10]:

$$\dot{\hat{v}}_y = a_y - v_x r \tag{3.13}$$

Since the lateral acceleration and yaw rate are measured directly, the lateral velocity may be found by directly integrating the kinematic relationship.

$$\hat{v}_y = \int_0^t \left(a_y - v_x r \right) dt \tag{3.14}$$

However, the resulting estimate is prone to significant error should there be any sensor bias or noise, as demonstrated above. To prevent this buildup of error, the use of a feedback term to correct the estimated lateral velocity from any sensor bias error has been suggested [7]. The implementation in this research is similar but has a slightly different form with emphasis placed on integration of the kinematic relationship.

$$\hat{v}_y = \int_0^t \left[a_y - v_x r + k \left(a_y - \hat{a}_y \right) \right] dt \tag{3.15}$$

The parameter k is the observer feedback gain and is in the range $-1 \le k \le 0$. The estimated lateral acceleration is determined from the measured states and the bicycle model, thus comprising a reduced-order observer:

$$\hat{a}_y = \left[-\frac{C_1 + C_2}{mv_x} \right] \hat{v}_y + \left[\frac{-aC_1 + bC_2}{mv_x} \quad \frac{C_1}{m} \right] \begin{bmatrix} r \\ \delta \end{bmatrix} \tag{3.16}$$

Note that if the feedback gain k is 0, the result is the open loop integrator of equation (3.14). The advantage of this approach is that the kinematic relationship is independent of the vehicle model and any modeling errors, and produces accurate lateral velocity estimates even when the vehicle is operating beyond the linear range of the model. The disadvantage is that the estimate is prone to errors in sensor bias and noise as previously discussed. If the feedback gain is -1, the state estimate is simply that of the reduced-order observer.

Since most non-linear handling events take place over short time durations, the integration errors will be minimal if an accurate lateral velocity is known at the beginning of the event. Since most driving is done at very low lateral acceleration, the feedback gain term may be utilized to correct any previous integration errors. Thus the desired non-linear observer uses a switching scheme with the feedback gain set to -1 at low lateral acceleration and set to 0 at high lateral acceleration:

$$k = \frac{1}{\pi} \arctan \left[10 \left(|v_x r| - 0.2 \right) \right] - 0.5 \tag{3.17}$$

A lateral acceleration of 0.2 m/s^2 is chosen as most non-linear handling events happen when lateral acceleration is above this value. The longitudinal velocity is multiplied by yaw rate instead of using the direct lateral acceleration measurement to ensure that non-linear behavior during a complete loss of traction is still captured (e.g. a spinout).

The resulting nonlinear reduced-order observer has the desirable property of accurately tracking lateral velocity during transient handling events that occur at high lateral acceleration. However since such events typically happen only over short time durations, the observer is able to avoid integration bias errors. An example of the lateral velocity estimation is shown in Figure 3.12. The simulated maneuver is a high speed double lane change. At 3.5 to 4 seconds in the simulation, the vehicle states exceed the linear range of the bicycle model, and therefore a traditional observer would produce errors in lateral velocity estimation.
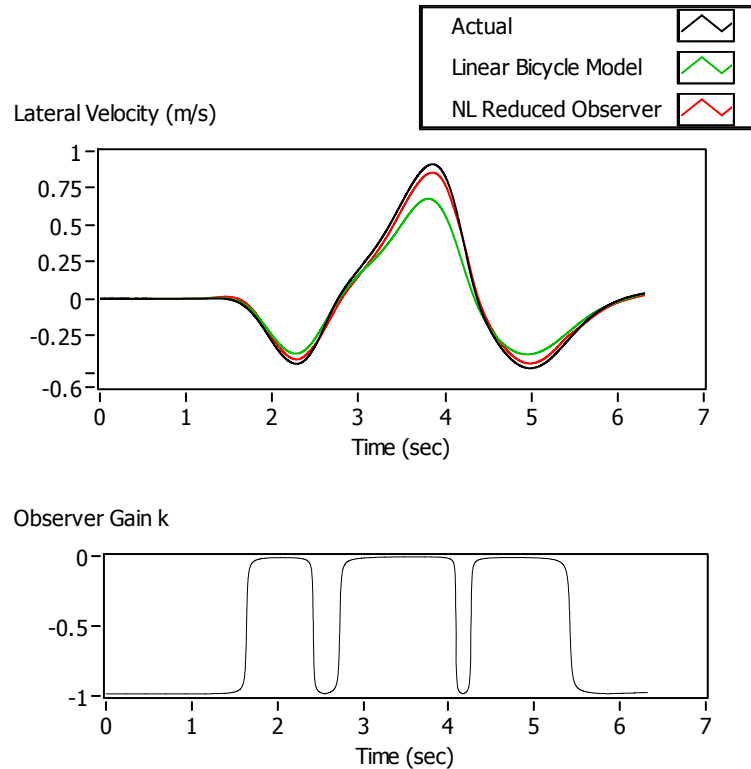
Figure 3.12: Nonlinear Reduced-Order Lateral Velocity Observer Estimate in Double Lane Change

Note that the results shown in Figure 3.12 utilize the nonlinear gain function shown in equation (3.17). The arctangent function is used to ensure a smooth switching behavior, however a simpler function or lookup table could also be used for actual implementation in a controller with limited computing resources. For the ESC control system developed, a simple piecewise linear function was used for the feedback gain k:

$$k = \begin{cases} \dfrac{|v_x r|}{0.2} - 1, & |v_x r| < 0.2 \\ 0, & |v_x r| \geq 0.2 \end{cases}$$

(3.18)

While the modified feedback gain function does not provide the smooth behavior of the arctangent function, the modified function is more realistic for implementation on a vehicle Electronic Control Unit (ECU). This modified piecewise linear feedback gain function was used in the ESC controller described in subsequent chapters.

3.2 Axle Slip Angle Estimation

Once the vehicle lateral velocity has been estimated using the nonlinear reduced order observer described, the axle slip angles may be calculated directly from kinematic relationships [14].

$$\alpha_1 = \arctan\left(\frac{v_y + ar}{v_x}\right) - \delta$$

$$\alpha_2 = \arctan\left(\frac{v_y - br}{v_x}\right)$$

(3.19)

Tire forces do not respond to changes in slip angle immediately, but rather develop shear forces as the tire deforms. For this reason, a first order lag is often used to model shear forces [49].

44

$$\dot{\tau}_i = \frac{v_{yi} - \tau_i |v_{xi}|}{L_{yi}}$$

$$\alpha_{Li} = \arctan(\tau_i)$$

(3.20)

Here v_{yi} and v_{xi} are the coordinates of the velocity vector of the wheel resolved on the wheel reference frame. L_{yi} is the tire relaxation length for tires on axle i, resulting in a first order lag with time constant $\tau_i = \frac{L_{yi}}{v_{xi}}$. Finally, α_{Li} is the lagged slip angle that may subsequently be correlated with lateral force and compared to the theoretical tire lateral force characteristics.

For the two axle vehicle with steering on the front wheel only these vectors are as follows:

$$v_{y1} = (v_y + ar)\cos\delta - v_x \sin\delta$$

$$v_{x1} = v_x \cos\delta + (v_y + ar)\sin\delta$$

$$v_{y2} = v_y - br$$

$$v_{x2} = v_x$$

(3.21)

Since the ESC control system should restrict the slip angles to relatively small values, linearized equations for the lagged axle slip angles may be used to reduce the computational burden. Note that since typically $v_x \gg (v_y + ar)\delta$, the second term in the equation for v_{x1} may be neglected.

$$v_{y1} \approx v_y + ar - v_x \delta$$

$$v_{x1} \approx v_x$$

$$\alpha_{Li} \approx \tau_i$$

(3.22)

The results are linear first order equations in slip angle for each axle. Note that the absolute value of velocity used in the CarSim model is dropped since the ESC system is only considered for forward vehicle velocities.

$$\dot{\alpha}_{L1} = \frac{v_y + ar - v_x\delta - v_x\alpha_{L1}}{L_{y1}}$$

$$\dot{\alpha}_{L2} = \frac{v_y - br - v_x\alpha_{L2}}{L_{y2}}$$

(3.23)

The tire models used in CarSim simulations in this work have a tire relaxation length of 0.565 m. As a result the lagged slip angles have a time constant of ~20 milliseconds at 100 kph and ~40 milliseconds at 50 kph. Since driver steer input may change rapidly, time constants of this order are significant when the axle slip angles are compared to axle lateral forces as discussed in Chapter Four. Therefore the lagged axle slip angle model is used in the developed ESC control strategy.

Chapter Summary

This chapter presented a novel nonlinear reduced-order lateral velocity observer used in the estimation of axle slip angles. First a review of different approaches to estimating vehicle lateral velocity was presented and the relative merits of each approach examined with a simulated double lane change maneuver. The nonlinear reduced-order observer with dynamic adaptation of feedback gain was shown to accurately track lateral velocity during transient nonlinear maneuvers, yet eliminate sensor noise and bias integration errors over time. The estimated lateral velocity was used to estimate slip angle of each axle, and a first-order slip angle lag model was used to account for tire relaxation effects.

CHAPTER FOUR

LATERAL FORCE AND FRICTION ESTIMATION

The ESC algorithm utilizes an estimation of lateral force for each axle, which is determined using linear force and angular momentum equations. The estimated axle slip angles and lateral forces are used to determine axle lateral force saturation and also provide a means of estimating coefficient of friction. These components of the complete ESC strategy are shown in Figure 1.1. A detailed view of axle force estimation portion of the control strategy is shown in Figure 4.1. Normal, lateral and longitudinal forces are estimated from vehicle sensor measurements as described below in 4.1 Lateral Force Estimation.
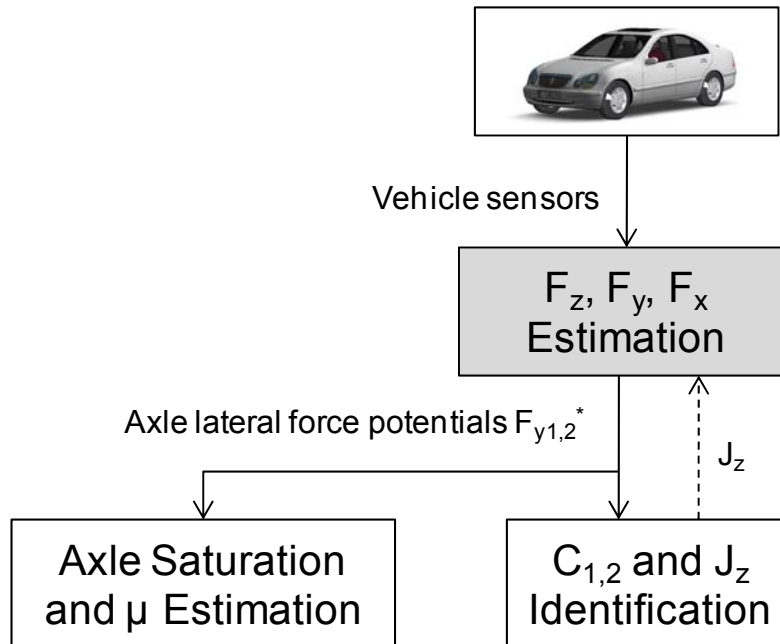
Figure 4.1: Role of Axle Lateral Force Estimation in ESC Strategy

47

The estimation of axle lateral force may also make use of the vehicle yaw moment of inertia J_z identified by the real-time parameter identification approach described in Chapter Five. From the force estimates the lateral force potential of each axle is determined as described in 4.2 Estimation of Lateral Force Potential.

Once the axle slip angle and lateral force estimates are known, axle saturation may be detected by examination of the lateral force characteristic curve. A detailed view of axle saturation and coefficient of friction estimation portion of the control strategy is shown in Figure 4.2.
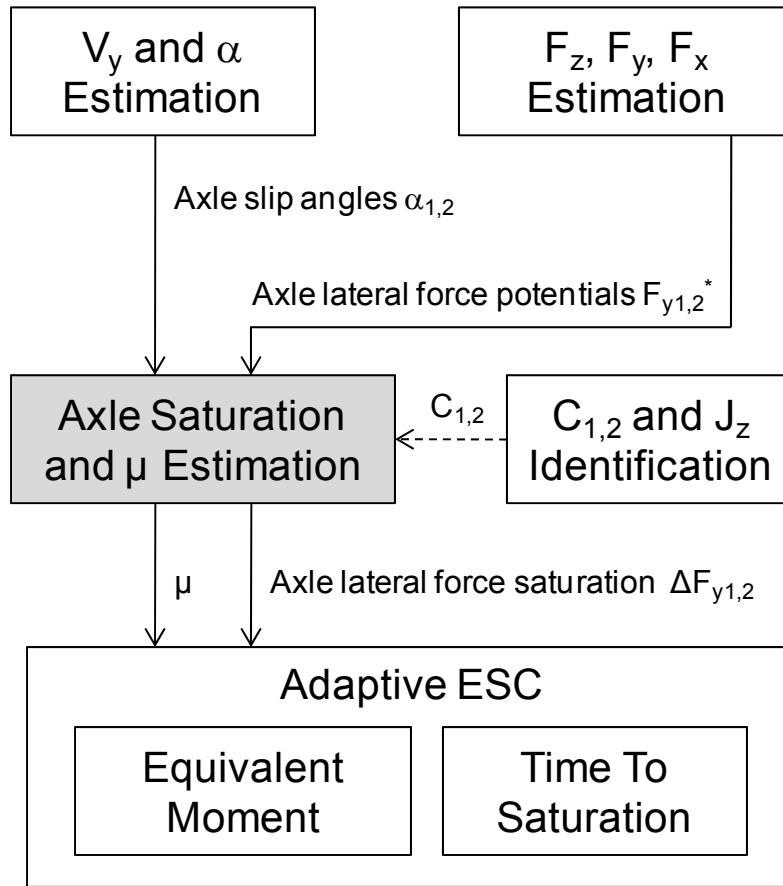
Figure 4.2: Role of Axle Saturation and Coefficient of Friction Estimation in ESC Strategy

The theoretical linear lateral force response of the axles are computed from the estimated axle slip angles $\alpha_{1,2}$ described in Chapter Three and identified axle cornering stiffness coefficients $C_{1,2}$ described in Chapter Five. The actual lateral force potential of each axle is compared to the theoretical linear lateral force response to determine axle saturation. When saturation is detected, the road/tire coefficient of friction may also be estimated. The detection of axle saturation and estimation of coefficient of friction is described in 4.3 Axle Saturation and Friction Estimation. The axle lateral force saturation and estimated coefficient of friction are then used in the ESC strategy described in Chapter Six.

4.1 Lateral Force Estimation

The linear force equation in the lateral direction and the angular moment equation together provide a unique solution for the lateral force values of the two axles. The equations result directly from a summation of forces in the lateral direction and summation of yaw moments, resulting in a system of linear equations.

$$\begin{bmatrix} ma_y \\ J\dot{r} \end{bmatrix} = \begin{bmatrix} 1 & 1 \\ a & -b \end{bmatrix} \begin{bmatrix} F_{y1}\cos\delta \\ F_{y2} \end{bmatrix} - \begin{bmatrix} 1 \\ a \end{bmatrix} F_{x1}\sin\delta \qquad (4.1)$$

While the vehicle lateral acceleration is available directly from a sensor, the yaw angular acceleration must be found either by numerically differentiating the yaw rate signal or from an additional angular accelerometer. Note that here positive F_{x1} is the braking force of the front axle in the $-x$ direction, therefore a negative sign is used where normally positive F_x would add to lateral force.

49

Inverting the system of equations (4.1) results in a direct estimation of axle lateral forces. Note that this same approach for axle lateral force estimation was proposed by Fukada [34].

$$\begin{bmatrix} F_{y1}\cos\delta \\ F_{y2} \end{bmatrix} = \begin{bmatrix} \dfrac{mb}{a+b} & \dfrac{J}{a+b} \\ \dfrac{ma}{a+b} & -\dfrac{J}{a+b} \end{bmatrix} \begin{bmatrix} a_y + \dfrac{F_{x1}}{m}\sin\delta \\ \dot{r} + \dfrac{aF_{x1}}{J}\sin\delta \end{bmatrix} \tag{4.2}$$

The force balance equations must also include any additional forces and moments generated from longitudinal drive traction or braking forces at the wheels. The drive and traction forces of the front wheels contribute to the lateral force of the steered wheels, and any ESC differential braking produces an additional moment that must be included in the moment equation.

In order to calculate the longitudinal forces at each wheel, the individual wheel dynamics must be considered. In order to determine brake force due to braking, the wheel-end brake chamber pressure commanded by the ABS system is used.
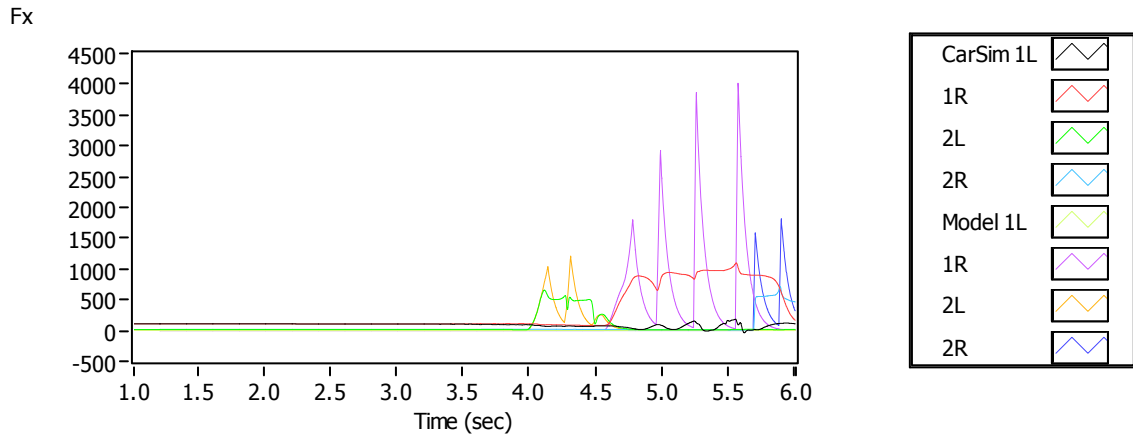
Figure 4.3: Brake Force Estimation without Wheel Dynamics

50

If wheel dynamics are ignored, the longitudinal brake force of the tire is directly proportional to the brake pressure applied. However, as seen in Figure 4.3 ignoring the wheel dynamics leads to significant errors in brake force estimation.

4.1.1 Non-Driven Wheel Braking Dynamics

The torques and forces acting on a wheel in the spin direction are shown in Figure 4.4. T_b is the applied brake torque on the wheel, T_d is the drive torque applied to wheels of driven axles, ω is the wheel angular spin velocity and r is the effective rolling radius of the wheel which is assumed to be a known constant parameter.
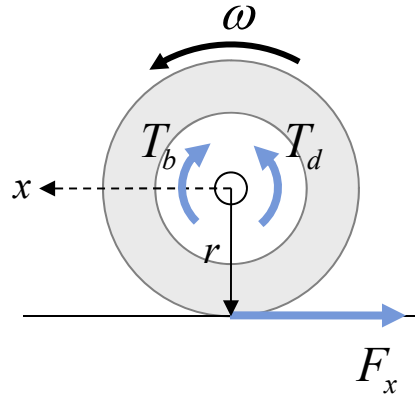
Figure 4.4: Wheel Braking Dynamics

For non-driven wheels, the wheel dynamics due to braking may be modeled as:

$$\begin{aligned} I_w \dot{\omega} &= rF_x - T_b \\ &= rF_x - k_b P_b \end{aligned}$$

(4.3)

Therefore if wheel spin acceleration is measured or wheel spin speed is measured and acceleration determined by numerical differentiation, the braking force may be determined as:

$$F_x = \frac{I_w}{r}\dot{\omega} + \frac{k_b}{r}P_b \qquad (4.4)$$

Here the brake pressure must be estimated by applying an appropriate first order model of the braking system to the brake pressure command output of the ABS controller. Figure 4.5 shows the estimation of brake force with the wheel dynamics included. Note that the rear wheel brake force is correctly estimated, however the front wheel longitudinal force estimation still shows large errors because drivetrain dynamics are not included in the model.

Fx
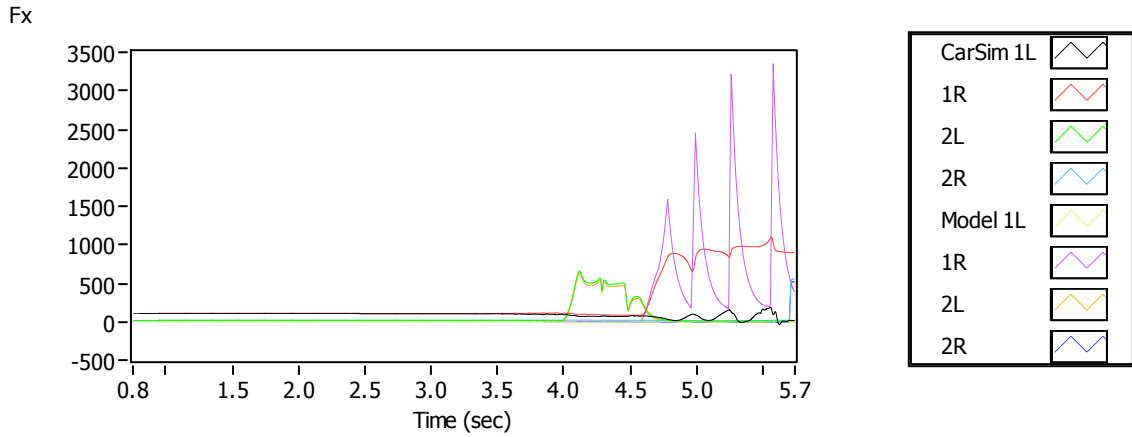
Figure 4.5: Brake Force Estimation with Wheel Dynamics

4.1.2 Driven Wheel Braking Dynamics

Note also that for the driven wheels, the drive torque and drivetrain inertia must also be added to the relationship provided in equation (4.3) [10]. The wheel dynamics due to braking and drive traction of the driven wheels may be modeled as:

$$\begin{aligned}
I_{eff}\dot{\omega} &= rF_x - T_b + T_d \\
&= rF_x - k_b P_b + T_d
\end{aligned} \qquad (4.5)$$

52

Here T_d is the drive traction from the differential. From a simple model of an open differential, the drive torque to either of the drive wheels may be modeled as a function of torque generated at the transmission output:

$$T_{dL,R} = \frac{1}{2}T_{trans}N_{diff}E_{diff}$$ (4.6)

N_{diff} is the differential gear ratio and E_{diff} is the differential efficiency ratio. Note that the transmission output torque is normally available from the powertrain controller since the engine torque output is estimated and the transmission gear ratios are known.

I_{eff} is the effective combined inertia of all drivetrain components from the engine output to the wheels. For a simple model including only transmission inertia and wheel inertia:

$$I_{eff} = I_w + \frac{1}{2}I_{trans}N_{diff}{}^2$$ (4.7)

Therefore if wheel spin acceleration is measured or wheel spin speed is measured and acceleration determined by numerical differentiation, the braking force may be determined from:

$$F_x = \frac{I_{eff}}{r}\dot{\omega} + \frac{k_b}{r}P_b - \frac{1}{2r}T_{trans}N_{diff}E_{diff}$$ (4.8)

Figure 4.6 shows the estimation of brake forces for all four wheels. The brake force of the front wheels is not estimated correctly with the inclusion of the drivetrain dynamics.

Note that there is a slight offset between actual and estimated longitudinal forces. This is due to the rolling resistance of the tires which is not modeled in the force

estimation. This could be included based on a simple tire model, however this is a minor effect on longitudinal force and in general applies evenly to tires on both sides of the vehicle and thus contributes no additional yaw moment.
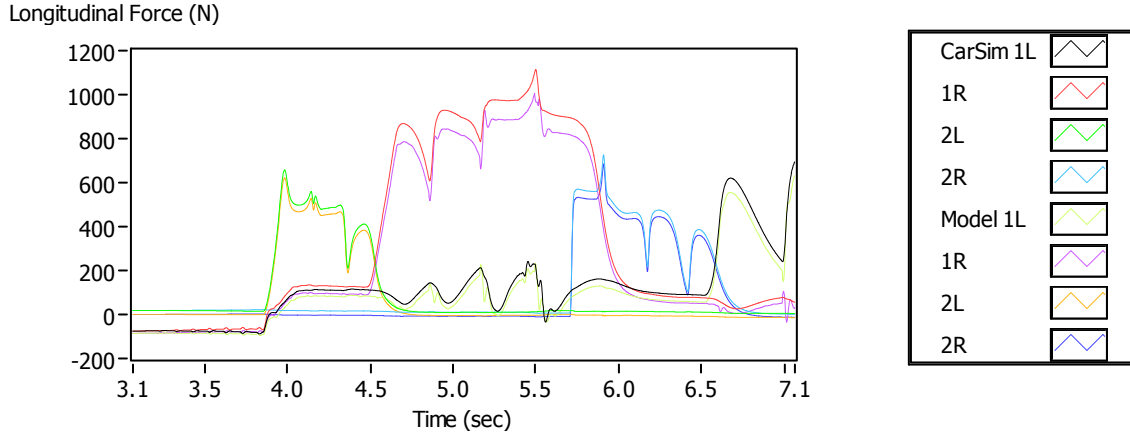
Figure 4.6: Brake Force Estimation with Wheel and Drivetrain Dynamics

Once the longitudinal braking forces for each wheel have been estimated, their contribution to the lateral force and yaw moment equations may be included. The contribution of longitudinal braking force to vehicle yaw moment may be defined:

$$M_{z,c} = \frac{t}{2} \left[\left(F_{x1L} - F_{x1R} \right) \cos \delta + F_{x2L} - F_{x2R} \right] \tag{4.9}$$

Note that the front axle lateral force terms are neglected in the moment contribution of longitudinal force since they are multiplied by the sine of the steer angle, and since they cancel moments when the left and right lateral forces are equal. The complete force and moment equations are then:

$$
\begin{bmatrix} a_y \\ \dot{r} \end{bmatrix} = \begin{bmatrix} \dfrac{1}{m} & \dfrac{1}{m} \\[2ex] \dfrac{a}{J} & -\dfrac{b}{J} \end{bmatrix} \begin{bmatrix} F_{y1}\cos\delta \\[1ex] F_{y2} \end{bmatrix} - \begin{bmatrix} \dfrac{1}{m} \\[2ex] \dfrac{a}{J} \end{bmatrix} F_{x1}\sin\delta + \begin{bmatrix} 0 \\[1ex] \dfrac{1}{J} \end{bmatrix} M_{z,c}
\qquad (4.10)
$$

The mass matrix may be inverted to allow direct calculation of the axle lateral forces.

$$
\begin{bmatrix} F_{y1} \\ F_{y2} \end{bmatrix} = \begin{bmatrix} \dfrac{mb}{\cos\delta(a+b)} & \dfrac{J}{\cos\delta(a+b)} \\[3ex] \dfrac{ma}{a+b} & -\dfrac{J}{a+b} \end{bmatrix} \begin{bmatrix} a_y + \dfrac{F_{x1}}{m}\sin\delta \\[3ex] \dot{r} + \dfrac{aF_{x1}}{J}\sin\delta - \dfrac{M_{z,c}}{J} \end{bmatrix}
\qquad (4.11)
$$

Note that here the cosine and sine functions of the road steer angle are used, however these could be replaced with linear approximations to reduce the computational burden of the controller.

4.2 Estimation of Lateral Force Potential

Due to longitudinal forces, the actual lateral force generated by the tires will be less than theoretically possible at the given slip angle when no longitudinal force is present. This must be accounted for if the lateral force characteristics of the tire are to be estimated. Otherwise the ESC control scheme will produce positive feedback: ESC braking will result in reduced lateral force and hence further axle saturation if this effect is not compensated.

The normal loads on each tire may be estimated by ignoring suspension roll and tire deflection dynamics and solving the static lateral load transfer for the measured lateral acceleration. Note that future work could incorporate a model of roll dynamics for a better estimation of normal loads. The longitudinal force is estimated from the wheel

braking dynamics described above. However, only the per-axle lateral forces are known from the estimation from force and moment balance equations. The per wheel lateral force must be determined in order to use the friction ellipse model to estimate lateral force potential – that is the lateral force generation possible at the given slip angle without longitudinal force.

As an approximation of the interaction of the wheel longitudinal and lateral forces, the "friction ellipse" may be used [14]:

$$\left(\frac{F_y}{F_y^*}\right)^2 + \left(\frac{F_x}{F_x^*}\right)^2 = 1 \tag{4.12}$$

The concept of the friction ellipse is also shown graphically in Figure 4.7. F_y^* is the lateral force potential of the wheel at the given state, and represents the lateral force that the wheel would generate at the current slip angle if the wheel did not have any longitudinal slip. Conversely F_x^* is the longitudinal force potential and represents the longitudinal force that would be generated with the current wheel slip if the slip angle was zero. The longitudinal force potential is the peak longitudinal force and is equal to the coefficient of friction multiplied by the tire normal force. For any state of combined longitudinal force F_x and lateral force F_y, the approximate relationship of equation (4.12) is assumed to hold. Therefore the resultant force vector must lie on the ellipse as shown in Figure 4.7. Note that typically the maximum possible lateral force potential is $F_{y,max}^* = \mu F_z$, the same as that of the longitudinal force potential. In this case the shape of the ellipse is circular, resulting in the commonly-known "friction circle" or "traction circle."
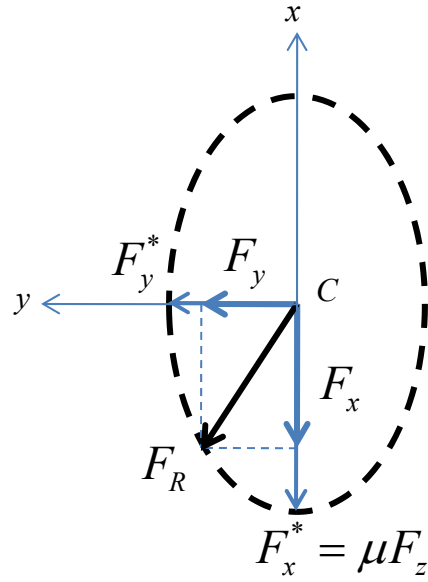
Figure 4.7: Tire Friction Ellipse for Constant Slip Angle

For each wheel, the friction ellipse is then:

$$\left(\frac{F_{yL}}{F_{yL}^*}\right)^2 + \left(\frac{F_{xL}}{\mu F_{zL}}\right)^2 = 1$$

$$\left(\frac{F_{yR}}{F_{yR}^*}\right)^2 + \left(\frac{F_{xR}}{\mu F_{zR}}\right)^2 = 1$$

(4.13)

Here $F_{yL,R}^*$ is the theoretical lateral force potential of the specific wheel. In addition to wheel longitudinal forces, the individual wheel normal forces are also estimated. The estimate is based on a steady state lateral load transfer due to lateral acceleration of the vehicle CG. The actual normal forces will vary during transient roll response to lateral forces, however the static approximation was found to be sufficient for use in the ESC algorithm in simulation testing.

If there were no longitudinal forces present, then the wheel lateral forces could be estimated from the axle lateral force:

$$F_{yL}^* = \frac{F_{zL}}{F_z} F_y^*$$

$$F_{yR}^* = \frac{F_{zR}}{F_z} F_y^*$$

(4.14)

Therefore:

$$\left(\frac{F_{yL}}{\frac{F_{zL}}{F_z} F_y^*} \right)^2 + \left(\frac{F_{xL}}{\mu F_{zL}} \right)^2 = 1$$

$$\left(\frac{F_{yR}}{\frac{F_{zR}}{F_z} F_y^*} \right)^2 + \left(\frac{F_{xR}}{\mu F_{zR}} \right)^2 = 1$$

(4.15)

Or rearranged:

$$F_{yL} = F_y^* \frac{F_{zL}}{F_z} \sqrt{1 - \left(\frac{F_{xL}}{\mu F_{zL}} \right)^2}$$

$$F_{yR} = F_y^* \frac{F_{zR}}{F_z} \sqrt{1 - \left(\frac{F_{xR}}{\mu F_{zR}} \right)^2}$$

(4.16)

Finally the actual lateral force generated by each wheel must sum to the estimated axle lateral force.

$$F_y = F_{yL} + F_{yR}$$

$$F_y = F_y^* \frac{F_{zL}}{F_z} \sqrt{1 - \left(\frac{F_{xL}}{\mu F_{zL}}\right)^2} + F_y^* \frac{F_{zR}}{F_z} \sqrt{1 - \left(\frac{F_{xR}}{\mu F_{zR}}\right)^2}$$

$$F_y = \frac{F_y^*}{F_z} \left[F_{zL} \sqrt{1 - \left(\frac{F_{xL}}{\mu F_{zL}}\right)^2} + F_{zR} \sqrt{1 - \left(\frac{F_{xR}}{\mu F_{zR}}\right)^2} \right] \qquad (4.17)$$

$$F_y^* = \left[F_{zL} \sqrt{1 - \left(\frac{F_{xL}}{\mu F_{zL}}\right)^2} + F_{zR} \sqrt{1 - \left(\frac{F_{xR}}{\mu F_{zR}}\right)^2} \right]^{-1} F_z F_y$$

Note that the friction ellipse approximation is valid only when the longitudinal slip is below that of the peak F_x. Beyond this point the longitudinal force is saturated and the friction ellipse fails because the F_x begins to decrease before F_y goes to zero. This causes a problem with the algorithm above because the actual F_x on the curve could lead to two possible F_y values, the one corresponding to the ellipse (longitudinal slip not saturated) and one corresponding to a greatly reduced F_y (longitudinal slip saturated). To avoid this problem, the ABS controller must ensure that the longitudinal slip stays below the peak value. This is done in this application be scaling the slip ratio targets for ABS activation by the estimated friction coefficient μ. Thus on a low friction surface the slip ratio is maintained at a lower range to prevent saturation.

Note also that the coefficient of friction estimated for the front axle is used as the estimate for both axles. This is because if only one axle has saturated, the coefficient of friction of the other axle is unknown until it is saturated. In general, the front axle saturates before the rear axle does, therefore this value may be assumed to apply to both. Even if a transition is made from a high friction surface to a low friction surface at 60

kph, the time between axles is only 167 milliseconds. Therefore it is not practical to try

to maintain separate estimates of friction coefficient for each axle.
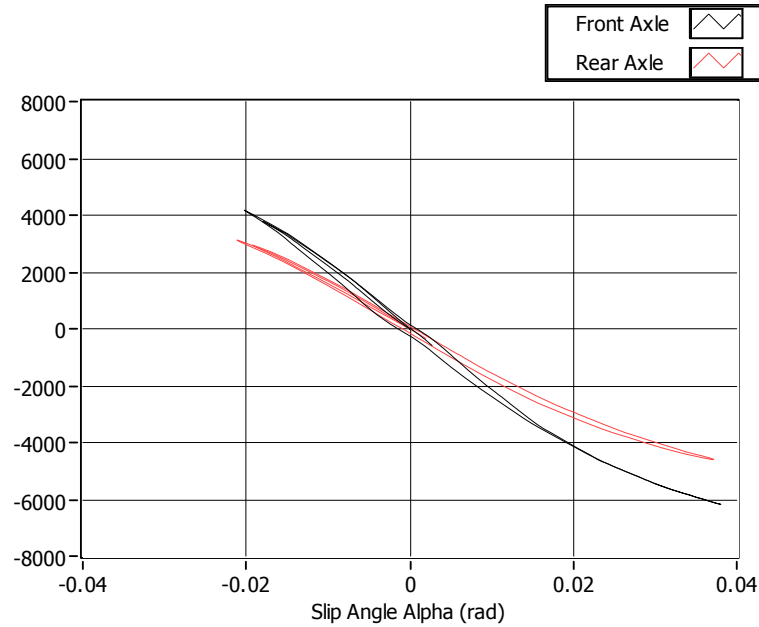
Figure 4.8: Real-Time Lateral Force Estimation in High Speed Double Lane Change

With estimates of axle slip angle and lateral force, the per-axle lateral force

characteristic curve may be generated in real-time while driving. An example of a trace

of lateral force and slip angle during a high speed double lane change maneuver is shown

in Figure 4.8.

4.3 Axle Saturation and Friction Estimation

Axle saturation is determined by comparing the estimated lateral force to a

theoretical force calculated as the slip angle multiplied by the axle linear cornering

stiffness coefficient. Note that while this determination does depend on a known axle

cornering stiffness value, this parameter is estimated in real-time from the lateral force response at low slip angle as described below.
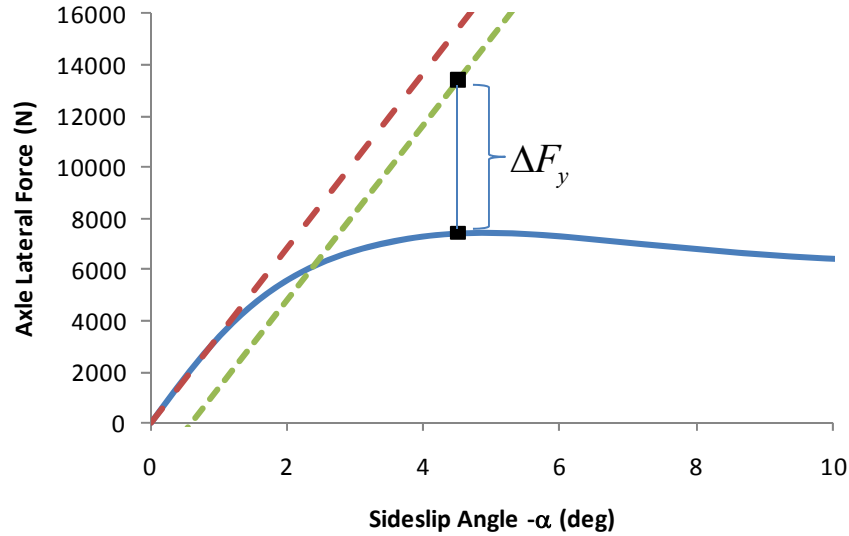
Figure 4.9: Axle Lateral Force Saturation Detection

Figure 4.9 shows the approach for detection of axle lateral force saturation from the estimated lateral force characteristics. The solid line represents the time history of estimated axle lateral force and slip angle, with the current estimate at slip angle of -4.5 deg., as indicated with a square. The theoretical axle lateral force assuming linear cornering stiffness is shown with the large dashed line. A dead zone of 2000 N below the linear lateral force is used in the detection algorithm to avoid false detection due to estimation errors and to account for the nonlinearity of the characteristic curve at slip angles below the angle corresponding to peak lateral force. If the estimated lateral force is lower than linear dead zone region, the axle is deemed to be saturated. The difference

between the theoretical lateral force and the estimated lateral force is subsequently used by the equivalent moment generation algorithm of the ESC controller described below.

The axle lateral force saturation detection can be used directly to calculate an estimate of road/tire coefficient of friction. In general, the peak lateral force will be equal to the axle normal load multiplied by the coefficient of friction. The assumption of the estimation is that if saturation of the axle lateral force is detected, the estimated lateral force must be at or very near the peak lateral force capability of the tires on that axle. This is evident for values of lateral force below the saturation limit shown in Figure 4.9. The coefficient of friction may then be directly estimated:

$$\hat{\mu} = \frac{|F_y|}{F_z}, \quad \text{if } |F_y| < |F_{y,sat}| = |-C\alpha| - F_{y,deadzone} \tag{4.18}$$

An example of estimated coefficient of friction on a simulated road surface with mu of 0.2 is shown in Figure 4.10. The rear axle did not saturate during this maneuver, therefore the estimated coefficient of friction remains at the initial assumed value. This motivates the need to use the front axle value as the assumed friction coefficient for both axles as simulation results show that the front axle generally saturates before the rear axle. The variations in estimated coefficient of friction in the front axle occur as the axle lateral force changes during saturation. Periods of constant estimated coefficient of friction occur because estimation is suspended when the axle lateral force is not saturated.
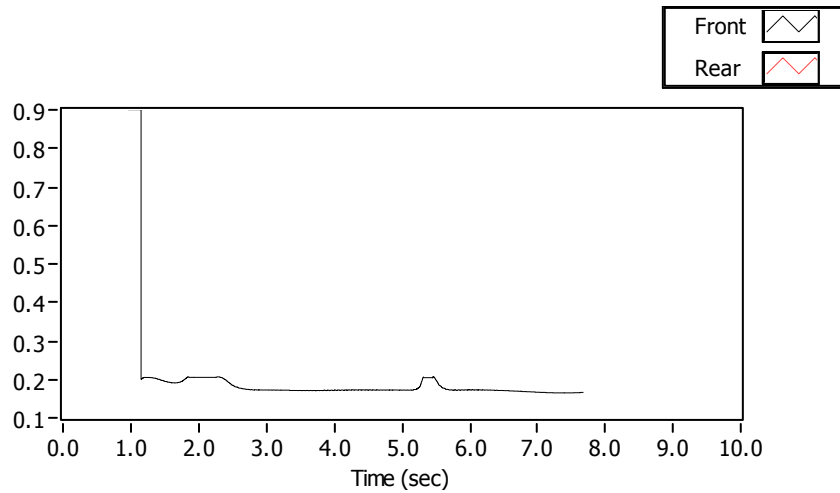
Figure 4.10: Estimated Coefficient of Friction on Low Friction Surface

Chapter Summary

In this chapter a method of estimating lateral force potential was presented and subsequently used in the determination of axle lateral force saturation and estimation of road/tire coefficient of friction. Basic axle lateral force was estimated by inverting the lateral force and yaw moment balance equations. Tire normal force was estimated from a steady state lateral load transfer model and longitudinal forces were estimated from measured wheel speeds and wheel spin moment balance equations. The friction ellipse approximation was used to combine these forces to obtain an estimate of axle lateral force potential in the absence of longitudinal forces.

From the real time estimation of axle lateral force response, axle lateral force saturation was detected by comparison to a linear lateral force response to slip angle. The estimated wheel normal loads provide an opportunity to estimate coefficient of friction when saturation is detected. Under normal driving conditions the lateral force response

63

characteristics will be used to identify vehicle parameters. When lateral force saturation

is detected, the ESC control strategy will be used to provide additional yaw moment to

restore vehicle stability.

CHAPTER FIVE

REAL-TIME VEHICLE PARAMETER IDENTIFICATION

When an axle of the vehicle is not saturated in lateral force capability, the estimated lateral force and slip angle provide an opportunity to identify critical vehicle parameters in real-time. This capability enables the ESC strategy to adapt to identified changes in these vehicle parameters. The role of vehicle parameter identification in the ESC strategy is shown in Figure 1.1 and in greater detail in Figure 5.1.
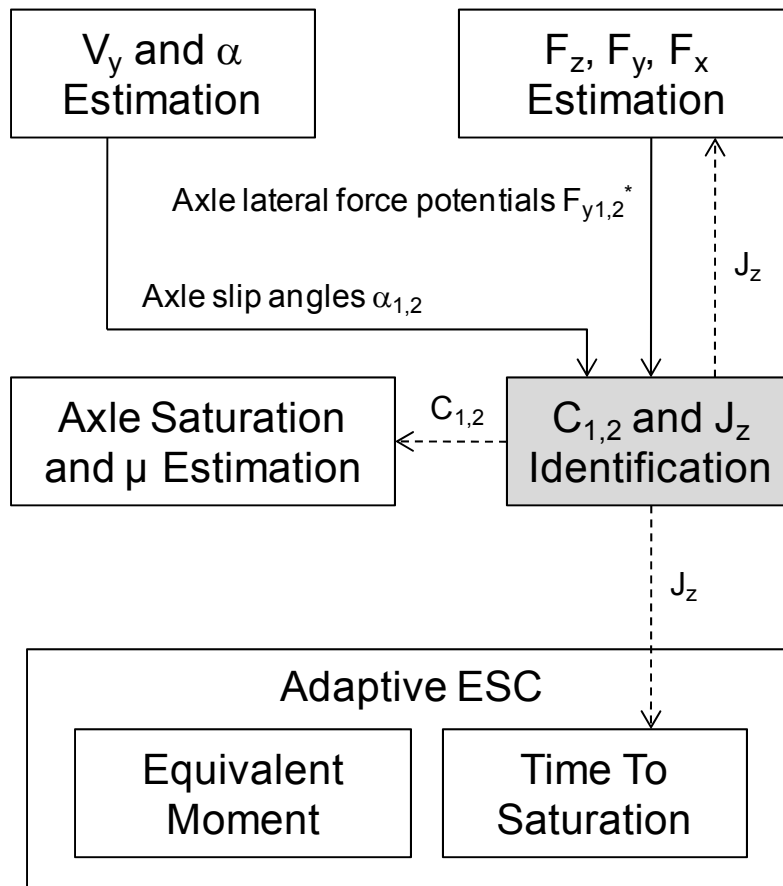
Figure 5.1: Role of Vehicle Parameter Identification in ESC Strategy

The estimated axle slip angles described in Chapter Three and the estimated axle lateral force potentials described in Chapter Four are used to identify vehicle parameters when the slip angles are relatively small. Identified axle cornering stiffness coefficients may be used in the detection of axle lateral force saturation as described in 4.3 Axle Saturation and Friction Estimation. The identified yaw moment of inertia J_z may be used in the estimation of axle lateral forces described in Chapter Four and in the predictive ESC strategy described in 6.2 Time To Saturation (TTS) Predictive ESC Control.

A recursive least squares with exponential forgetting factor algorithm is used to identify the linear cornering stiffness coefficient for each axle in real-time. Since only vehicle motion is measured and not forces, it is not possible to estimate vehicle mass directly. However when the axle cornering stiffnesses are identified, a change in vehicle mass will appear as a corresponding change in cornering stiffness. In this manner the ESC algorithm is capable of adapting to changes in both tire properties and vehicle mass.

In addition to estimating lateral cornering stiffnesses, yaw moment of inertia may be identified by using recursive least squares estimation on the system of lateral force equations. This approach is very advantageous since mass and center of gravity longitudinal location may be measured directly using scales under the axles or on-vehicle load pressure sensors at the axles. However, yaw moment of inertia is a very difficult quantity to measure. Total vehicle mass may also be determined from longitudinal driving dynamics, thus obviating the need for load sensors at each axle. Therefore, it is desirable to also estimate center of gravity longitudinal location. However, testing results show that the recursive least squares estimation is not capable of separating the effects of

relative front/rear distribution of cornering stiffness and center of gravity longitudinal location.

5.1 Axle Cornering Stiffness Identification

The cornering stiffness of the tires on an axle may change over time due to wear, road condition or other factors. In addition replacement tires may be of a different make and/or model than the original tires and may have different handling properties. For these reasons the cornering stiffness is estimated directly from the estimated lateral force characteristics when the lateral force is not saturated. The simple linear model for axle lateral force generation serves as the model for identification.

$$F_{y1} = -C_1 \alpha_1$$
$$F_{y2} = -C_2 \alpha_2$$

(5.1)

A Recursive Least Squares (RLS) with exponential forgetting factor algorithm is used for estimation of cornering stiffness for each axle [50]. This approach is the same as that proposed by Deng and Haicen, except that here the front and rear cornering stiffness equations have been decoupled since front and rear lateral forces and slip angles have already been estimated [23]. As a result simple RLS estimates can be computed for each axle cornering stiffness at each sample n:

$$k_n = \frac{P_{n-1} \hat{\alpha}_n}{\lambda + P_{n-1} \hat{\alpha}_n^2}$$
$$\hat{C}_n = \hat{C}_{n-1} + k_n \left(\hat{F}_{y,n} - \hat{C}_{n-1} \hat{\alpha}_n \right)$$
$$P_n = \frac{P_{n-1}}{\lambda} \left(1 - k_n \hat{\alpha}_n \right)$$

(5.2)

Seeding P_0 with an initial large value of 1000 ensures fast convergence of the cornering stiffness estimates. The forgetting factor λ is given a value of 0.9999. Since the ESC controller has a time step of 1 millisecond, a step change in cornering stiffness will result in a 50% change in the estimated value in ~7 seconds. Both front and rear axle cornering stiffnesses are initialized with a value of 200,000 N/rad. The actual cornering stiffness of the front axle is much higher than that of the rear axle due to the weight bias towards the front of the test vehicle. Note that the estimation is suspended for an axle when the side slip angle exceeds 1 degree in magnitude. Above this range nonlinearities are evident in the lateral force characterstic curve due to secondary effects.
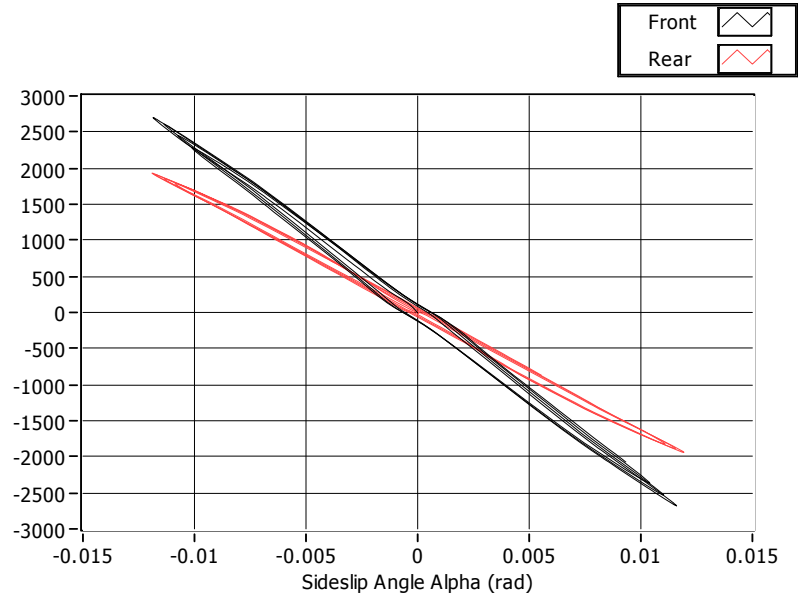
Figure 5.2: Estimated Lateral Force Characteristic Response of Nominal Vehicle

A test of the cornering stiffness estimation was conducted with a swept sinusoidal steering input with handwheel angle amplitude of 17 deg (approximately 1 deg road-

wheel angle) and with frequency increasing from 0.2 Hz to 0.6 Hz at 100 kph. The results for the nominal test vehicle are shown in Figure 5.2 and Figure 5.3.

Although both axles were initialized with the same cornering stiffness, the estimation algorithm quickly converged on a higher cornering stiffness for the front axle. For reference the theoretical combined cornering stiffness values of the loaded tires on each axle are also provided on the plot. As can be seen in Figure 5.3, the actual cornering stiffnesses are lower than the theoretical values due to other effects such as roll steer and compliance steer. The final estimate values agree with a manual linear least squares fits of the lateral force characteristic data output from CarSim.
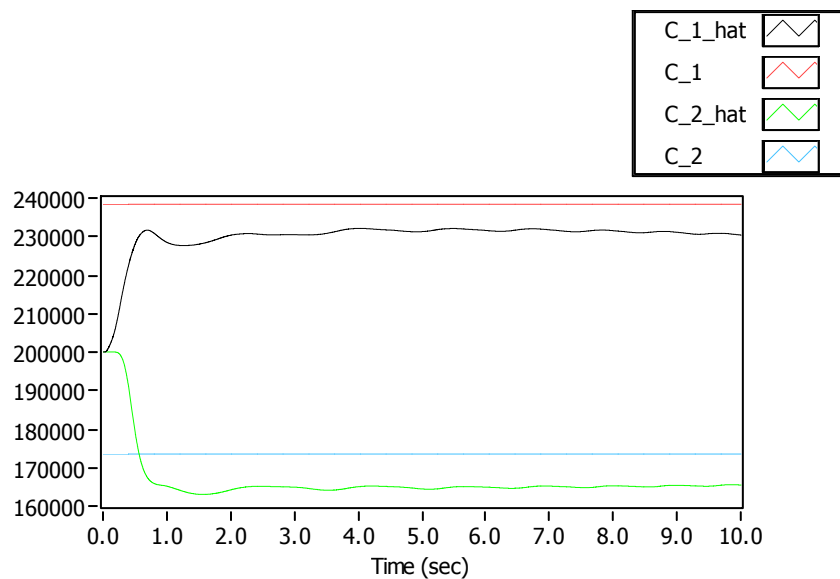
Figure 5.3: Axle Cornering Stiffness Estimation of Nominal Vehicle

For comparison a second test vehicle model was configured with rear tires with 80% of the lateral force capability of the front tires, resulting in an oversteering vehicle.

Again the cornering stiffness estimation algorithm was initialized with cornering stiffness values of 200,000 N/rad.

The lateral force characteristics estimation and cornering stiffness estimation are shown in Figure 5.4 and Figure 5.5.
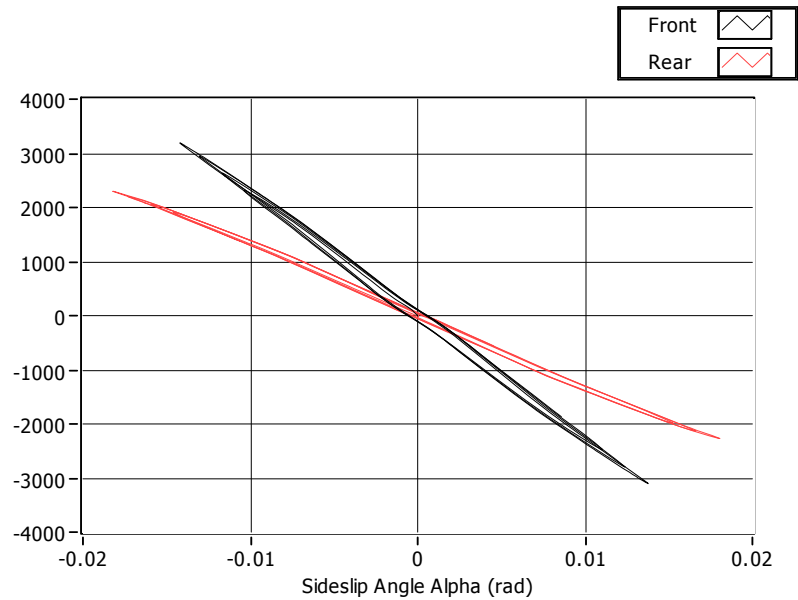
Figure 5.4: Estimated Lateral Force Characteristic Response of Oversteering Vehicle

The estimated cornering stiffness of the rear axle for the nominal vehicle (Figure 5.3) is 166,000 N/rad. The estimated rear axle cornering stiffness for the second test vehicle (Figure 5.5) is 130,000 N/rad, or 78% of that of the nominal vehicle. Again the theoretical values of axle cornering stiffness of the nominal vehicle are also shown on the plot for reference.
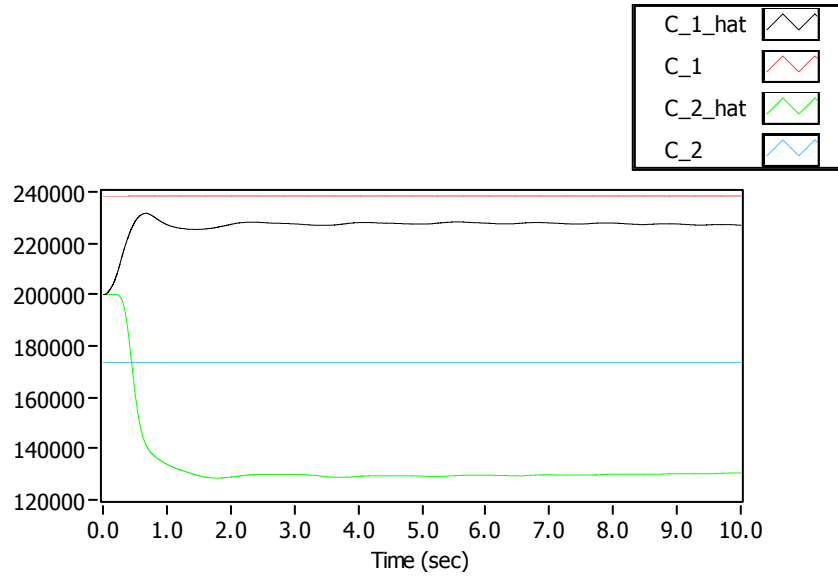
Figure 5.5: Axle Cornering Stiffness Estimation of Oversteering Vehicle

It should be noted that such RLS estimations require input signals that are persistently exciting. If the estimated forces and slip angles remain small for extended periods of time, significant estimation errors may develop. When such a condition is encountered or signal quality is deemed to be poor, the forgetting factor may be adjusted closer to 1 such that the previous estimation value is retained [23]. The simple examples here provide sufficient signal excitation, therefore such a correction is not employed. However, this would need to be considered for any practical application of the method.

5.2 Indirect Vehicle Mass Identification

Although forces are not measured and therefore vehicle mass cannot be identified directly, a change in vehicle mass will manifest itself as an apparent change in cornering stiffness to the control system. Note that if the yaw moment of inertia of the vehicle is

assumed to have a constant radius of gyration, then the inertia will scale linearly with total vehicle mass.

$$J = mR_z{}^2 \tag{5.3}$$

In this case the lateral force and moment equations (4.11) may be rewritten:

$$
\begin{bmatrix} \dfrac{F_{y1}}{m} \\[2mm] \dfrac{F_{y2}}{m} \end{bmatrix} =
\begin{bmatrix} \dfrac{b}{\cos\delta(a+b)} & \dfrac{R_z{}^2}{\cos\delta(a+b)} \\[4mm] \dfrac{a}{a+b} & -\dfrac{R_z{}^2}{a+b} \end{bmatrix}
\begin{bmatrix} a_y + \dfrac{F_{x1}}{m}\sin\delta \\[4mm] \dot{r} + \dfrac{aF_{x1}}{J}\sin\delta - \dfrac{M_{z,c}}{J} \end{bmatrix} \tag{5.4}
$$

In the case where the axle is not in saturation, the linear lateral force model is assumed to hold.

$$
\begin{bmatrix} -\dfrac{C_1}{m}\alpha_1 \\[2mm] -\dfrac{C_2}{m}\alpha_2 \end{bmatrix} =
\begin{bmatrix} \dfrac{b}{\cos\delta(a+b)} & \dfrac{R_z{}^2}{\cos\delta(a+b)} \\[4mm] \dfrac{a}{a+b} & -\dfrac{R_z{}^2}{a+b} \end{bmatrix}
\begin{bmatrix} a_y + \dfrac{F_{x1}}{m}\sin\delta \\[4mm] \dot{r} + \dfrac{aF_{x1}}{J}\sin\delta - \dfrac{M_{z,c}}{J} \end{bmatrix} \tag{5.5}
$$

It is clear from this formulation of the equations that the identification process is actually identifying cornering force per unit mass. For example a doubling of vehicle mass (assuming all other vehicle parameters unchanged) should result in an identified cornering stiffness of one half of the original value. In actuality, a number of vehicle parameters change with vehicle mass. For example compression of the tires leads to kinematic and compliance effects in both wheel toe and camber. More importantly, tire cornering stiffness itself generally increases with increasing normal load. The tire cornering stiffness as a function of normal load for the tires used for simulation studies in this work are shown in Figure 5.6.
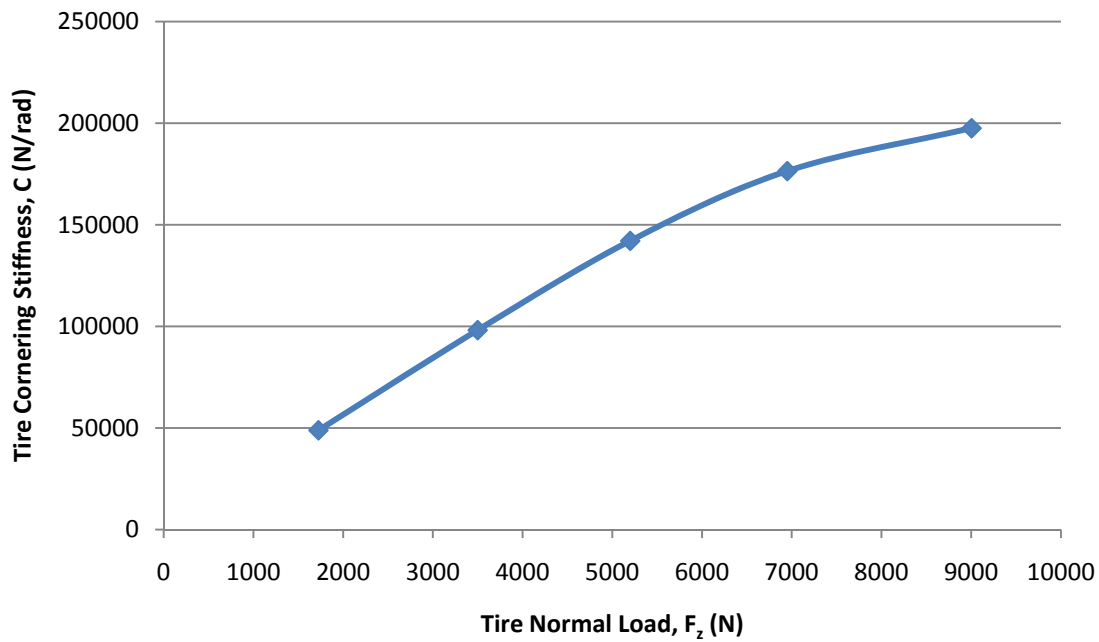
Figure 5.6: Simulated 215/75 R17 Tire Cornering Stiffness as a Function of Normal Load

For the vehicle model used in simulations, the nominal front tire load is 4425 N and the nominal rear tire load is 3079 N. For tire loads below these nominal values, it is clear from Figure 5.6 that the cornering stiffness scales linearly with vehicle load.

Therefore if the cornering stiffness identification is carried out assuming the nominal vehicle mass, there will be only a slight change in identified cornering stiffness when the actual vehicle mass is decreased. The decreased mass results in decreased tire cornering stiffness and the vehicle handling behavior changes only slightly due to secondary suspension effects. However increasing the vehicle load will put some or all tires in the nonlinear part of the curve observed in Figure 5.6. In this case the percentage increase in cornering stiffness will be less than the corresponding percentage increase in

vehicle mass. As a result, the identification algorithm which assumes nominal vehicle mass should converge to lower than normal values of cornering stiffness.

A simulation was conducted with an increased vehicle mass of 50% in both the sprung and unsprung masses. The moments of inertia where also increased 50% assuming a constant radius of gyration (i.e. a consistent distribution of mass throughout the vehicle bodies). Due to the increase in mass the wheel loads increased by 50% and the tire cornering stiffnesses increased according to the relationship in Figure 5.6. The increases mass and corresponding increase in axle cornering stiffness may also be seen in Table 5.1. As a result of the nonlinear relationship for cornering stiffness, the cornering stiffness normalized by vehicle mass actually decreased by 7% in the front axle and by 2% in the rear.

Table 5.1: Theoretical Axle Cornering Stiffness from Tire Model

	Vehicle mass, m (kg)	Tire normal load, F_z (N)		Axle Cornering Stiffness, C (N/rad)		C/m (N/(rad*kg))	
		Front	Rear	Front	Rear	Front	Rear
Nominal	1530	4425	3079	244,100	172,900	159.5	113.0
Loaded	2295	6638	4619	340,600	254,100	148.4	110.7
%	150%	150%	150%	140%	147%	93%	98%

The simulation of the sine sweep input was conducted again with the heavy vehicle. As can be observed in Figure 5.7 the cornering stiffnesses identified are lower than those of the nominal vehicle seen in Figure 5.3.
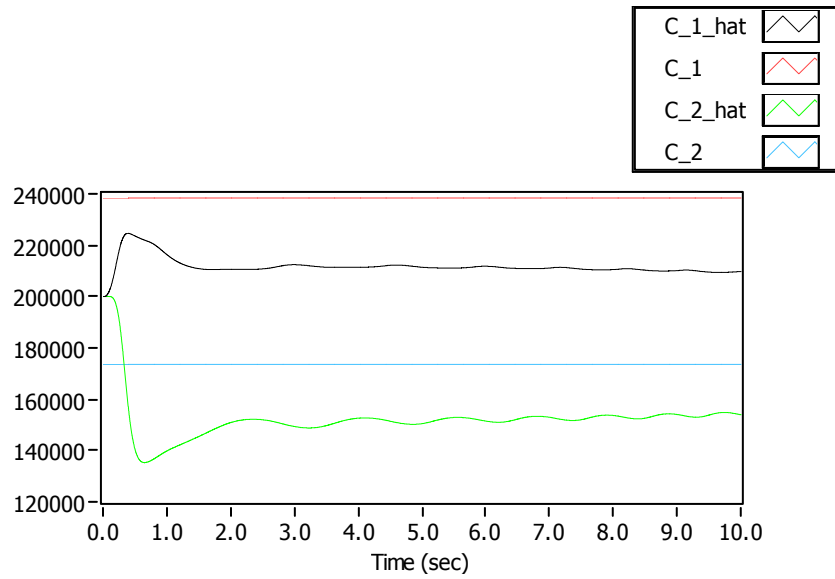
Figure 5.7: Axle Cornering Stiffness Estimation of 150% Mass Vehicle

Table 5.2 shows that the identified cornering stiffness of the front axle decreased by 9% while the rear axle decreased by 8%. As expected the magnitude of the decrease is close to the decrease of the theoretical normalized cornering stiffnesses in table. These results do not match exactly as the cornering stiffness is not the only parameter that changes with increasing vehicle mass; compression of the suspension leads to additional changes in the kinematics and compliance effects on the wheels.

Table 5.2: Identified Axle Cornering Stiffness from Simulation

	Axle Cornering Stiffness, C (N/rad)	
	Front	Rear
Nominal	231,000	166,000
Loaded	209,000	152,000
%	90.5%	91.6%

The results of the estimation in Figure 5.7 do show however that the parameter identification does identify the net change in normalized axle cornering stiffness. As a result the ESC control system is therefore able to adapt to the change in vehicle mass via the change in axle cornering stiffness.

5.3 Vehicle Yaw Moment of Inertia Identification

Equation (5.1) enabled separate recursive least squares estimations of the cornering stiffnesses of each axle. Each estimation used one lateral force equation with a single regression variable α_i and a single observed variable F_{yi}. This resulted in the simple recursive least squares estimation of equation (5.2). By rearranging equation (4.11), a system of equations may be realized for recursive least squares estimation of both axle cornering stiffnesses and vehicle yaw moment of inertia.

$$
\begin{bmatrix} -C_1\alpha_1 \\ -C_2\alpha_2 \end{bmatrix} = \begin{bmatrix} \dfrac{mb}{\cos\delta(a+b)} & \dfrac{J}{\cos\delta(a+b)} \\ \dfrac{ma}{a+b} & -\dfrac{J}{a+b} \end{bmatrix} \begin{bmatrix} a_y \\ \dot{r} \end{bmatrix} + \begin{bmatrix} F_{x1}\tan\delta - \dfrac{M_{z,c}}{\cos\delta(a+b)} \\ \dfrac{M_{z,c}}{a+b} \end{bmatrix}
$$

$$
\begin{bmatrix} -\alpha_1 & 0 & -\dfrac{\dot{r}}{\cos\delta(a+b)} \\ 0 & -\alpha_2 & \dfrac{\dot{r}}{a+b} \end{bmatrix} \begin{bmatrix} C_1 \\ C_2 \\ J \end{bmatrix} = \begin{bmatrix} \dfrac{mba_y}{\cos\delta(a+b)} + F_{x1}\tan\delta - \dfrac{M_{z,c}}{\cos\delta(a+b)} \\ \dfrac{maa_y}{a+b} + \dfrac{M_{z,c}}{a+b} \end{bmatrix}
$$

(5.6)

The vector of cornering stiffness values and yaw moment of inertia are the parameters to be identified. For recursive least squares, the variables of the matrix premultiplied by the parameter vector are the regressors and the variables of the vector on the right-hand side are the outputs.

$$\boldsymbol{\Phi}_n{}^T\boldsymbol{\theta} = \mathbf{y}_n$$

$$\boldsymbol{\Phi}_n = \begin{bmatrix} -\alpha_1 & 0 \\ 0 & -\alpha_2 \\ -\dfrac{\dot{r}}{\cos\delta(a+b)} & \dfrac{\dot{r}}{a+b} \end{bmatrix}$$

$$\boldsymbol{\theta} = \begin{bmatrix} C_1 \\ C_2 \\ J \end{bmatrix}$$

$$\mathbf{y}_n = \begin{bmatrix} \dfrac{mba_y}{\cos\delta(a+b)} + F_{x1}\tan\delta - \dfrac{M_{z,c}}{\cos\delta(a+b)} \\ \dfrac{maa_y}{a+b} + \dfrac{M_{z,c}}{a+b} \end{bmatrix}$$

(5.7)

The recursive least squares with exponential forgetting algorithm may then be applied to the system of equations [50]:

$$\mathbf{K}_n = \mathbf{P}_{n-1}\boldsymbol{\Phi}_n\left(\lambda\mathbf{I} + \boldsymbol{\Phi}_n{}^T\mathbf{P}_{n-1}\boldsymbol{\Phi}_n\right)^{-1}$$

$$\hat{\boldsymbol{\theta}}_n = \hat{\boldsymbol{\theta}}_{n-1} + \mathbf{K}_n\left(\mathbf{y}_n - \boldsymbol{\Phi}_n{}^T\hat{\boldsymbol{\theta}}_{n-1}\right)$$

$$\mathbf{P}_n = \frac{1}{\lambda}\left(\mathbf{P}_{n-1} - \mathbf{K}_n\boldsymbol{\Phi}_n{}^T\mathbf{P}_{n-1}\right)$$

(5.8)

The results of estimation for the sine sweep steer input simulation are shown in Figure 5.8. The final value of identified yaw inertia is 4820 kg*m^2, where theoretical model value is 4606 kg*m^2. The difference may be related to the vehicle roll and other compliances that make the vehicle appear slow in response to yaw moment input. Simulation of a vehicle with very high roll stiffness and minimal compliances results in an identified yaw moment of inertia very close to the theoretical value. These effects may also explain the slightly lower estimated cornering stiffness values as well.
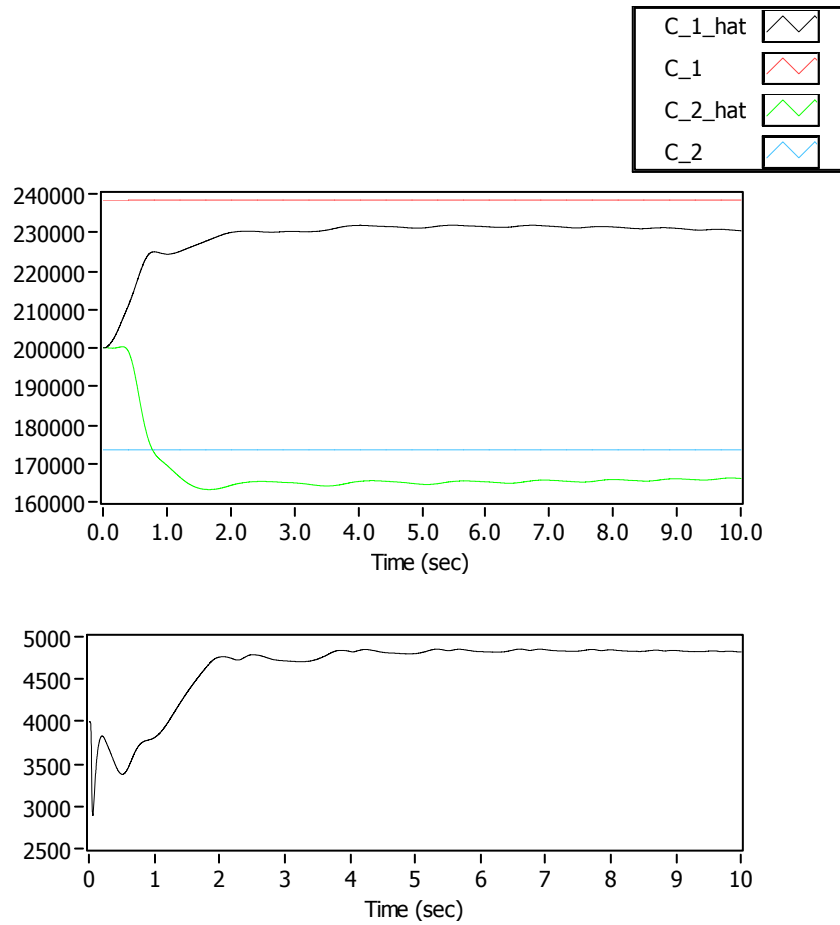
Figure 5.8: RLS Estimation of Axle Cornering Stiffnesses and Yaw Moment of Inertia

In order to further test the yaw moment of inertia identification, the algorithm was tested with a vehicle loaded at Gross Vehicle Weight Rating. As described in section 7.3 ESC System Robustness Test Results, this vehicle has 450 kg added to the trunk which significantly changes the vehicle parameters. Note that for the axle cornering stiffness and yaw moment of inertia estimation to succeed, the total vehicle mass and center of gravity longitudinal location must be known. Therefore the assumption is made that

these changes may be detected by sensors such as load sensors in the axle suspensions, and therefore these parameters are used in the RLS estimation algorithm.
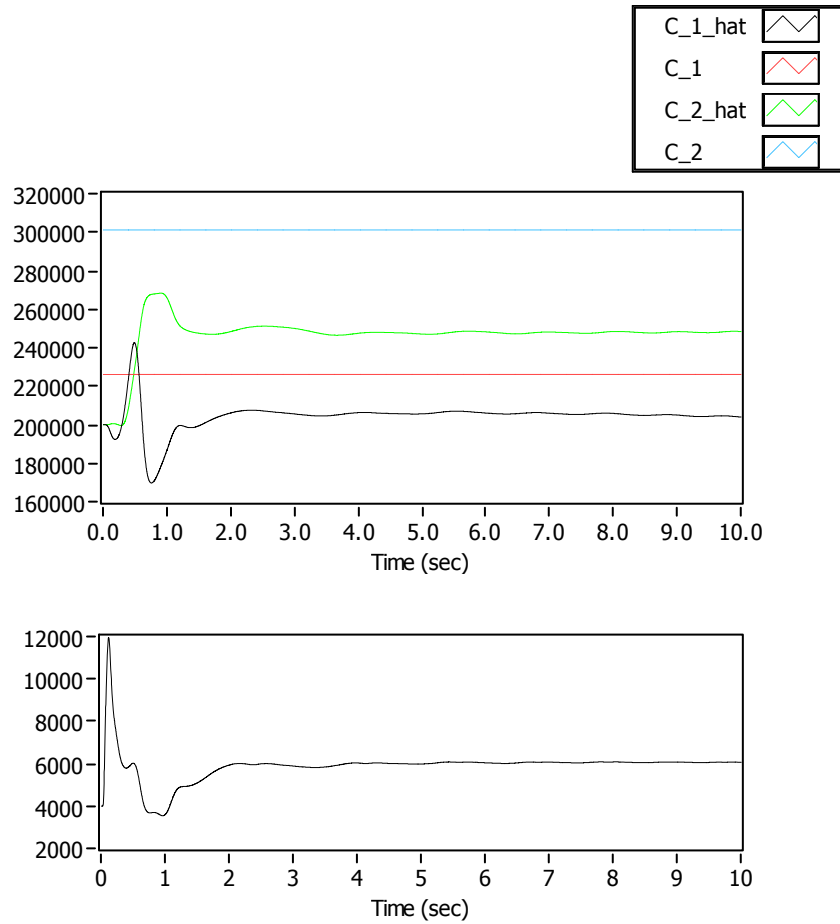
Figure 5.9: RLS Estimation of Axle Cornering Stiffnesses and Yaw Moment of Inertia for Loaded Vehicle

The results of the sine sweep test for the loaded vehicle are shown in Figure 5.9. As expected, the rear axle cornering stiffness is significantly higher than that of the front axle due to the change in front/rear vehicle weight distribution with the added load. The

changes in nominal axle cornering stiffnesses and yaw moment of inertia due to the additional loading can be seen in Table 7.10.

The identified cornering stiffnesses are again lower than the nominal computed cornering stiffnesses in the loaded condition, which are also shown in Figure 5.9. This is especially true for the rear axle, which in the heavily loaded condition would be expected to have even more secondary effects on cornering stiffness due to kinematic and compliance effects of the suspension as well as lateral load transfer. The final value of identified yaw moment of inertia is 6,060 kg*m^2, which is in very close agreement with the theoretical value of 6,122 kg*m^2.

5.4 Vehicle Center of Gravity Longitudinal Location Identification

If total vehicle mass is estimated from longitudinal driving dynamics, then sensors are not needed at each axle to measure normal loads. However, information on center of gravity longitudinal location is not known without these sensors. Therefore it is desirable to estimate this location directly from the vehicle handling. If a constant radius of gyration for yaw moment of inertia is assumed, then this parameter may be estimated from the identified vehicle mass. The problem then is to estimate axle cornering stiffnesses and center of gravity longitudinal location. As in section 5.3 Vehicle Yaw Moment of Inertia Identification, the lateral force equations may be rearranged in a form suitable for recursive least squares estimation. Note that the wheelbase $l = a + b$ is substituted in the equations such that the only parameter to be identified is the distance from the front axle to the center of gravity, a.

$$\begin{bmatrix} -C_1\alpha_1 \\ -C_2\alpha_2 \end{bmatrix} = \begin{bmatrix} \dfrac{m(l-a)}{l\cos\delta} & \dfrac{J}{l\cos\delta} \\ \dfrac{ma}{l} & -\dfrac{J}{l} \end{bmatrix} \begin{bmatrix} a_y \\ \dot{r} \end{bmatrix} + \begin{bmatrix} F_{x1}\tan\delta - \dfrac{M_{z,c}}{\cos\delta l} \\ \dfrac{M_{z,c}}{l} \end{bmatrix}$$

$$\begin{bmatrix} -\alpha_1 & 0 & \dfrac{ma_y}{l\cos\delta} \\ 0 & -\alpha_2 & -\dfrac{ma_y}{l} \end{bmatrix} \begin{bmatrix} C_1 \\ C_2 \\ a \end{bmatrix} = \begin{bmatrix} \dfrac{mla_y + J\dot{r}}{l\cos\delta} + F_{x1}\tan\delta - \dfrac{M_{z,c}}{l\cos\delta} \\ -\dfrac{J\dot{r}}{l} + \dfrac{M_{z,c}}{l} \end{bmatrix}$$

(5.9)
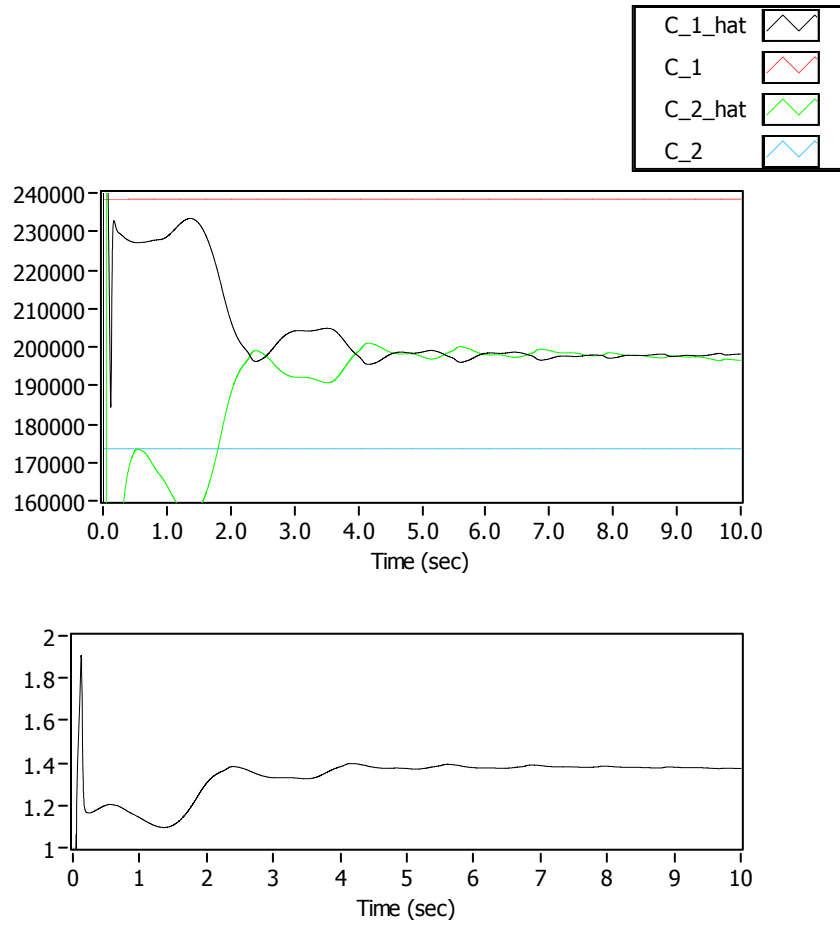
Figure 5.10: RLS Estimation of Axle Cornering Stiffnesses and Center of Gravity Longitudinal Location

The results of estimation for the sine sweep steer input simulation are shown in Figure 5.10. Note that the final estimated center of gravity longitudinal location is ~1.38 m, which is half of the vehicle wheelbase of 2.776 m. In addition, the identified cornering stiffnesses are approximately equal. The results seem to indicate that there is not enough information contained in the system model to differentiate between CG longitudinal location and differences in front and rear cornering stiffnesses.

Chapter Summary

This chapter presented a method of vehicle parameter identification using recursive least squares to identify axle cornering stiffness coefficients and vehicle yaw moment of inertia. The lateral force and yaw moment balance equations were rearranged into a linear regression form assuming linear lateral force response of the tires. A forgetting factor was used to ensure that sudden changes in vehicle parameters may be detected quickly. The identification of cornering stiffness coefficients was shown to provide a means of adapting to changes in vehicle mass. Two vehicle loading conditions were used to validate the parameter identification strategy. In addition, another identification strategy to identify center of gravity longitudinal location along with cornering stiffness coefficients was examined. However, this approach failed to accurately identify the vehicle parameters, thus indicating that the simple force and moment model is insufficient without including further dependencies among these parameters. The identification axle cornering stiffness coefficients and vehicle moment of inertia will be shown to enable the ESC control strategy to adapt to changes in these parameters.

CHAPTER SIX

ADAPTIVE ELECTRONIC STABILITY CONTROL

Once axle lateral force saturation is detected, an ESC control strategy is used to maintain yaw stability of the vehicle. Two separate control strategies described below are used to determine a commanded brake force for each wheel of the vehicle. An ABS controller is then used to modulate wheel brake pressures to maintain stable longitudinal wheel slip. The roles of the ESC algorithms and ABS controller in the complete system are shown in Figure 6.1. The ESC algorithms compensate for the detected axle lateral force saturation described in 4.3 Axle Saturation and Friction Estimation. The ESC algorithms in turn produce desired longitudinal braking targets for the ABS controller. The ABS controller modulates wheel-end brake pressures to maintain longitudinal slip ratio of each wheel within a determined target range.

The ESC control strategy is comprised of two basic algorithms. The primary algorithm determines the reduction in yaw moment due to lateral force saturation of an axle and then generates an equivalent moment via differential braking of the opposite axle. The second algorithm predicts Time to Saturation (TTS) of the rear axle and applies differential braking of to the front axle before saturation occurs and stability is lost. The predictive TTS algorithm is given priority over the equivalent moment algorithm. This chapter discusses both ESC control strategies as well as the details of the ABS strategy.
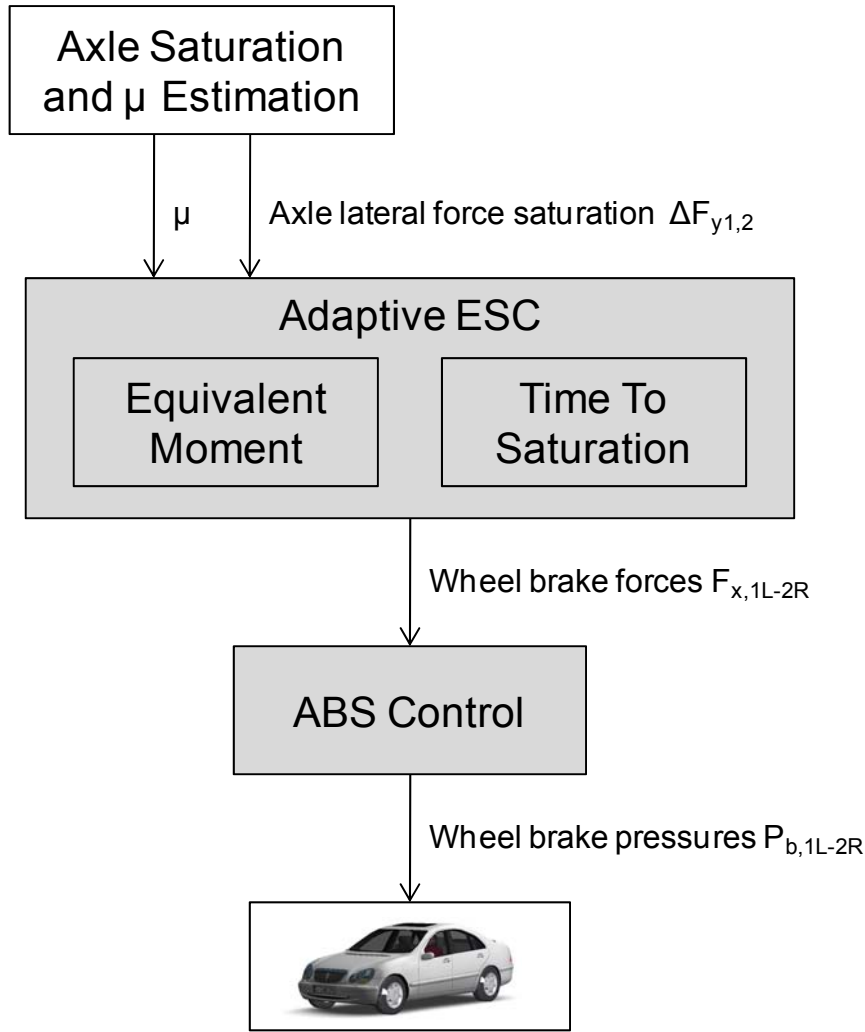
Figure 6.1: Role of ESC Algorithms and ABS Controller in Complete System

6.1 Equivalent Moment ESC Control Strategy

The ESC algorithm determines the reduction in yaw moment due to lateral force saturation of an axle and then generates a moment of the same magnitude via differential braking of the opposite axle. The term "Equivalent Moment" is defined in this work to refer to this ESC strategy. An ABS controller is also present and receives target wheel slip commands from the ESC controller. The ABS controller monitors wheel speed

sensor values and modulates brake pressure through a simple switching strategy to maintain wheel slip around a desired target value. For this research the ABS controller also takes advantage of the coefficient of friction estimated by the ESC controller to adapt slip targets. In addition the controller adjusts longitudinal slip targets to appropriate targets when slip angle is present using a simple model of combined slip.

The idea behind the equivalent moment control is that the reduced yaw moment of the saturated axle can be compensated by differential braking on the non-saturated axle. The reduction in yaw moment is due to the difference in lateral force generation between the linear model and the actual force generated at the axle. To compensate, differential braking may be used on the unsaturated axle, however the longitudinal braking force at one wheel will result in a corresponding reduction in lateral force generated by that wheel. Although this reduction is desirable since the reduction in lateral force of the braked wheel also helps compensate for the reduced yaw moment of the saturated axle, it must be accounted for when determining the braking force to apply to generate a net equivalent yaw moment on the vehicle. The concept of the friction ellipse is again employed to model the interaction of lateral and longitudinal forces as described in section 4.2 Estimation of Lateral Force Potential and illustrated in Figure 4.7.

6.1.1 Case 1: Front Axle Saturation in Left Turn

The linear lateral force model predicts a yaw moment as a function of the slip angles at the front and rear axles.

$$\sum_{i=1,2} M_{zi,p} = F_{y1,p}a - F_{y2,p}b = -C_1\alpha_1 a + C_2\alpha_2 b \qquad (6.1)$$

The actual moment generated due to the lateral forces of the wheels is:

$$\sum_{i=1,2} M_{zi} = F_{y1}^* a - F_{y2}^* b \qquad (6.2)$$

Note that here the theoretical lateral force potential of each axle is estimated from the estimated lateral and longitudinal forces. If the front axle is saturated, then $\left| F_{y1}^* \right| < \left| -C_1 \alpha_1 \right|$ and there is a corresponding reduction in yaw moment generated:

$$\Delta M_{z1} = \sum M_{z,p} - \sum M_z = -C_1 \alpha_1 a - F_{y1}^* a = \Delta F_{y1} a \qquad (6.3)$$
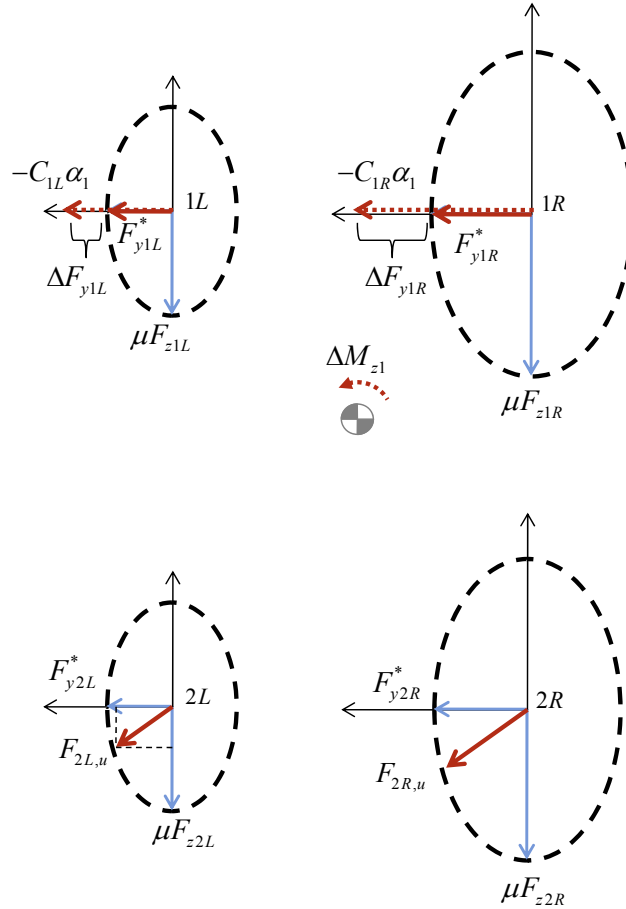
Figure 6.2: Missing Yaw Moment Due to Front Axle Lateral Force Saturation

The concept of the missing yaw moment is illustrated graphically in Figure 6.2. The figure shows the idealized lateral and longitudinal tire forces at each wheel of the vehicle viewed from above. The condition indicated is a left-hand turn with lateral force saturation of the front axle. The actual lateral forces of each wheel are indicated with solid vector arrows while the theoretical linear lateral force response $-C_{1j}\alpha_1$ of each tire is indicated with dashed arrow vectors. The resulting missing moment is indicated at the vehicle center of gravity with a dashed arrow.
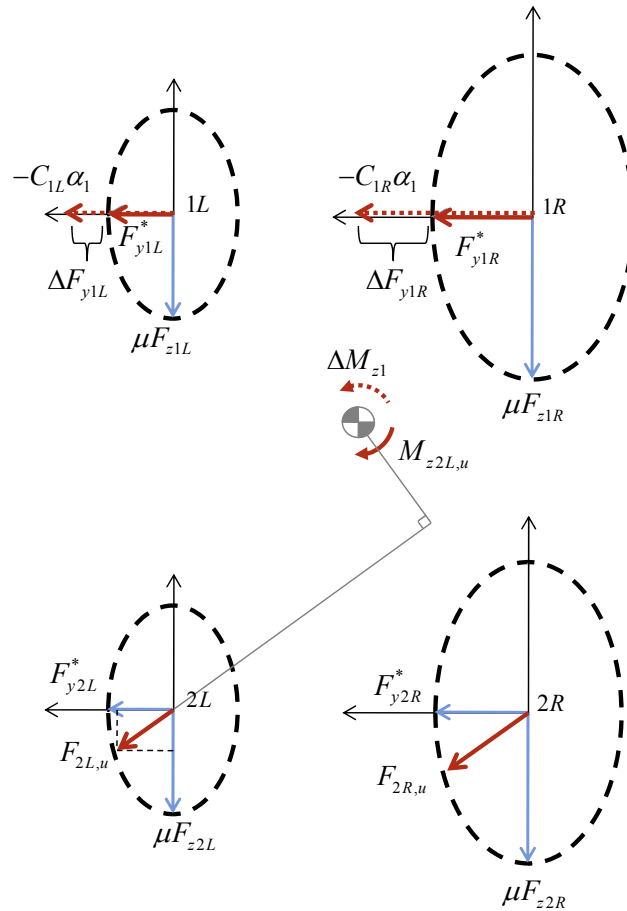
Figure 6.3: Yaw Moment Contribution of Left Rear Wheel Without ESC Differential Braking

To compensate for the reduced yaw moment, the left rear wheel may be braked to help induce the desired yaw motion of the vehicle. In this case there will be a net change in moment generated by this wheel due to changes in both lateral and longitudinal forces generated. Figure 6.3 shows the contribution of the left rear wheel resultant force to the yaw moment of the vehicle without controlled ESC braking. In this case the wheel forces are shown with an initial small amount of longitudinal force that may be present from sources such as driver braking or tire rolling resistance. As indicated in the figure, the uncontrolled moment contribution of this wheel $M_{z2L,u}$ is opposing the desired vehicle yaw motion in a left hand turn.

Since this wheel may already be braked due to ESC, the lateral and longitudinal forces that would be generated without braking must be estimated. The opposite wheel on the axle can be used to approximate the braking force that would be present at the current wheel without ESC intervention.

$$F_{x2L,u} = F_{x2R} \tag{6.4}$$

Here $F_{x2L,u}$ is the hypothetical longitudinal force that would be generated by the wheel if brake force due to ESC differential braking were not applied.

Since the lateral force potential of the actuated wheel is known, the corresponding unbraked lateral $F_{y2L,u}$ force may be determined using the friction ellipse.

$$\left(\frac{F_{y2L,u}}{F_{y2L}^{*}} \right)^{2} + \left(\frac{F_{x2L,u}}{\mu_{p}F_{z2L}} \right)^{2} = 1$$

$$F_{y2L,u} = F_{y2L}^{*} \sqrt{1 - \left(\frac{F_{x2L,u}}{\mu_{p}F_{z2L}} \right)^{2}} \tag{6.5}$$

When additional longitudinal braking is applied to this wheel by the ESC system brake actuation, there is a change in yaw moment contribution as shown in Figure 6.4. The additional longitudinal brake force is seen to change the direction of the yaw moment contribution of this wheel, thus with ESC braking this wheel now contributes to the desired yaw motion of the vehicle in the left hand turn. The Equivalent Moment ESC strategy takes advantage of this change in yaw moment contribution of the left rear wheel to compensate for the missing yaw moment due to lateral force saturation of the front wheels.
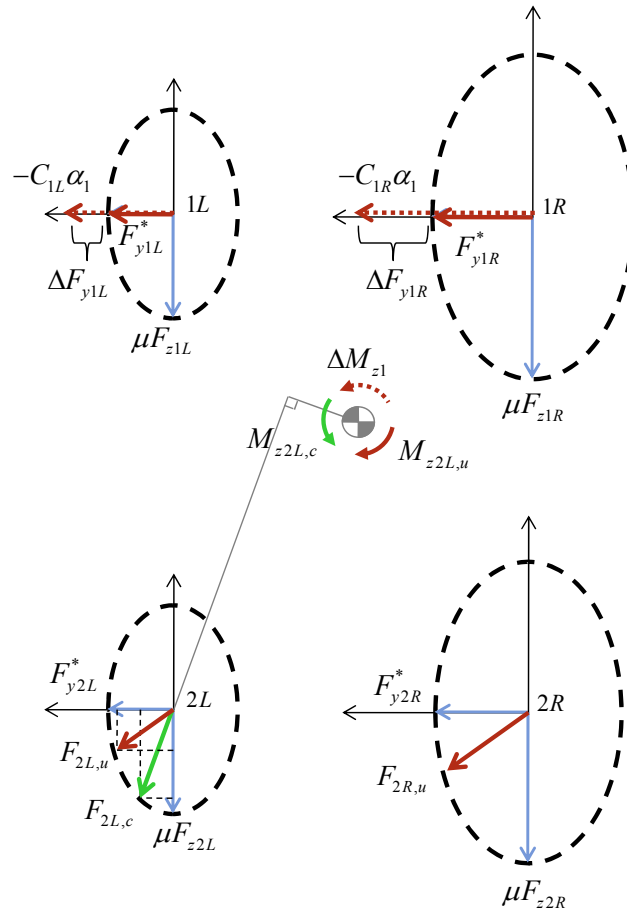
Figure 6.4: Yaw Moment Contribution of Left Rear Wheel With ESC Differential Braking

The net change in moment due to differential braking will be the difference between the braked and unbraked moment generation:

$$\Delta M_{z2L,c} = M_{z2L,c} - M_{z2L,u}$$

$$= -F_{y2L,c}b + F_{x2L,c}\frac{t}{2} - \left(-F_{y2L,u}b + F_{x2L,u}\frac{t}{2} \right)$$

$$= -F_{y2L,c}b + F_{x2L,c}\frac{t}{2} + F_{y2L,u}b - F_{x2L,u}\frac{t}{2}$$

(6.6)

In these equations the subscripts "c" and "u" are used to indicate conditions with controlled ESC braking and without ESC braking, respectively.

The equivalent moment principal dictates that the yaw moment due to the differential braking on the controlled axle must be equal to the reduction in yaw moment due to the saturated axle.

$$\Delta M_{z2L,c} = \Delta M_{z1}$$

$$-F_{y2L,c}b + F_{x2L,c}\frac{t}{2} + F_{y2L,u}b - F_{x2L,u}\frac{t}{2} = \Delta F_{y1}a$$

(6.7)

$$-F_{y2L,c}b + F_{x2L,c}\frac{t}{2} = \Delta F_{y1}a - F_{y2L,u}b + F_{x2L,u}\frac{t}{2}$$

As described above, the lateral and longitudinal forces at the left rear wheel are related by the friction ellipse during braking:

$$\left(\frac{F_{y2L,c}}{F_{y2L}^*} \right)^2 + \left(\frac{F_{x2L,c}}{\mu F_{z2L}} \right)^2 = 1$$

(6.8)

Here F_x^* has been replaced by the normal force times the peak friction coefficient since this is the maximum longitudinal force that can be generated. In addition, the lateral force potential F_{y2L}^* as described above is used to determine the maximum potential lateral force when no braking is applied.

Substituting for $F_{y2L,c}$ from the moment equation results in a quadratic equation in $F_{x2L,c}$:

$$\left(\frac{F_{x2L,c}\frac{t}{2b} - \Delta F_{y1}\frac{a}{b} + F_{y2L,u} - F_{x2L,u}\frac{t}{2b}}{F_{y2L}^*} \right)^2 + \left(\frac{F_{x2L,c}}{\mu F_{z2L}} \right)^2 = 1 \qquad (6.9)$$

Rearranged in standard quadratic form:

$$AF_{x2L,c}^{\;2} + BF_{x2L,c} + C = 0$$

$$A = \left(\frac{t}{F_{y2L}^* 2b} \right)^2 + \left(\frac{1}{\mu F_{z2L}} \right)^2$$

$$B = \frac{t}{F_{y2L}^* b}\left(\frac{-\Delta F_{y1}2a + F_{y2L,u}2b - F_{x2L,u}t}{F_{y2L}^* 2b} \right) \qquad (6.10)$$

$$C = \left(\frac{-\Delta F_{y1}2a + F_{y2L,u}2b - F_{x2L,u}t}{F_{y2L}^* 2b} \right)^2 - 1$$

A solution to the quadratic equation exists only if $B^2 - 4AC > 0$. If this condition is not met, then a different method must be employed to determine the appropriate brake force to use for differential braking. As the vehicle is in a left hand turn, F_{y2L}^* will normally be positive. In this case increasing the braking force on the left rear wheel also decreases the lateral force. Both of these actions act to increase the desired negative yaw moment. Therefore the maximum yaw moment is induced when full braking is applied and the only way that the quadratic equation may not be solved is if the desired yaw moment is higher than can be realized by braking this wheel. In this case the brake force may simply be set to the maximum possible brake force. The ABS controller will ensure that the wheel does not slip excessively when high brake pressure is applied to achieve the high longitudinal braking force.

$$F_{x2L,c} = \frac{2}{t}\Delta F_{y1}a - \frac{2}{t}F_{y2L,u}b + F_{x2L,u} \tag{6.11}$$

However, the case when $F_{y2L}{}^*$ is negative must be considered as this situation is possible during transient maneuvers. In this case the negative lateral force contributes to the desired yaw moment of the vehicle. Increasing brake force will reduce the lateral force, which will reduce the contribution of the wheel lateral force to the desired negative moment. At some particular brake force less than the maximum possible, the maximum possible yaw moment in the negative direction may be realized. If the desired yaw moment exceeds this maximum possible value, the quadratic equation cannot be solved and the brake force should be set to the value corresponding to maximum yaw moment. This brake force that maximizes the yaw moment may be found by setting the derivative of the moment equation equal to zero.

$$\begin{aligned}\Delta M_{z2L,c} &= \frac{t}{2}\left(F_{x2L,c} - F_{x2L,u}\right) - b\left(F_{y2L,c} - F_{y2L,u}\right)\\[2mm]&= \frac{t}{2}\left(F_{x2L,c} - F_{x2L,u}\right) - b\left[F_{y2L}^*\sqrt{1 - \left(\frac{F_{x2L,c}}{F_{x2L}^*}\right)^2} - F_{y2L,u}\right]\end{aligned} \tag{6.12}$$

Taking the derivative with respect to $F_{x2L,c}$:

$$\frac{d\Delta M_{z2L,c}}{dF_{x2L,c}} = \frac{t}{2} - \frac{bF_{y2L}^*}{2}\left[1 - \left(\frac{F_{x2L,c}}{F_{x2L}^*}\right)^2\right]^{-\frac{1}{2}}\left(-\frac{2F_{x2L,c}}{F_{x2L}^{*2}}\right) = 0 \tag{6.13}$$

This equation may be solved for the longitudinal braking force.

$$F_{x2L,c} = F_{x2L}^*\sqrt{\frac{1}{\left(\dfrac{2bF_{y2L}^*}{tF_{x2L}^*}\right)^2 + 1}} \tag{6.14}$$

Note that this formulation ensures that the square root function must only consider the range of input and output from 0 to 1 for ease of computation.

6.1.2 Case 2: Front Axle Saturation in Right Turn

A strategy for braking of the right rear wheel during front axle saturation in a right-hand turn may be derived similarly to the left rear wheel strategy. In this case the nominal longitudinal brake force of the right rear wheel without ESC intervention is assumed to be the same as that of the left rear wheel.

$$F_{x2R,u} = F_{x2L} \tag{6.15}$$

The net change in moment due to differential braking is therefore:

$$\Delta M_{z2R,c} = -F_{y2R,c}b - F_{x2R,c}\frac{t}{2} + F_{y2R,u}b + F_{x2R,u}\frac{t}{2} \tag{6.16}$$

The equivalent moment principal dictates that the yaw moment due to the differential braking on the controlled axle must be equal to the reduction in yaw moment due to the saturated axle.

$$\Delta M_{z2R,c} = \Delta M_z$$

$$-F_{y2R,c}b - F_{x2R,c}\frac{t}{2} = \Delta F_{y1}a - F_{y2R,u}b - F_{x2R,u}\frac{t}{2} \tag{6.17}$$

Again the assumption of the friction ellipse may be used to develop an equation quadratic in $F_{x2R,c}$ that may be solved to yield the desired longitudinal brake force.

$$AF_{x2R,c}^2 + BF_{x2R,c} + C = 0$$

$$A = \left(\frac{t}{F_{y2R}^* 2b}\right)^2 + \left(\frac{1}{\mu F_{z2R}}\right)^2$$

$$B = -\frac{t}{F_{y2R}^* b}\left(\frac{-\Delta F_{y1} 2a + F_{y2R,u} 2b + F_{x2R,u} t}{F_{y2R}^* 2b}\right) \qquad (6.18)$$

$$C = \left(\frac{-\Delta F_{y1} 2a + F_{y2R,u} 2b + F_{x2R,u} t}{F_{y2R}^* 2b}\right)^2 - 1$$

Again the brake force may be determined directly from the solution of the quadratic equation if the condition $B^2 - 4AC > 0$ holds. Otherwise the longitudinal brake force corresponding to the maximum yaw moment must be applied. The solution in this case depends on the direction of the rear axle lateral brake force. If this lateral force is negative as it would normally be in a right hand turn, the brake force should be set to the maximum possible.

$$F_{x2R,c} = -\frac{2}{t}\Delta F_{y1} a + \frac{2}{t}F_{y2R,u} b + F_{x2R,u} \qquad (6.19)$$

Otherwise if the rear axle lateral force is in the positive direction, the brake force yielding maximum possible moment must be found by differentiating the moment equation, setting this equation equal to zero and solving for the brake force.

$$F_{x2R,c} = F_{x2R}^* \sqrt{\frac{1}{\left(\dfrac{2bF_{y2R}^*}{tF_{x2R}^*}\right)^2 + 1}} \qquad (6.20)$$

6.1.3 Case 3: Rear Axle Saturation in Left Turn

A strategy for braking of the right front wheel during rear axle saturation in a left-hand turn may be derived similarly to the strategy for the front wheels. Note that the

difference in this case is that the longitudinal and lateral tire forces are in the wheel coordinate system and should be resolved onto the vehicle coordinate system due to steer angle. However if the steer angle is assumed to be small the two coordinate systems may be confused. Testing has shown that the simplified equations derived here assuming no steer angle of the front wheels produce acceptable ESC system performance.

If the rear axle is saturated, then $\left| F_{y2}^* \right| < \left| -C_2\alpha_2 \right|$ and there is a corresponding reduction in yaw moment generated.

$$\Delta M_z = \sum M_{z,p} - \sum M_z = C_2\alpha_2 b - \left(-F_{y2}^* b \right) = -\Delta F_{y2} b \qquad (6.21)$$

In this case the nominal longitudinal brake force of the right front wheel without ESC intervention is assumed to be the same as that of the left front wheel.

$$F_{x1R,u} = F_{x1L} \qquad (6.22)$$

The net change in moment due to differential braking is therefore:

$$\Delta M_{z1R,c} = F_{y1R,c}a - F_{x1R,c}\frac{t}{2} - F_{y1R,u}a + F_{x1R,u}\frac{t}{2} \qquad (6.23)$$

The equivalent moment principal dictates that the yaw moment due to the differential braking on the controlled axle must be equal to the reduction in yaw moment due to the saturated axle.

$$\Delta M_{z1R,c} = \Delta M_z$$

$$F_{y1R,c}a - F_{x1R,c}\frac{t}{2} = -\Delta F_{y2}b + F_{y1R,u}a - F_{x2R,u}\frac{t}{2} \qquad (6.24)$$

Again the assumption of the friction ellipse may be used to develop an equation quadratic in $F_{x1R,c}$ that may be solved to yield the desired longitudinal brake force.

$$AF_{x1R,c}{}^2 + BF_{x1R,c} + C = 0$$

$$A = \left(\frac{t}{F_{y1R}^* 2a}\right)^2 + \left(\frac{1}{\mu F_{z1R}}\right)^2$$

$$B = \frac{t}{F_{y1R}^* a}\left(\frac{-\Delta F_{y2} 2b + F_{y1R,u} 2a - F_{x1R,u} t}{F_{y1R}^* 2a}\right) \qquad (6.25)$$

$$C = \left(\frac{-\Delta F_{y2} 2b + F_{y1R,u} 2a - F_{x1R,u} t}{F_{y1R}^* 2a}\right)^2 - 1$$

Again the brake force may be determined directly from the solution of the quadratic equation if the condition $B^2 - 4AC > 0$ holds. Otherwise the longitudinal brake force corresponding to the maximum yaw moment must be applied. The solution in this case depends on the direction of the front axle lateral brake force. If this lateral force is positive as it would normally be in a left hand turn, the brake force should be set to the maximum possible.

$$F_{x1R,c} = \frac{2}{t}\Delta F_{y2}b - \frac{2}{t}F_{y1R,u}a + F_{x1R,u} \qquad (6.26)$$

Otherwise if the rear axle lateral force is in the negative direction, the brake force yielding maximum possible moment must be found by differentiating the moment equation, setting this equation equal to zero and solving for the brake force.

$$F_{x1R,c} = F_{x1R}^* \sqrt{\frac{1}{\left(\frac{2aF_{y1R}^*}{tF_{x1R}^*}\right)^2 + 1}} \qquad (6.27)$$

6.1.4 Case 4: Rear Axle Saturation in Right Turn

A strategy for braking of the left front wheel during rear axle saturation in a right-hand turn may be derived similarly to the strategy for the right front wheel. In this case

the nominal longitudinal brake force of the left front wheel without ESC intervention is assumed to be the same as that of the right front wheel.

$$F_{x1L,u} = F_{x1R} \tag{6.28}$$

The net change in moment due to differential braking is therefore:

$$\Delta M_{z1L,c} = F_{y1L,c}a + F_{x1L,c}\frac{t}{2} - F_{y1L,u}a - F_{x1L,u}\frac{t}{2} \tag{6.29}$$

The equivalent moment principal dictates that the yaw moment due to the differential braking on the controlled axle must be equal to the reduction in yaw moment due to the saturated axle.

$$\Delta M_{z1L,c} = \Delta M_z$$

$$F_{y1L,c}a + F_{x1L,c}\frac{t}{2} = -\Delta F_{y2}b + F_{y1L,u}a + F_{x2L,u}\frac{t}{2} \tag{6.30}$$

Again the assumption of the friction ellipse may be used to develop an equation quadratic in $F_{x1L,c}$ that may be solved to yield the desired longitudinal brake force.

$$AF_{x1L,c}^{2} + BF_{x1L,c} + C = 0$$

$$A = \left(\frac{t}{F_{y1L}^{*}2a}\right)^{2} + \left(\frac{1}{\mu F_{z1L}}\right)^{2}$$

$$B = -\frac{t}{F_{y1L}^{*}a}\left(\frac{-\Delta F_{y2}2b + F_{y1L,u}2a + F_{x1L,u}t}{F_{y1L}^{*}2a}\right) \tag{6.31}$$

$$C = \left(\frac{-\Delta F_{y2}2b + F_{y1L,u}2a + F_{x1L,u}t}{F_{y1L}^{*}2a}\right)^{2} - 1$$

Again the brake force may be determined directly from the solution of the quadratic equation if the condition $B^2 - 4AC > 0$ holds. Otherwise the longitudinal brake force corresponding to the maximum yaw moment must be applied. The solution in this

case depends on the direction of the front axle lateral brake force. If this lateral force is negative as it would normally be in a right hand turn, the brake force should be set to the maximum possible.

$$F_{x1L,c} = -\frac{2}{t}\Delta F_{y2}b + \frac{2}{t}F_{y1L,u}a + F_{x1L,u} \tag{6.32}$$

Otherwise if the rear axle lateral force is in the positive direction, the brake force yielding maximum possible moment must be found by differentiating the moment equation, setting this equation equal to zero and solving for the brake force.

$$F_{x1L,c} = F_{x1L}^* \sqrt{\frac{1}{\left(\frac{2aF_{y1L}^*}{tF_{x1L}^*}\right)^2 + 1}} \tag{6.33}$$

6.1.5 Case 5: Saturation of Both Axles

Special consideration must be given to the case when both axles are saturated in lateral force generation. In cases of large saturation such as driving on ice, the driver may input large steering input to the front wheels to overcorrect for the lateral force saturation. Applying differential braking to the rear axle would enable the vehicle to yaw in the direction desired by the driver. However if the rear axle is already saturated as well, the yaw motion would further saturate both axles and could lead to a spinout condition. In addition, even if complete control of the vehicle is not lost, to recover from the turn, the vehicle would need to travel back through the developed yaw angle before straightening or beginning a turn in the opposite direction. In this case the excessive buildup of yaw rate could lead to further instability or loss of control.

For these reasons, priority is given to rear axle saturation when saturation of both axles is detected. Differential braking is applied to the front axle to restore the rear axle slip angle to the usable range. While some loss of cornering capability occurs because of differential braking on the front axle, vehicle stability is maintained by minimizing slip angle of the rear axle.

6.2 Time To Saturation (TTS) Predictive ESC Control

Often by the time rear axle saturation is detected, the vehicle has significant angular momentum. Differential braking applied after axle saturation is detected is often insufficient to overcome this angular momentum. Therefore to maintain stability of the vehicle a control strategy that anticipates rear axle saturation and applies differential braking before this situation occurs is desired. The strategy here compares a computed Time To Saturation (TTS) and a Time To Recover (TTR) and applies maximum differential braking when $TTS \le TTR$.

6.2.1 Time To Saturation Calculation

The linearized equation of the slip angle for the rear axle is

$$\alpha_2 = \arctan\left(\frac{v_y - br}{v_x}\right) \approx \frac{v_y - br}{v_x} \tag{6.34}$$

Considering a right hand turn, slip angle of the rear axle is generally positive. The risk of rear axle saturation occurs when the slip angle corresponding to maximum lateral force is realized. For an ideal tire model, this saturation would occur when the linear cornering stiffness is equal to the maximum traction force available.

$$\alpha_{2,sat,ideal} = \frac{\mu F_{z,2}}{C_2} \tag{6.35}$$

For real tires, the actual slip angle at saturation is considerably higher than this ideal value since lateral force deviates from the linear curve at relatively low slip angles. For the tire models used for the simulated sedan for evaluation of the ESC algorithm, the peak lateral force occurs at a value of slip angle approximately 2.3 times that of the idealized value.

$$\alpha_{2,sat} = 2.3 \frac{\mu F_{z,2}}{C_2} \tag{6.36}$$

Assuming that the vehicle speed is constant, the rate of change or rear slip angle is

$$\dot{\alpha}_2 \approx \frac{\dot{v}_y - b\dot{r}}{v_x} \tag{6.37}$$

If this value is positive during a right hand turn, then the vehicle is oversteering and there is a risk that there is impending saturation of the rear axle. In this case both yaw rate and yaw acceleration are negative. If the rate of change of vehicle sideslip and rate of change of yaw rate are assumed to be constant, then the slip angle increases linearly over time.

$$\alpha_2(t) = \alpha_{2,0} + \dot{\alpha}_2 t$$
$$\alpha_2(t) = \alpha_{2,0} + \frac{\dot{v}_y - b\dot{r}}{v_x} t \tag{6.38}$$

Therefore the Time To Saturation (TTS) can be calculated directly from this relationship.

$$\alpha_2(t_{sat}) = \alpha_{2,sat}$$

$$\alpha_{2,0} + \frac{\dot{v}_y - b\dot{r}}{v_x} t_{sat} = 2.3 \frac{\mu F_{z,2}}{C_2}$$

$$\frac{\dot{v}_y - b\dot{r}}{v_x} t_{sat} = 2.3 \frac{\mu F_{z,2}}{C_2} - \alpha_{2,0} \qquad (6.39)$$

$$t_{sat} = \frac{v_x}{\dot{v}_y - b\dot{r}} \left(2.3 \frac{\mu F_{z,2}}{C_2} - \alpha_{2,0} \right)$$

Note that this TTS value may be computed directly as the vehicle lateral velocity observer computes the rate of change of lateral velocity directly and the force observer computes the yaw acceleration. The current slip angle and static axle normal load are also known.

Note that the assumption that the rate of change of lateral velocity and yaw acceleration are constant may not be true over the period of time until the axle is saturated. However if control action of the ESC controller is assumed to limit the amplitude of these values to their current value or less, then the estimate of TTS represents the minimum time to saturation (i.e. worst case).

6.2.2 Time To Recover Calculation

The time required to for the ESC differential braking to stop the increase in rear axle slip angle is referred to as the time to recover. This value represents the time required to stop the increase in rear axle slip angle if maximum available differential braking is applied to the front axle and maintained.

In order to stop further increase in rear axle slip angle, the rate of change of this angle must be zero.

$$\dot{\alpha}_2 = 0$$
$$\dot{v}_y - b\dot{r} = 0 \tag{6.40}$$

Therefore slip angle will be stabilized if both lateral velocity and yaw rate are stabilized. The rate of change of lateral velocity is related to lateral acceleration and yaw rate by the kinematic relationship used by the lateral velocity observer.

$$\dot{v}_y = a_y - v_x r \tag{6.41}$$

Therefore if yaw rate is held constant at the value that makes this expression zero, the rear slip angle value will be stabilized.

$$r_{rec} = \frac{a_y}{v_x} \tag{6.42}$$

Given the current yaw rate and the desired yaw rate for recovery, the following equation based on impulse and momentum principles applies.

$$Jr_0 + \int_0^{t_{rec}} M_z(t)dt = Jr_{rec} \tag{6.43}$$

The moment applied to the vehicle will have contributions from differential braking as well as the lateral forces generated at both axles.

$$Jr_0 + \int_0^{t_{rec}} M_{z,c}(t)dt + \int_0^{t_{rec}} aF_{y1}(t) - bF_{y2}(t)dt = Jr_{rec} \tag{6.44}$$

If the max differential braking is applied to the front axle during this time, the moment contribution will be approximately constant. The lateral forces generated by both axles however will not be constant as the slip angles will be changing. However at or very near axle saturation, the lateral force generation of the axles will be limited by the normal loads and the coefficient of friction.

$$aF_{y1,sat} - bF_{y2,sat} = a\mu F_{z1} - b\mu F_{z2}$$
$$= a\mu \frac{b}{l}F_z - b\mu \frac{a}{l}F_z$$
$$= \frac{\mu}{l}F_z(ab - ba)$$
$$= 0$$

(6.45)

Although for the TTS calculation the slip angle is assumed to increase linearly, such an assumption of linear increase in lateral force generated cannot be made. In order to accurately predict the behavior of the lateral force over time, an axle lateral force model would need to be incorporated. In addition, the solution of the impulse and momentum equation would require forward simulation to solve since a closed form solution would not be possible.

For these reasons, an approximation of lateral force is made. The lateral forces are assumed to linearly increase from the present value to the saturation value at the time of recovery. In this manner the average lateral force is then

$$F_{y1,avg} = \frac{1}{2}\left(F_{y1,0} + F_{y1,sat}\right) = \frac{1}{2}\left(F_{y1,0} + \mu F_{z1}\right)$$

$$F_{y2,avg} = \frac{1}{2}\left(F_{y2,0} + F_{y2,sat}\right) = \frac{1}{2}\left(F_{y2,0} + \mu F_{z2}\right)$$

(6.46)

Assuming these average values of lateral force and a constant differential braking force, the time to recover may be calculated directly from the impulse and momentum relationship.

$$Jr_0 + \int_0^{t_{rec}} M_{z,c}dt + \int_0^{t_{rec}} aF_{y1,avg} - bF_{y2,avg}dt = Jr_{rec}$$

$$Jr_0 + \int_0^{t_{rec}} -\frac{t}{2}\mu F_{z1R}dt + \int_0^{t_{rec}} \frac{a}{2}\left(F_{y1,0} + \mu F_{z1}\right) - \frac{b}{2}\left(F_{y2,0} + \mu F_{z2}\right)dt = Jr_{rec} \quad (6.47)$$

$$Jr_0 + \left[-\frac{t}{2}\mu F_{z1R} + \frac{a}{2}\left(F_{y1,0} + \mu F_{z1}\right) - \frac{b}{2}\left(F_{y2,0} + \mu F_{z2}\right)\right]t_{rec} = Jr_{rec}$$

Rearranging,

$$
\begin{aligned}
t_{rec} &= \frac{J\left(r_0 - r_{rec}\right)}{\dfrac{t}{2}\mu F_{z1R} - \dfrac{a}{2}\left(F_{y1,0} + \mu F_{z1}\right) + \dfrac{b}{2}\left(F_{y2,0} + \mu F_{z2}\right)} \\[2em]
&= \frac{J\left(r - \dfrac{a_y}{v_x}\right)}{\dfrac{t}{2}\mu F_{z1R} - \dfrac{a}{2}\left(F_{y1} + \mu F_{z1}\right) + \dfrac{b}{2}\left(F_{y2} + \mu F_{z2}\right)}
\end{aligned}
\tag{6.48}
$$

Note that the approximation in axle lateral force assumed may result in a negative time to recover since the moment due to differential braking may be insufficient to overcome the moment due to axle lateral forces. However simulations have shown this to occur only during initial transients in which lateral force is significant in the front axle before it has had a chance to develop in the rear axle. Although the negative time is an anomaly and slightly delays ESC intervention, it may prevent unnecessary intervention during transient maneuvers. In addition the ESC control with TTS is found to only have a delay of ~0.1 seconds when time to recover is negative, resulting in satisfactory performance in stabilizing an oversteering vehicle.

6.3 Anti-Lock Braking System Control

The ABS controller monitors wheel speed sensor values and modulates brake pressure through a simple switching strategy to maintain wheel slip around a desired target value. For this research the ABS controller also takes advantage of the coefficient of friction estimated by the ESC controller to adapt slip targets. In addition the controller adjusts longitudinal slip targets to appropriate targets when slip angle is present using a simple model of combined slip.

6.3.1 Basic ABS Slip Controller

Wheel speeds are measured by commercially available sensors. It is assumed that the vehicle forward velocity v_x can be determined by the ABS controller from wheel speeds. There are a number of approaches to estimating longitudinal velocity in the literature, and the focus of this research is on the ESC algorithm. Slip ratio is maintained within a nominal range of 0.07 to 0.10, where slip ratio is defined as:

$$\kappa = 1 - \frac{\omega_i r}{v_x}$$

(6.49)

The controller simulates a valve that enables and disables a brake pressure to each wheel. The brake pressure is the maximum of the ESC command pressure and the driver brake pedal pressure realized at the master cylinder. It is assumed that the brake system is capable of supplying an ESC commanded brake pressure up to 15 MPa. The master cylinder brake pressure has a bias to the front such that the brake pressure at the rear wheels is only 40% of the full master cylinder pressure which is delivered to the front wheels. Note that simulations were not conducted with driver braking applied for this research.

The slip ratio controller uses a simple threshold with a hysteresis to maintain wheel slip in the desired range. Brake pressure is applied until the wheel slip exceeds the upper target, at which point no further brake pressure is applied. The brake pressure is then withheld until the slip value is less than the lower target value. At this point full brake pressure is applied again and the cycle is repeated. Combined with the brake and wheel dynamics, the simulated ABS system and vehicle model in CarSim result in an on/off cycling at around 10Hz, which is a rate typical of an actual vehicle.

The slip targets are established to try to maintain maximum tractive force, however with a bias towards the lower slip values. The tire model used in CarSim achieves maximum longitudinal force at a slip value of 0.12. The slip values are maintained below this maximum for two reasons. First the wheel dynamics become unstable at slip values above maximum longitudinal force slip value since increasing slip results in reduced longitudinal force. It is very difficult for the controller to prevent wheel lock (100% slip) in this case as this happens very quickly due to the unstable wheel dynamics. Second, the higher the longitudinal slip, the less lateral force generation is possible. Therefore to prevent wheel dynamics instability and provide a compromise between longitudinal and lateral force generation, the slip is maintained at values less than the slip value corresponding to maximum longitudinal force.

6.3.2 Coefficient of Friction Compensation of Slip Targets

Longitudinal force generation is greatly affected by the friction generated between the road and the tire. Environmental conditions such as rain, ice or snow can greatly reduce the coefficient of friction of the tire on the road [14]. When the coefficient of friction is reduced, the maximum longitudinal force potential and the value of slip at which the maximum force is generated are both reduced significantly. Therefore target values of slip for the ABS controller may actually be too high in the case of reduced coefficient of friction and may actually attempt to maintain slip at values well above that of the maximum longitudinal force slip.

CarSim simulates uses a method referred to as similarity to adjust the tire data provide in tables of longitudinal force versus slip [51].

$$F_x = \frac{\mu}{\mu_0} FX(F_z, \frac{\mu_0}{\mu} \kappa) \quad\quad (6.50)$$

Here "FX" is a two-dimensional lookup table of longitudinal force for given tire normal load and longitudinal slip. μ is the current road/tire coefficient of friction, while μ_0 is the nominal coefficient of friction defined for the look-up table data.

Since the value of coefficient of friction is estimated by the ESC controller, this value is available and may be used by the ABS controller to adapt longitudinal slip targets to appropriate values. The ABS controller thus modifies the upper and lower slip targets by:

$$\kappa_{UL} = \frac{\mu}{\mu_0} \kappa_{UL,0}$$
$$\kappa_{LL} = \frac{\mu}{\mu_0} \kappa_{LL,0} \quad\quad (6.51)$$

κ_{UL} and κ_{LL} are the upper and lower slip ratio target limits after compensating for coefficient of friction, while $\kappa_{UL,0}$ and $\kappa_{LL,0}$ are the nominal slip ratio targets assuming high coefficient of friction μ_0.

This ensures that longitudinal slip is maintained below the value of slip corresponding to the maximum possible longitudinal braking force at the current coefficient of friction.

6.3.3 Combined Lateral/Longitudinal Slip Compensation of Slip Targets

A combined slip model may be used to determine the lateral and longitudinal tire forces when both longitudinal slip and slip angle are nonzero. This theory ensures that the total combined wheel slip does not exceed the maximum possible slip, and attempts to determine realistic force generation corresponding to the combined slip [14]. As a

result, the longitudinal force curves as a function of slip angle not only change in magnitude, they also change in shape. These curves for the sedan tire model used in simulations are shown for values of slip angle ranging from 0 to 20 deg are shown in Figure 6.5.
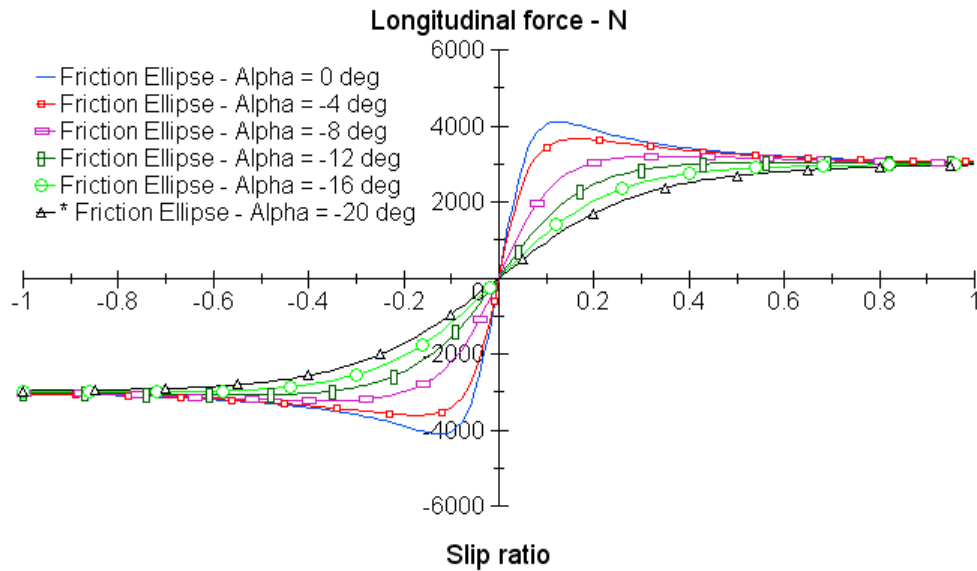
Figure 6.5: Combined long/lat slip for 215/55R17 tire model with Fz = 4,125 N

Clearly from these curves, a target longitudinal slip value of 0.085 used by the ABS controller will result in a significant reduction in longitudinal force generation. The actual values of longitudinal force and their percentage of longitudinal force with no slip angle are shown in Table 6.1. Such high slip angles may occur when high rates of steering wheel angle are input by the driver in obstacle avoidance maneuvers or on low friction surfaces. The reduction in longitudinal force generation will severely limit the corrective action of the ESC system in such conditions.

Table 6.1: Reduction in Tire Longitudinal Force with Slip Angle

Slip angle, α (deg)	Longitudinal Force, $F_x(\kappa=0.085,\alpha)$ (N)	% Longitudinal Force at $F_{x0}(\kappa=0.085, \alpha=0)$
0	3890	100%
4	3267	84.0%
8	2042	52.5%
12	1370	35.2%
16	1024	26.3%
20	814	20.9%

In addition to the reduction in force as slip angle increases, Figure 6.5 shows that the slip ratio corresponding to maximum longitudinal force increases significantly. In fact for slip angles greater than ~10 deg, the maximum longitudinal force corresponds to the longitudinal force of pure sliding (100% slip) and occurs at a slip ration of 1.

In the combined slip theory, the change in magnitude comes primarily from a scaling of the force generation by the ratio of slip to combined slip [14].

$$F_x \approx \frac{\sigma_x}{\sigma_{total}} F_x(\kappa)$$

$$F_y \approx \frac{\sigma_y}{\sigma_{total}} F_y(\alpha)$$

(6.52)

Where

$$\sigma_x = -\frac{\kappa}{1+\kappa}$$

$$\sigma_y = \frac{\tan(\alpha)}{1+\kappa}$$

$$\sigma_{total} = \sqrt{\sigma_x^2 + \sigma_y^2}$$

(6.53)

Therefore

$$F_x \approx \frac{\kappa}{\sqrt{\kappa^2 + \tan(\alpha)^2}} F_x(\kappa)$$ (6.54)

This accounts for the large reduction in longitudinal force generation when slip angle is high, as seen in table. To account for this, the slip ratio targets for the ABS controller may be adjusted accordingly to maintain a compromise between lateral and longitudinal force generation. For example if the slip ratio is equal to the tangent of the slip angle, then both forces will be approximately 70% of their nominal values. Note that this is only a rough approximation, as the complete combined slip theory actually changes the shape of the force curves as seen above.

As the ESC algorithm includes an estimate of axle slip angle for each axle, the target slip ratio for the ABS controller may be modified as:

$$\kappa_{UL} = \max\left(\kappa_{UL,0}, |\tan(\alpha)|\right)$$
$$\kappa_{LL} = \max\left(\kappa_{LL,0}, |\tan(\alpha)|\right)$$ (6.55)

Values of corresponding longitudinal and lateral forces are shown in Table 6.2 and Table 6.3 for a nominal slip ratio target of 0.085. The longitudinal force generated at high slip angles is seen to be as much as three times that of the slip ratio target without modification. As desired the target slip ratio yields a reasonable compromise between lateral and longitudinal force generation. Note that although value of F_x at $\alpha = 20$ deg is only 62% of the longitudinal force at $\kappa = 0.085$, $\alpha = 0$ deg, this value is ~80% of the F_x of 3000 N at pure sliding (i.e. $\kappa = 1$).

Table 6.2: Compensated Longitudinal Slip Ratio Target Effect on Longitudinal Force

Slip angle, α (deg)	$\tan(\alpha)$	Longitudinal slip, $\kappa = \max[0.085,\tan(\alpha)]$	Longitudinal Force, $F_x(\kappa,\alpha)$ (N)	% Longitudinal Force at $F_{x0}(\kappa=0.085, \alpha=0)$
0	0	0.085	3890	100%
4	0.07	0.085	3267	84.0%
8	0.14	0.14	2708	69.6%
12	0.21	0.21	2516	64.7%
16	0.29	0.29	2467	63.4%
20	0.36	0.36	2406	61.9%

Table 6.3: Compensated Longitudinal Slip Ratio Target Effect on Lateral Force

Slip angle, α (deg)	Lateral Force, $F_{y0}(\alpha,\kappa=0.085)$ (N)	Longitudinal slip, $\kappa = \max[0.085,\tan(\alpha)]$	Lateral Force, $F_y(\alpha,\kappa)$ (N)	% Lateral Force at $F_{y0}(\alpha,\kappa=0.085)$
4	2694	0.085	2694	100%
8	3380	0.14	2719	80.4%
12	3426	0.21	2547	74.3%
16	3457	0.29	2440	70.6%
20	3488	0.36	2432	69.7%

Chapter Summary

This chapter presented the core ESC and ABS strategies developed for this research work. The ESC strategy consists of two algorithms: Equivalent Moment and Time to Saturation. The Equivalent Moment strategy uses the friction ellipse approximation on the braked wheel to ensure that yaw moment developed by differential braking compensates for the moment lacking due to lateral force saturation of the opposite axle. When saturation of both axles are detected, differential braking on the front axle is used to prevent loss of control of the vehicle from rear axle saturation. The predictive Time to Saturation strategy enables differential braking to be applied before

saturation of rear axle lateral force occurs. This strategy simultaneously calculates an estimate of recovery time with differential braking and applies the braking when the time to recover is less than or equal to the estimated time to saturation. The Time to Saturation strategy is given priority over the Equivalent Moment strategy in order to ensure vehicle stability.

In addition, a basic ABS strategy to prevent wheel slip was presented. The need to adapt longitudinal slip ratio targets under low coefficient of friction conditions was explained. The friction estimate provided by the axle lateral force saturation detection enabled this adaptation. In addition, the need to adapt longitudinal slip ratio targets in the presence of high slip angle was discussed. The change in shape of the longitudinal force response to slip ratio when slip angles are large motivates a significant increase in slip ratio targets under these conditions.

CHAPTER SEVEN

ESC SYSTEM SIMULATION RESULTS

In order to test the adaptive ESC control strategy, co-simulation of the algorithm with a high fidelity vehicle model was conducted as illustrated in Figure 7.1. The vehicle parameter estimation and adaptive ESC strategy was implemented in LabVIEW using the LabVIEW Control Design and Simulation Module. A model of a typical D-class sedan was used in CarSim together with a simple driver model to follow various designed test maneuvers.
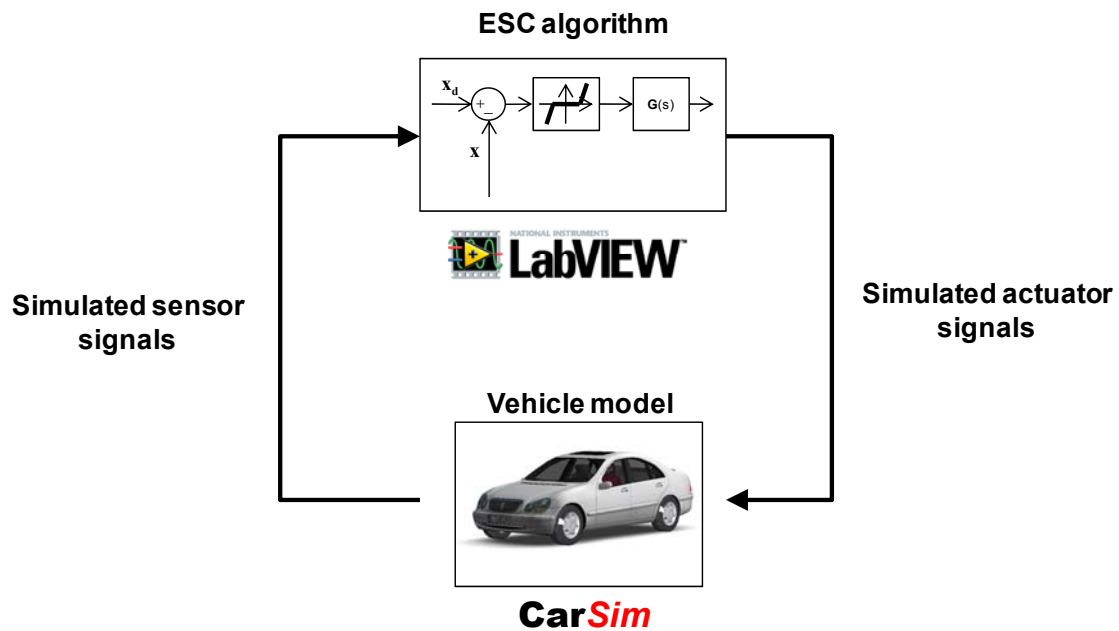
Figure 7.1: ESC Software Co-Simulation

At each simulated controller timestep of 1 millisecond, the simulated brake actuator pressures were sent from the controller to the CarSim model, and simulated sensor values were sent to the controller in LabVIEW. The LabVIEW model also included a simple first-order model of the brake hydraulic dynamics as the actuator signal sent to CarSim is the actual wheel-end brake pressure.

7.1 Test Vehicle Configurations

A nominal vehicle configuration simulating a typical D-class sedan was used with identical tire models on all four wheels. The ESC strategy utilizes the parameters of the nominal test vehicle shown in Table 7.1. The nominal axle cornering stiffness values are shown, however the ESC system is capable of estimating these values from the vehicle response as described above.

<p align="center">Table 7.1: Nominal Test Vehicle Parameters</p>

Parameter	Value	Units
Mass, m	1530	kg
Yaw moment of inertia, J	4607	kg*m^2
CG long. distance to front axle, a	1.139	m
CG long. distance to rear axle, b	1.637	m
Track width, t	1.55	m
Nominal front axle cornering stiffness, C_1	238,300	N/rad
Nominal rear axle cornering stiffness, C_2	173,500	N/rad
CG height from ground, h_G	0.519	m

From these basic parameters the bicycle model can be used to determine theortical values of basic vehicle handling parameters.

The theoretical understeer gradient can be calculated [14]:

$$K_{us} = \frac{mg}{l}\left(\frac{b}{C_1} - \frac{a}{C_2}\right)$$ (7.1)

For the nominal vehicle configuration, the understeer gradient is 0.00165 or 0.0944 deg/G. Therefore the nominal vehicle is an understeering vehicle with a characteristic speed of 463 kph. It should be noted that this is only an ideal value. The actual vehicle understeer gradient depends on many additional factors such as lateral load transfer and kinematic and compliance effects.

In order to characterize the vehicle handling response four performance parameters have been proposed: yaw rate steady state gain, yaw rate natural frequency, yaw rate damping ratio and lateral acceleration phase delay at 1 Hz [52, 53]. The theoretical ideal values may be calculated by hand [14, 52], or by simulation analysis in CarSim. The ideal values may be computed as follows.

Stability factor [14]:

$$K = \frac{m}{l^2}\left(\frac{b}{C_1} - \frac{a}{C_2}\right)$$ (7.2)

Yaw rate gain [14, 52]:

$$\frac{r}{\delta_{HW}} = \frac{v_x}{k_s l\left(1 + K v_x^2\right)}$$ (7.3)

Yaw rate natural frequency [14, 52]:

$$\omega_{n,r} = \frac{l}{v_x} \sqrt{\frac{C_1 C_2 \left(1 + K v_x^2\right)}{Jm}} \qquad (7.4)$$

Yaw rate damping ratio [14, 52]:

$$\zeta_r = \frac{J\left(C_1 + C_2\right) + m\left(a^2 C_1 + b^2 C_2\right)}{2l\sqrt{JmC_1 C_2 \left(1 + K v_x^2\right)}} \qquad (7.5)$$

Lateral acceleration phase delay at 1 Hz [52]:

$$\phi_{a_y} = \arctan\left(\frac{blC_2}{\dfrac{lC_2 v_x}{2\pi} - 2\pi J v_x}\right) - \arctan\left(\frac{2\zeta\omega_n}{\omega_n^2 - 1}\right) \qquad (7.6)$$

The test vehicle was characterized for understeer behavior by simulating a constant radius test in CarSim with slowly increasing vehicle speed. The result of this test is indicated as the "Nominal Sedan" in Figure 7.2. The oversteering sedan indicated in the figure is described as a second vehicle configuration below. From this test the simulated response understeer gradient shown in Table 7.2 was determined.
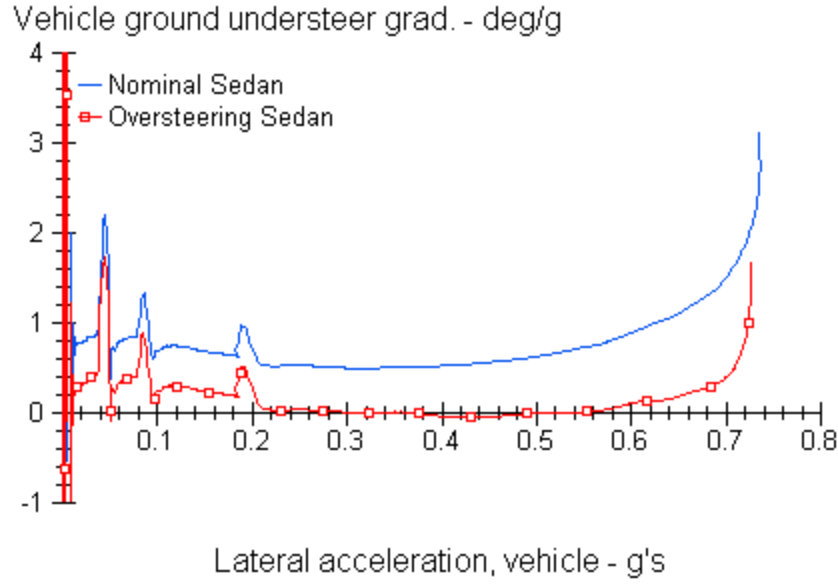
Figure 7.2: Constant Radius Circle Test Understeer Gradient Results

To evaluate the other four handling parameters, a simulation was conducted with an open-loop steer input of an exponential sine sweep from 0.02 to 20 Hz. A handwheel angle amplitude of 17 deg was used as this generates approximately 3 m/s^2 of steady state lateral acceleration at 100 kph. The yaw rate gain, natural frequency and yaw rate damping ratio were determined by using LabVIEW System Identification Toolkit functions to fit a second order transfer function to the yaw rate response data. The numerator order selected for identification was one while the denominator order was two according to the yaw rate response model of the bicycle model [14].

$$\frac{R(s)}{\Delta(s)} = \frac{lC_1C_2s + mv_xaC_1}{Jmv_xs^2 + \left[J(C_1+C_2) + m(a^2C_1+b^2C_2)\right]s + \frac{C_1C_2l^2}{v_x}(1+Kv_x^2)} \tag{7.7}$$

The simulation response for lateral acceleration phase delay at 1 Hz was determined from a frequency response function (FRF) analysis in CarSim of the sine

117

sweep simulation results. The value reported is an approximate value since no model was fit to the data and the FRF data exhibits some noise.

Table 7.2: Handling Parameters of Nominal Vehicle Model

Handling Parameter	Theoretical	Simulation Response
Understeer gradient, deg/G	0.094	0.50
Yaw rate steady state gain, s^{-1}	0.565	0.382
Yaw rate natural frequency, Hz	1.25	1.81
Yaw rate damping ratio	1.00	0.939
Lateral acceleration phase delay at 1 Hz, deg	16.1	-59

A second vehicle was configured for testing to simulate the conditions of worn tires on the rear axle of the vehicle. This was realized by replacing the rear tires of the nominal vehicle model with tires that have 80% of the capacity of the nominal tires with respect to lateral force, longitudinal force, aligning moment and camber thrust. As a result the vehicle parameters are identical to those of the nominal vehicle model, except that the nominal rear axle cornering stiffness is 138,800 N/rad. Thus this vehicle tends to oversteer in extreme handling maneuvers and thus is more prone to spinout and loss of vehicle control.

The resulting vehicle has an understeer gradient of -0.00723 or -0.414 deg/G, and thus exhibits oversteering behavior. This vehicle has a critical speed of 221 kph. Table shows the results of the theoretical values as well as the values determined from the same simulations as those executed for the nominal vehicle.

Table 7.3: Handling Parameters of Oversteering Vehicle Model

Handling Parameter	Theoretical	Simulation Response
Understeer gradient, deg/G	-0.0072	-0.05
Yaw rate steady state gain, s^{-1}	0.743	0.468
Yaw rate natural frequency	0.971	1.87
Yaw rate damping ratio	1.16	1.24
Lateral acceleration phase delay at 1 Hz, deg	13.7	-72

7.2 Test Maneuvers

Vehicle simulations were conducted using a variety of test maneuvers and test conditions. The ISO 3888-2 severe lane change was tested with both vehicle configurations on a high friction surface. The ISO 3888-1 high-speed double lane change was used to evaluate simulation performance of both vehicles on a low friction surface. Finally a fishhook maneuver was used to evaluate the propensity for spinout of the oversteering vehicle on a high friction surface.

7.2.1 Severe Double Lane Change Simulation

In order to evaluate the performance of the ESC control system in a real-world evasive action scenario, the ISO 3888-2 severe lane change maneuver was used [14, 54]. The standard defines cones for a two lane changes over a short distance and calls for an initial speed of 80 kph with no throttle applied during the maneuver. To successfully pass the test, a vehicle must proceed through the course without touching any cones marking the lanes.

To evaluate the vehicle performance with and without ESC, simulations of the severe lane change course were conducted using the CarSim driver model. A desired

vehicle path through the cones was developed and optimized to maximize the speed at which the vehicle without ESC could successfully navigate the course.

Plots of several different vehicle states for a severe double lane change maneuver are shown in Figure 7.3 through Figure 7.7. In Figure 7.3, the simulation with equivalent moment ESC enabled can be observed to follow the designed target path for the maneuver more closely than the simulation without ESC.
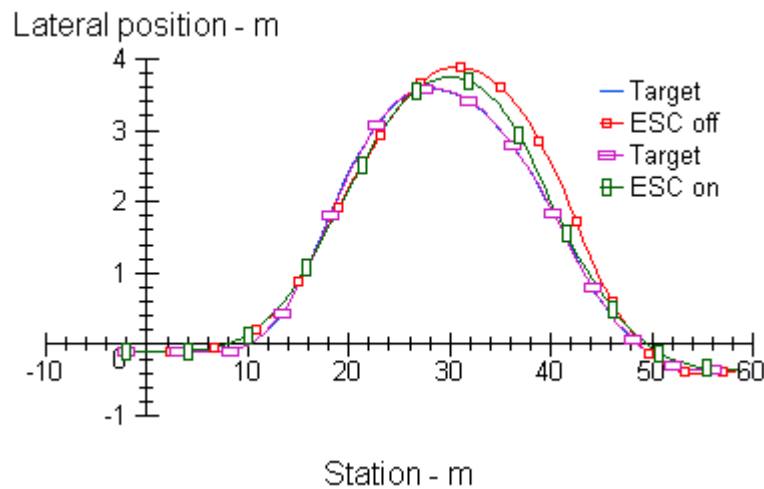
Figure 7.3: Tracking Results for Nominal Vehicle Severe Double Lane Change at 62 kph
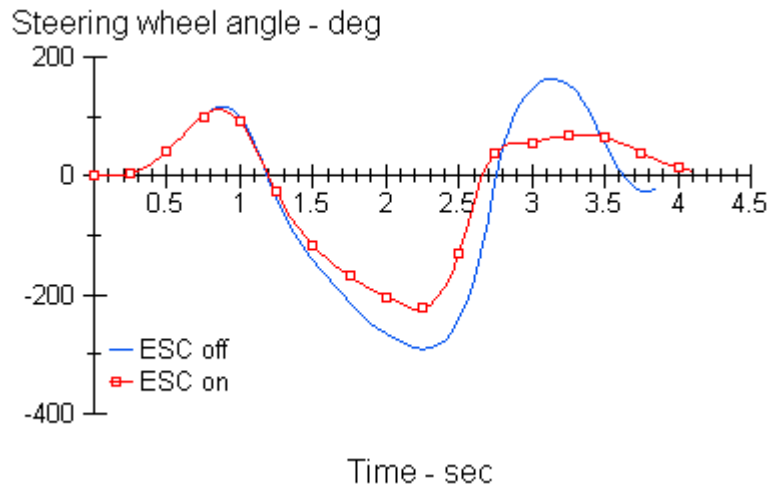
Figure 7.4: Steering Wheel Angle for Nominal Vehicle Severe Double Lane Change at 62 kph
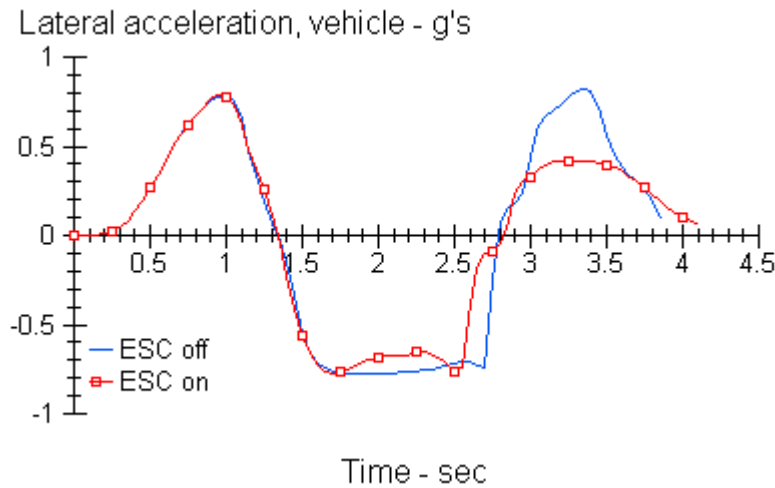
Figure 7.5: Lateral Acceleration for Nominal Vehicle Severe Double Lane Change at 62 kph

Figure 7.6 shows the longitudinal brake force of each wheel during the maneuver with ESC enabled. During the initial lane change to the left, lateral force saturation of the front axle is detected and the left rear wheel is braked to help initiate the turn. Almost immediately lateral force saturation of the rear axle is detected and the front right wheel

121

is braked to prevent vehicle oversteer. Then again as the vehicle is steered to the right to settle the vehicle in the left lane and begin the transition back to the right lane, the right rear wheel is braked to correct for understeer. This braking is alternated with front left wheel wheel braking as rear axle lateral force saturation is detected and corrected. By the transition back to the right lane at the end of the maneuver the ESC system has reduced vehicle speed such that the final turn does not require ESC system intervention.
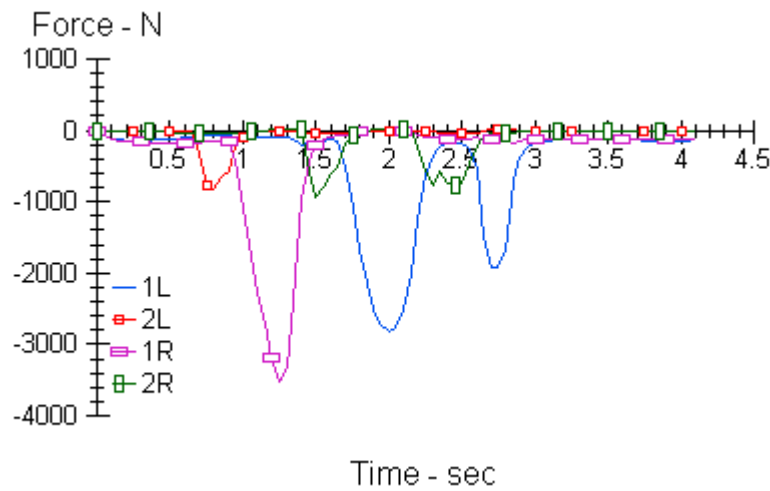
Figure 7.6: Wheel Longitudinal Force for Nominal Vehicle Severe Double Lane Change at 62 kph
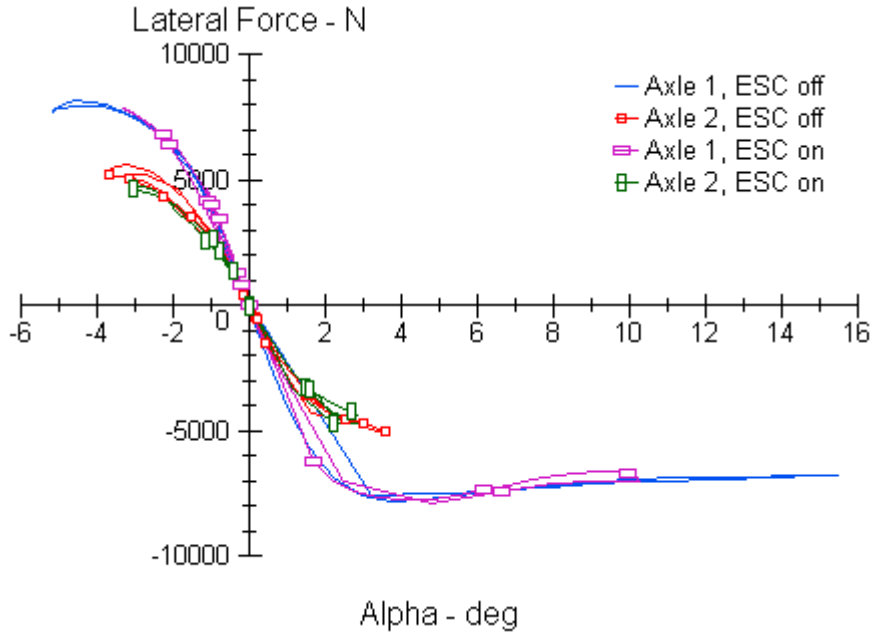
Figure 7.7: Lateral Force Characteristics for Nominal Vehicle Severe Double Lane Change at 62 kph

Figure 7.7 shows the axle lateral force plotted against the axle slip angle. Note that front axle lateral force saturates both with ESC enabled and disabled, however with ESC the maximum axle slip angle is reduced from roughly 15 deg to 10 deg.

Various metrics are used to quantify the performance of the ESC controller [55, 56]. These metrics are cost functions that can be compared for the same test conditions of the severe lane change maneuver executed with ESC enabled and with ESC disabled. The task performance may be evaluated by integrating the square of the lateral offset of the vehicle from the desired path [55].

$$J_T = \int_0^{t_f} \left(L_{y,target} - L_y \right)^2 dt \tag{7.8}$$

The physical workload of the driver may be evaluated by integrating the square of the steering wheel angle [55].

$$J_P = \int_0^{t_f} \delta_{HW}^2 dt \qquad (7.9)$$

Finally the mental workload of the driver may be evaluated by integrating the square of the steering wheel rate [56].

$$J_M = \int_0^{t_f} \dot{\delta}_{HW}^2 dt \qquad (7.10)$$

Table 7.4 show the values of these three cost functions for the severe lane change at 62 kph, both with ESC enabled and disabled. Although the vehicle successfully navigates the cones defining the lanes in both simulations, the vehicle with ESC enabled follows the desired path much closer. This can be seen in the task performance metric J_T, as well as observed in Figure 7.3. The physical workload of the driver was also significantly reduced, as evidenced by the physical workload metric J_P and Figure 7.4. The mental workload metric J_M was also reduced by almost half when the ESC system was enabled.

Table 7.4: Performance Metrics for Nominal Vehicle Severe Double Lane Change at 62.2 kph

Metric	ESC Off	ESC On	% Improvement
Task Performance, J_T (m^{2}s)	0.389	0.101	74%
Physical Workload, J_P (rad^{2}s)	28.5	15.3	46%
Mental Workload, J_M (rad^2/s)	209	105	50%

Table 7.5 shows the performance metrics for the oversteering vehicle in the same course. Note that the improvement in task performance is considerably less than that of the nominal understeering vehicle. This is because at the lower initial speed of 55.4 kph,

124

the vehicle is much better able to navigate the course than the nominal vehicle at 62.2 kph. This is evidenced by the fact that the task performance metric seen in Table 7.4 for the nominal vehicle is a full order of magnitude higher than that of Table 7.5 for the oversteering vehicle. The oversteering vehicle tends to hit the cones due to swing out of the rear of the vehicle, causing it to have a much lower speed through the course.

Table 7.5: Performance Metrics for Oversteering Vehicle Severe Double Lane Change at 55.4 kph

Metric	ESC Off	ESC On	% Improvement
Task Performance, J_T (m^2s)	0.0292	0.0266	9%
Physical Workload, J_P (rad^2s)	11.1	5.4	51%
Mental Workload, J_M (rad^2/s)	76.7	37.3	51%

The ESC control makes only a marginal increase in track following performance since the primary benefit is reduced swing out of the rear of the vehicle. As before the physical and mental workload metrics are reduced in half by the ESC sytem intervention. Note that at the low speeds through 3888-2, the TTS control is not triggered and therefore makes no change in performance metrics.

Another metric selected to evaluate ESC system performance is the maximum speed at which the vehicle was able to successfully navigate the course. The simulations were repeated with increasing vehicle speed in 0.1 kph increments until the vehicle failed to successfully navigate the course. These tests were conducted for both the nominal vehicle configuration and the oversteering vehicle with reduced cornering stiffness on the rear tires. Table 7.6 shows the results for both vehicles with ESC off, with ESC on with

the Equivalent Moment control only (EM) and with ESC on with both Equivalent Moment and Time To Saturation control (EM+TTS).

Table 7.6: Maximum Entry Speed for Severe Double Lane Change

Vehicle	Max speed, no ESC (kph)	Max speed w/ESC (kph)		% improvement w/ ESC	
		EM	EM+TTS	EM	EM+TTS
Nominal	62.2	64.8	64.8	4.2%	4.2%
Oversteering	55.4	59.4	59.8	7.2%	7.9%

Note that the improvement in course speed for the oversteering vehicle is significantly higher than that for the nominal vehicle. This is because the nominal vehicle is fairly well balanced and therefore performs reasonably well at the limits of traction. The ESC system does, however, enable the nominal vehicle to reach an initial speed 4% higher than without ESC control. The performance improvement of the oversteering vehicle is substantially higher because the ESC system is able to correct the rear axle saturation problems of the vehicle. The TTS algorithm provides substantial improvement by taking corrective action before the rear axle reaches saturation.

7.2.2 Low Friction Double Lane Change Simulation

The ISO 3888-1 double lane change course is intended to simulate a high speed overtaking maneuver. This maneuver was used to test the ESC performance on a low friction surface. Again vehicle speed was increased in 0.1 kph increments until the vehicle could no longer successfully navigate the course. In this test the driver attempts

to maintain the entry speed throughout the maneuver. Similar improvements in target speed were observed for the low friction double lane change as with the severe double lane change, as seen in Table 5.1. Again the ESC system with TTS enabled and TTS disabled produced the same performance metric values at these relatively low speeds.

Table 7.7: Performance Metrics for Nominal Vehicle Double Lane Change Low μ at 57.2 kph

Metric	ESC Off	ESC On	% Improvement
Task Performance, J_T (m^{2}s)	0.0259	0.0025	90%
Physical Workload, J_P (rad^{2}s)	2.34	0.96	59%
Mental Workload, J_M (rad^2/s)	11.0	4.0	64%

Again note that the task performance metric for the oversteering vehicle seen in Table 7.8 is an order of magnitude lower than that of the nominal vehicle. Therefore the improvement due to ESC is substantially lower. However, the driver physical and mental workloads are again reduced by 40-50%.

Table 7.8: Performance Metrics for Oversteering Vehicle Double Lane Change Low μ at 51.9 kph

Metric	ESC Off	ESC On	% Improvement
Task Performance, J_T (m^{2}s)	0.0023	0.0022	4%
Physical Workload, J_P (rad^{2}s)	1.17	0.70	40%
Mental Workload, J_M (rad^2/s)	5.7	2.6	54%

The maximum speed through the course for the double lane change on the low friction surface is shown in Table 7.9. For both vehicles the percentage improvement in

127

target speed is 4-5%. This is observed for the ESC system both with TTS is enabled and disabled.

Table 7.9: Maximum Target Speed for Double Lane Change on Low Friction Surface

Vehicle	Max speed, no ESC (kph)	Max speed w/ESC (kph)		% improvement w/ ESC	
		EM	EM+TTS	EM	EM+TTS
Nominal	57.2	60.0	59.6	4.9%	4.2%
Oversteering	51.9	54.5	54.5	5.0%	5.0%

Tests were also conducted of both vehicles on the high-speed ISO 3888-1 double lane change course with a high friction surface. However the vehicles were generally able to navigate the course without saturating lateral force. The ESC system on the oversteering vehicle did not intervene at all as desired. The ESC system on the nominal understeering detected slight axle saturation: first a brief saturation of the front axle and then a brief saturation of the rear axle. Therefore minimal differential braking was applied in this case. As a result in this case the rear axle had a slight reduction in lateral force due to the braking and swung out slightly. The top speed through the course was reduced from 96.8 to 96.5 kph – only a marginal change.

7.2.3 Fishhook Maneuver Simulation

Finally a standard fishhook maneuver was used to evaluate the propensity for spinout both with and without ESC. For this test the oversteering vehicle configuration was used as the understeering vehicle does not spin out at high speed. The test is

conducted at a constant target vehicle speed. The steering wheel is quickly ramped to 294 degrees and held briefly before being ramped back through 0 deg at 1 second. The steering wheel continues to be quickly ramped to -294 deg, at which is held for the remainder of the test. While this test is typically used for testing rollover propensity of trucks and SUVs, it may also induce spinout in a passenger car and is thus suitable for ESC testing as well.

The target speed of the vehicle was increased in 0.5 kph increments until vehicle spin out was observed. For this test vehicle spin out was defined as reaching a vehicle slip angle greater than or equal to 90 deg. On a high friction surface, the oversteer vehicle without ESC reached a maximum target speed of 72 kph without spinning out. However with the ESC system enabled, the same vehicle remained very stable with a maximum slip angle of <5 deg for this test. The vehicle sideslip angle for both tests can be seen in Table 7.9.
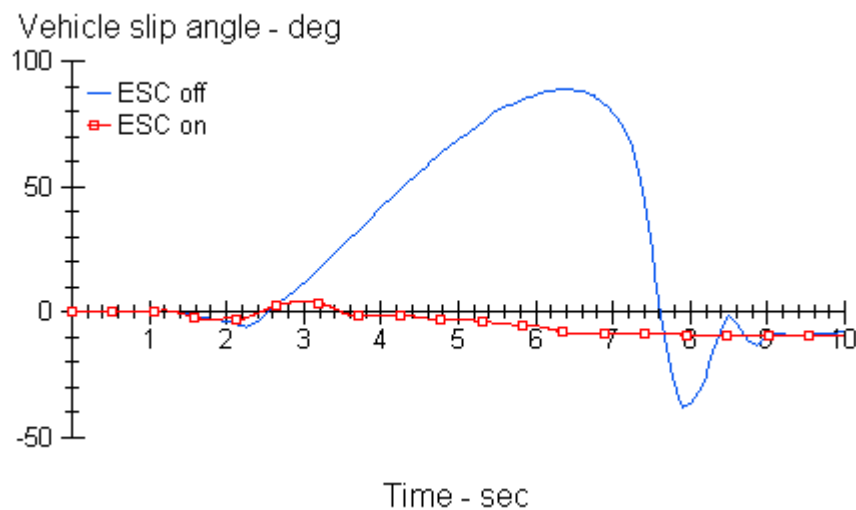
Figure 7.8: Fishhook Maneuver of Oversteering Vehicle at 72 kph

Tests were repeated with the ESC system enabled in an attempt to find the maximum target speed before spin out was induced. However, even at a target speed of 110 kph, the ESC system was able to bring the vehicle to a complete stop before the vehicle slip angle reached 90 degrees. By braking the front left wheel, the ESC system prevented vehicle oversteer throughout the maneuver.

7.3 ESC System Robustness Test Results

In order to test the robustness of the ESC system, the severe lane change maneuvers were again tested with a test vehicle configuration to simulate the test sedan fully loaded at Gross Vehicle Weight Rating (GVWR). The nominal sedan model was used with a 450 kg load placed in the trunk, 3.2 m behind the front axle of the vehicle. Note that the nominal sedan model is assumed to include a 75 kg driver, therefore the load simulates a maximum payload of 525 kg, which would be typical for this class of sedan.

The relevant vehicle parameters of the loaded vehicle are compared to the nominal vehicle in Table 5.1. The addition of the load in the trunk shifted the total vehicle center of gravity almost 0.5 m towards the rear of the vehicle. The change in load also significantly increased rear axle cornering stiffness while decreasing front axle cornering stiffness slightly. The yaw moment of inertia also increased substantially with the added load.

Table 7.10: Loaded Test Vehicle Parameters

Parameter	Units	Nominal	Loaded	Net Change
Mass, m	kg	1530	1980	+450
Yaw moment of inertia, J	kg*m^2	4607	6122	+1515
CG long. distance to front axle, a	m	1.139	1.607	+0.468
CG long. distance to rear axle, b	m	1.637	1.169	-0.468
Nominal front axle cornering stiffness, C_1	N/rad	238,300	226,300	-12,000
Nominal rear axle cornering stiffness, C_2	N/rad	173,500	301,000	+127,500
CG height from ground, h_G	m	0.519	0.560	+0.041

To test the loaded vehicle, the ISO 3888-1 severe double lane change maneuver described in 7.2.1 Severe Double Lane Change Simulation was used. The maximum speed that the loaded test vehicle was able to successfully complete the maneuver was reduced from 62.2 kph to 56.0 kph as shown in Table 7.11. The table also shows the maximum speed of the loaded test vehicle with two ESC configurations: one in which the ESC system assumes the parameters of the nominal unloaded vehicle and one that uses the actual parameters of the loaded vehicle. The first simulates an ESC system without adaptation, while the second simulates the ESC system utilizing the identified loaded vehicle parameters in the estimation of axle slip angles, lateral forces and saturation. Note that in order to identify these changes, the system would need to detect the changes in mass and center of gravity longitudinal location using sensors such as load sensors in the suspension of each axle. The changes in axle cornering stiffnesses and total vehicle yaw moment of inertia may then be identified automatically using the recursive least squares algorithm presented in section 5.3 Vehicle Yaw Moment of Inertia Identification.

.

Table 7.11: Maximum Entry Speed for Loaded Vehicle Severe Double Lane Change

Vehicle	Max speed, no ESC (kph)	Max speed w/ESC, nominal vehicle params (kph)	Max speed w/ESC, loaded vehicle params (kph)
Nominal	62.2	64.8	
Loaded	56.0	58.2	60.5

The results of table show that even when the ESC system did not adapt to the changed vehicle parameters, it was still able to improve vehicle performance through the maneuver. In this case the system still applied appropriate differential braking to help maintain control of the vehicle through the maneuver. However, due to the errors in assumed vehicle parameters, the system tended to overestimate rear axle saturation and applied excessive differential braking to the front axle. This in turn reduced the front axle lateral force and thus the cornering ability of the vehicle as it tried to navigate the course. However, when the ESC system assumed the changed parameters of the loaded vehicle, the maximum speed through the course was improved by 8% to 60.5 kph.

The results show that the ESC strategy is robust with respect to significant change in vehicle parameters due to loading at GVWR. However the results also show that the performance of the ESC system may be improved significantly by adapting the vehicle parameters used by the algorithm to the changes automatically identified using the strategies described in this research.

Chapter Summary

This chapter showed the results of simulations used to evaluate the performance of the parameter identification and ESC strategies presented. Co-simulations of the ESC strategy implemented in LabVIEW and a high-fidelity model of a sedan in CarSim were used in the evaluations. Standard ISO double lane change simulations with a simple driver steering model in CarSim demonstrated the improvement in performance with the ESC system. Notably, the driver physical and mental effort was shown to be reduced in half at the limits of vehicle handling with the ESC system enabled. An oversteering vehicle with reduced rear tire cornering stiffness exhibited significant improvement in performance with the predictive Time to Saturation algorithm enabled. Simulations on both high friction and low friction road surfaces demonstrated the ability of the system to identify and adapt to changing environmental conditions. A fishhook steering maneuver was used to demonstrate the ability of the ESC system to prevent spinout of an oversteering vehicle.

Finally, robustness of the ESC system was tested by changing adding 450 kg at the rear of the vehicle to simulate an extreme loading condition. The designed ESC system based on the nominal vehicle parameters was shown to be robust and still yielded performance improvements when implemented on the loaded vehicle. Further improvement in system performance was demonstrated when the ESC strategy was adapted to use the changed vehicle parameters detected by the parameter identification strategy.

CHAPTER EIGHT

CONCLUSION

8.1 Summary of Findings

This dissertation presented a novel scheme for estimating relevant vehicle states and parameters, as well as a novel ESC strategy. The proposed system utilizes the same sensors and actuators employed in current production passenger car ESC systems. A novel nonlinear reduced-order lateral velocity observer was employed to aid in the estimation of axle slip angles. The designed lateral velocity observer has a dynamic feedback gain that is adapted based on current vehicle state. As a result the lateral velocity observer uses the kinematic model-based estimate to accurately track lateral velocity during transient nonlinear maneuvers, yet corrects estimates for sensor bias and noise errors during normal stable driving conditions. The estimated lateral velocity was used in turn with other vehicle states to estimate slip angle at each axle. The axle slip angle estimation also included a first-order lag model to account for tire relaxation length effects and aid in the subsequent time correlation of slip angles with estimated axle lateral forces.

The lateral force at each axle was estimated by inverting the lateral force and yaw moment equations. These relationships allowed the lateral force to be directly calculated from the measured lateral acceleration and the measured or calculated yaw angular acceleration. Since lateral force generation may be reduced due to tire longitudinal forces from braking or drive traction, the lateral force potential of each axle was calculated in order to estimate the lateral force that would be generated in the absence of longitudinal

forces. The slip angles together with estimated lateral forces enable the real-time detection of axle lateral force saturation. When axle lateral force saturation is detected, the road coefficient of friction is estimated using the axle lateral and normal forces.

When the axle lateral forces are not saturated, the estimated states are used in a recursive least squares algorithm to identify axle cornering stiffness coefficients and total vehicle yaw moment of inertia. The parameter identification approach was shown to accurately identify changes in these parameters during normal driving conditions. In addition, the identification of axle cornering stiffness coefficients was shown to enable the control strategy to adapt to changes in total vehicle mass. An attempt to identify center of gravity longitudinal location using a similar technique proved to be unsuccessful. Future work could possibly investigate this issue further and employ other techniques to successfully identify center of gravity location.

During axle lateral force saturation, the Equivalent Moment ESC controller applies differential braking to generate a moment equivalent to the difference in moment that would be generated by the saturated axle if it had perfectly linear cornering stiffness capability. A key advantage to this approach over other ESC strategies is that the case of lateral force saturation of both axles can be detected and handled explicitly by the control strategy. In addition to the Equivalent Moment strategy, the predictive Time to Saturation algorithm was used to anticipate rear axle lateral force saturation and take corrective action in advance. Finally the ABS braking strategy was presented in which the longitudinal slip ratio target ranges were adapted to compensate for current estimates of coefficient of friction and axle slip angle.

The ESC system was shown by simulation to significantly improve vehicle stability and controllability while reducing driver physical and mental workload. The maximum speed at which a virtual driver could navigate various double lane change maneuvers was shown to be increased significantly using the described ESC strategy. The Time to Saturation algorithm was shown to improve performance significantly of the oversteering vehicle configuration with reduced rear tire cornering stiffness. The robustness of the ESC system was also demonstrated by simulating a heavily loaded vehicle configuration with the nominal vehicle parameters. The benefit of the adaptive control strategy was also demonstrated by the improved performance of the ESC control system with the oversteering vehicle when the changes in vehicle parameters detected by the parameter identification strategy were incorporated into the ESC controller.

One key feature of the equivalent moment ESC algorithm is that it does not require tuning of controller gains for successful implementation. Conventional ESC systems employ a state feedback controller for which feedback gains must be tuned to produce the desired response. In addition, these systems rely on the bicycle model with accurate vehicle parameters to generate desired vehicle states. While the equivalent moment algorithm does utilize some vehicle parameters for estimation, key parameters such as axle cornering stiffness and vehicle yaw moment of inertia are estimated and thus the controller automatically adapts to changes. The identification of cornering stiffness was also shown to enable adaptation of the ESC control system to changes in vehicle mass. Changes in vehicle mass or tire cornering stiffnesses are reflected in the estimated

cornering stiffness values, in turn allowing the accurate detection of axle lateral force saturation and adaptation of the ESC strategy.

8.2 Future Work

It should be noted that the current system is designed to function properly even when the driver is applying brakes or drive traction commanded from the throttle pedal, even though these scenarios were not investigated in the simulation results of this dissertation. However, the current system only considers the use of braking force beyond the current brake pressure applied by the driver to apply a corrective moment to the vehicle. Future work could be done to investigate the possibility of releasing brake pressure on individual wheels to affect a yaw moment when the driver is applying brake force from the master cylinder. The use of other actuation devices such as active drivetrain torque distribution could utilize the same strategies presented here.

In addition, the estimation and control strategies could be further improved by incorporating longitudinal dynamics into the calculations. The addition of a longitudinal accelerometer would enable estimation of lateral force distribution between the front and rear wheels. In addition the kinematic interactions of the lateral and longitudinal dynamics could be incorporated to improve accuracy during transient maneuvers.

The models could be extended to incorporate roll dynamics of the sprung mass and possibly the axles. Currently the lateral load transfer of the wheel normal forces assumes a static model with no roll. While this was found to produce acceptable estimates for use in the ESC system, the estimates could be greatly improved during transient maneuvers when the vehicle experiences significant roll motion. In addition,

the inclusion of roll could enable the active roll control in addition to yaw stability control. A nonlinear observer scheme similar to the one used for lateral velocity could be used to estimate roll angle from integrated roll angle sensor data, with correction from a nonlinear observer feedback term when lateral acceleration is small. With the roll estimate, a predictive scheme similar to the Time To Saturation scheme of the ESC system could be used to estimate time to vehicle rollover for trucks or SUVs with higher center of gravity. Vehicle braking could be used to slow the vehicle before unrecoverable rollover conditions are realized.

While a sedan was used for simulation testing in this research, the methods would be directly applicable to straight trucks. The trucks could especially benefit from the parameter identification and controller adaptation since they have varying loading conditions between trips.

In addition, the stability concepts presented here could be extended to articulated tractor/semi-trailer combination vehicles. Stability control systems are commercially available today for both tractors and trailers and may include sensors for lateral acceleration and yaw rate on both units. If trailer sensor data were to be communicated to the tractor stability control system, many of the method presented here could be extended to the articulated combination vehicle. For example, a similar nonlinear reduced order observer could be used to estimate trailer articulation angle by integrating the difference between the tractor and trailer yaw rate sensors. The observer could use a nonlinear feedback term to correct integration errors using a second kinematic relationship or an articulated bicycle dynamic model. Forces could be estimated by using

the same inverse dynamic relationship. Assuming that a single lateral force could be used for all tractor drive axles and a single lateral force for all trailer axles, the unknown lateral forces would be these two, the steer axle lateral force and the lateral force transmitted at the hitch kingpin. The lateral force and angular momentum balance equations could then be solved for the four unknown lateral forces. The ESC controller could be extended to the complete combination vehicle. The two-axle vehicle considered three possible axle saturation conditions: front axle only, rear axle only or both axles. Treating the combination tractor/semi-trailer as a three axle vehicle, there would be seven possible axle saturation combinations, and appropriate control strategies would need to be developed for each.

REFERENCES

1.   Update on Electronic Stability Control. IIHS Status Report, 2006. **41**(5).

2.   FMVSS No. 126 Electronic Stability Control Systems. 2006, National Highway Traffic Safety Administration.

3.   Wang, J. and F.M. Council, *Estimating Truck-Rollover Crashes on Ramps by Using a Multistate Database.* Transportation Research Record, 1999. **1686**: p. 29-35.

4.   Sampson, D.J.M. and D. Cebon, *An investigation of roll control system design for articulated heavy vehicles*, in *Proc. 4th International Symposium on Advanced Vehicle Control*. p. 311–316.

5.   *Bendix Stability FAQs*. 2008 [cited; Available from: http://www.bendix.com/SiteCollectionDocuments/ABS/StabilityFAQ.pdf.

6.   Ghoneim, Y.A., W.C. Lin, D.M. Sidlosky, H.H. Chen, Y.-K. Chin, and M.J. Tedrake, *Integrated chassis control system to enhance vehicle stability.* Int. J. of Vehicle Design, 2000. **23**(1/2).

7.   Tseng, H.E., B. Ashrafi, D. Madau, T.A. Brown, and D. Recker, *The Development of Vehicle Stability Control at Ford.* IEEE/ASME Transactions on Mechatronics, 1999. **4**(3).

8.   Manning, W.J. and D.A. Crolla, *A review of yaw rate and sideslip controllers for passenger vehicles.* Transactions of the Institute of Measurement and Control, 2007. **29**(2): p. 117–135.

9.   Shibahata, Y., K. Shimada, and T. Tomari, *Improvement of Vehicle Maneuverability by Direct Yaw Moment Control.* Vehicle System Dynamics, 1993. **22**: p. 465-481.

10.   van Zanten, A.T., *Bosch ESP Systems: 5 Years of Experience.* SAE Paper 2000-01-1633, 2000.

11.   van Zanten, A.T., R. Erhardt, K. Landesfeind, and G. Pfaff, *VDC Systems Development and Perspective.* SAE Paper 980235, 1998.

12.   van Zanten, A.T., R. Erhardt, and G. Pfaff, *VDC, The Vehicle Dynamics Control System of Bosch.* SAE Paper 950759, 1995.

13. Bedner, E., D. Fulk, and A. Hac, *Exploring the Trade-Off of Handling Stability and Responsiveness With Advanced Control Systems.* SAE Paper 2007-01-0812, 2007.

14. Genta, G., *Motor Vehicle Dynamics : Modeling and Simulation*. Series on Advances in Mathematics for Applied Sciences. Vol. 43. 1997, Singapore; River Edge, N.J.: World Scientific. 539.

15. Esmailzadeh, E., A. Goodarzi, and G.R. Vossoughi, *Optimal yaw moment control law for improved vehicle handling.* Mechatronics, 2003. **13**(7): p. 659-675.

16. Zheng, S., H. Tang, Z. Han, and Y. Zhang, *Controller design for vehicle stability enhancement.* Control Engineering Practice, 2006. **14**(12): p. 1413-1421.

17. Anwar, S., *Generalized predictive control of yaw dynamics of a hybrid brake-by-wire equipped vehicle.* Mechatronics, 2005. **15**(9): p. 1089-1108.

18. Eslamian, M., G. Alizadeh, and M. Mirzaei, *Optimization-based non-linear yaw moment control law for stabilizing vehicle lateral dynamics.* Proceedings of the Institution of Mechanical Engineers, Part D: Journal of Automobile Engineering, 2007. **221**.

19. Yi, K., T. Chung, J. Kim, and S. Yi, *An investigation into differential braking strategies for vehicle stability control.* Proceedings of the Institution of Mechanical Engineers, Part D: Journal of Automobile Engineering, 203. **217**.

20. Abe, M., Y. Kano, K. Suzuki, Y. Shibahata, and Y. Furukawa, *Side-slip control to stabilize vehicle lateral motion by direct yaw moment.* JSAE Review, 2001. **22**(4): p. 413-419.

21. Rajamani, R., *Vehicle Dynamics and Control*. 2006, New York: Springer Science. 470.

22. Wielenga, T.J., *A Method for Reducing On-Road Rollovers ± Anti-Rollover Braking.* SAE Paper 1999-01-0123, 1999.

23. Deng, W. and H. Zhang. *RLS-based online estimation on vehicle linear sideslip.* in *American Control Conference, 2006*. 2006.

24. Bevly, D.M., J.C. Gerdes, C. Wilson, and Z. Gengsheng. *The use of GPS based velocity measurements for improved vehicle state estimation*. in *American Control Conference, 2000. Proceedings of the 2000*. 2000.

25.   Ryu, J., E.J. Rossetter, and J.C. Gerdes. *Vehicle Sideslip and Roll Parameter Estimation using GPS*. in *AVEC 2002 6th Int. Symposium on Advanced Vehicle Control*. 2002. Hiroshima, Japan.

26.   Bevly, D.M., J. Ryu, and J.C. Gerdes, *Integrating INS Sensors With GPS Measurements for Continuous Estimation of Vehicle Sideslip, Roll, and Tire Cornering Stiffness.* Intelligent Transportation Systems, IEEE Transactions on, 2006. **7**(4): p. 483-493.

27.   Farrelly, J. and P. Wellstead. *Estimation of vehicle lateral velocity*. in *Control Applications, 1996., Proceedings of the 1996 IEEE International Conference on*. 1996.

28.   Anderson, R. and D.M. Bevly. *Estimation of slip angles using a model based estimator and GPS*. in *American Control Conference, 2004. Proceedings of the 2004*. 2004.

29.   Hac, A. and M.D. Simpson, *Estimation of Vehicle Side Slip Angle and Yaw Rate.* SAE Paper 2000-01-0696, 2000.

30.   Liu, C.S. and H. Peng, *A State and Parameter Identification Scheme for Linearly Parameterized Systems.* ASME Journal of Dynamic Systems, Measurement and Control, 1998. **120**(4): p. 524-528.

31.   Ungoren, A.Y., H. Peng, and H.E. Tseng, *A study on lateral speed estimation methods.* Int. J. of Vehicle Autonomous Systems 2004. **2**(1/2): p. 126 - 144.

32.   von Vietinghoff, A., S. Olbrich, and U. Kiencke, *Extended Kalman Filter for Vehicle Dynamics Determination Based on a Nonlinear Model Combining Longitudinal and Lateral Dynamics.* SAE Paper 2007-01-0834, 2007.

33.   Imsland, L., H.F. Grip, T.A. Johansen, T.I. Fossen, J.C. Kalkkuhl, and A. Suissa, *Nonlinear Observer for Vehicle Velocity with Friction and Road Bank Angle Adaptation-Validation and Comparison with an Extended Kalman Filter.* SAE Paper 2007-01-0808 2007.

34.   Fukada, Y., *Slip-Angle Estimation for Vehicle Stability Control.* Vehicle System Dynamics: International Journal of Vehicle Mechanics and Mobility, 1999. **32**(4): p. 375 - 388.

35.   Nishio, A., K. Tozu, H. Yamaguchi, K. Asano, and Y. Amano, *Development of vehicle stability control system based on vehicle sideslip angle estimation.* SAE Paper 2001-01-0137, 2001.

36. Ashrafi, B. and D.A. Recker, *U.S. Patent 5,742,919 Method and Apparatus for Dynamically Determining a Lateral Velocity of a Motor Vehicle*. 1998, Ford Global Technologies, Inc.

37. Lu, J. and T.A. Brown, *U.S. Patent 6,671,595 Vehicle side slip angle estimation using dynamic blending and considering vehicle attitude information*. 2003: Ford Global Technologies, LLC.

38. Au, F.T.K., R.J. Jiang, and Y.K. Cheung, *Parameter identification of vehicles moving on continuous bridges.* Journal of Sound and Vibration, 2004. **269**(1-2): p. 91-111.

39. Yi, K. and K. Hedrick, *Observer-Based Identification of Nonlinear System Parameters.* Journal of Dynamic Systems, Measurement, and Control, 1995. **117**: p. 175.

40. Bae, H.S., J. Ryu, and J.C. Gerdes. *Road Grade and Vehicle Parameter Estimation for Longitudinal Control Using GPS*. in *IEEE Conference on Intelligent Transportation Systems, Proceedings, ITSC*. 2001. Oakland, CA.

41. Lingman, P. and B. Schmidtbauer, *Road slope and vehicle mass estimation using Kalman filtering.* Vehicle System Dynamics, 2003. **37**: p. 12-23.

42. Vahidi, A., M. Druzhinina, and A. Stefanopoulou. *Simultaneous mass and time-varying grade estimation for heavy-duty vehicles*. in *American Control Conference, 2003. Proceedings of the 2003*. 2003.

43. Huh, K., J. Jung, D. Hong, S. Lim, S. Han, K. Han, H.Y. Jo, and J.M. Yun, *Vehicle Mass Estimator Design for Adaptive Roll Stability Control.* SAE Paper 2007-01-0820, 2007.

44. Ryu, J., *State and Parameter Estimation for Vehicle Dynamics Control Using GPS*, in *Department of Mechanical Engineering*. 2004, Stanford University.

45. Solmaz, S., M. Akar, and R. Shorten. *Online Center of Gravity Estimation in Automotive Vehicles using Multiple Models and Switching*. in *Control, Automation, Robotics and Vision, 2006. ICARCV '06. 9th International Conference on*. 2006.

46. Ray, L.R., *Nonlinear state and tire force estimation for advanced vehicle control.* Control Systems Technology, IEEE Transactions on, 1995. **3**(1): p. 117-124.

47. Ray, L.R., *Nonlinear Tire Force Estimation and Road Friction Identification: Simulation and Experiments.* Automatica, 1997. **33**(10): p. 1819-1833.

48. Dutton, K., S. Thompson, and B. Barraclough, *The Art of Control Engineering*. 1997: Prentice Hall.

49. Bernard, J.E. and C.L. Clover, *Tire Modeling for Low–speed and High–speed Calculations*. SAE Paper 950311, 1995.

50. Åström, K.J. and B. Wittenmark, *Adaptive Control: Second Edition*. 1994: Prentice Hall.

51. Pacejka, H.B. and R.S. Sharp, *Shear Force Development by Pneumatic Tyres in Steady State Conditions: A Review of Modelling Aspects*. Vehicle System Dynamics: International Journal of Vehicle Mechanics and Mobility, 1991. **20**(3): p. 121 - 175.

52. Mimuro, T., R.G. Dubensky, H. Yasunaga, K. Satoh, and M. Ohsaki, *Four parameter evaluation method of lateral transient response*. SAE Paper 901734, 1990.

53. Vedamuthu, S. and E.H. Law, *An investigation of the pulse steer method for determining automobile handling qualities*. SAE Paper 930829, 1993.

54. *ISO 3888-2:2002 Passenger cars -- Test track for a severe lane-change manoeuvre -- Part 2: Obstacle avoidance*. 2002, International Organization for Standardization (ISO).

55. Horiuchi, S. and N. Yuhara, *An Analytical Approach to the Prediction of Handling Qualities of Vehicles With Advanced Steering Control System Using Multi-Input Driver Model*. Journal of Dynamic Systems, Measurement, and Control, 2000. **122**(3): p. 490-497.

56. Oscarsson, M., *Variable Vehicle Dynamics Design - Objective Design Methods*, in *Department of Electrical Engineering*. 2003, Linköping University.